Graduate School Form
30 Updated 12/26/2015

PURDUE UNIVERSITY
GRADUATE SCHOOL
Thesis/Dissertation Acceptance

This is to certify that the thesis/dissertation prepared

By Kyong-Yup Paik

Entitled
Experimental Investigation of Hot-Jet Ignition of Methane-Hydrogen Mixtures in A Constant-Volume Combustor

For the degree of Master of Science in Mechanical Engineering

Is approved by the final examining committee:

M. Razi Nalim
Chair

Likun Zhu
Co-chair

Whitney Yu
Co-chair

To the best of my knowledge and as understood by the student in the Thesis/Dissertation Agreement, Publication Delay, and Certification Disclaimer (Graduate School Form 32), this thesis/dissertation adheres to the provisions of Purdue University's "Policy of Integrity in Research" and the use of copyright material.

Approved by Major Professor(s): M. Razi Nalim

Approved by: Sohel Anwar 10/5/2016
Head of the Departmental Graduate Program Date

EXPERIMENTAL INVESTIGATION OF HOT-JET IGNITION OF METHANE-HYDROGEN MIXTURES IN A CONSTANT-VOLUME COMBUSTOR

A Thesis

Submitted to the Faculty

of

Purdue University

by

Kyong-Yup Paik

In Partial Fulfillment of the

Requirements for the Degree

of

Master of Science in Mechanical Engineering

December 2016

Purdue University

Indianapolis, Indiana

To my mom and dad, my brother, and my wife.

ACKNOWLEDGMENTS

I would first like to express my special appreciation and thanks to my advisor Professor Dr. M. Razi Nalim who has guided and supported me throughout my graduate studies. He consistently allowed this paper to be my own work, but steered me in the right the direction whenever he thought I needed it.

I would also like to thank my committee members Dr. Whitney Yu and Dr. Likun Zhu for their time, good advice and proposing improvements on my thesis. Appreciation and thanks is also given to Ms. Valerie Lim Diemer, Ms. Aimee Brough, Ms. Sherrie Tucker, Mr. Michael Golub, and Mr. Jerry Mooney for their help to prepare this thesis.

Special thanks to my colleagues at the Combustion and Propulsion Research Laboratory, Md Nazmuzzaman Khan, Arash Jamali, Ali Tarraf Kojok, and Mohammad Ebrahim Feyz, for sharing their knowledge and research experience which helped me to come up with ideas for experimental tests, and for all the fun we have had in the last three years.

Finally, I must express my very profound gratitude to my mom Yang Sook, my dad Kwang Eup, my brother Seung Yeop, and my wife Hyo Jeong, for providing me with unfailing support and continuous encouragement throughout my years of study and through the process of researching and writing this thesis. This accomplishment would not have been possible without them.

TABLE OF CONTENTS

Page

LIST OF TABLES vii

LIST OF FIGURES viii

ABBREVIATIONS xiii

NOMENCLATURE xv

ABSTRACT xviii

1 INTRODUCTION 1

1.1 History of Wave Rotor Developments 1

1.2 Operating Principle of Wave Rotor Combustors 2

1.3 Previous Research 7

1.3.1 Hot-Jet Ignition 7

1.3.2 Ignition Delay Time 8

1.3.3 Lean Premixed Methane-Hydrogen-Air Flames 11

1.3.4 Schlieren Photography Technique 16

1.4 Scope of the Present Research 25

2 EXPERIMENTAL SETUP AND PROCEDURE 26

2.1 Pre-Chamber 28

2.1.1 Spark Plug 30

2.1.2 Nozzle 30

2.1.3 Diaphragm 32

2.2 Pre-Chamber Ignition System 36

2.3 Main Chamber 38

2.4 Ignition Process 40

2.5 Fueling System 42

2.5.1 Pre-Chamber Fueling 44

Page

2.5.2 Main Chamber Fueling 47
2.6 Data Acquisition 56
2.6.1 Synchronizing Circuit 56
2.6.2 Pressure Data Acquisition System 59
2.6.3 Dynamic Pressure Transducer 59
2.6.4 Pressure Sensor Probe 62
2.6.5 High-Speed Image Acquisition System 65
2.7 Schlieren Photography Setup 67
2.8 Schlieren Image Processing 70
2.9 Experimental Procedure 73
2.10 Experimental Conditions 74
3 IGNITION DELAY TIME INVESTIGATION 75
3.1 Repeatability Test of Pre-chamber Combustion 75
3.2 Initial Shock Speed Measurement 79
3.3 Diaphragm Rupture Timing and Pressure 87
3.4 Reflected Shock Pressure Measurement 92
3.4.1 Simple Shock Tube Model 92
3.4.2 Pressure Ratio Across Initial Shock Wave 95
3.4.3 Pressure Ratio of P_5 to P_1 97
3.4.4 Attenuation of Pressure Ratio of Reflected Shock Wave . . . 100
3.5 Ignition Delay Time Measurement 106
3.5.1 Effect of Diaphragm Rupture Pressure on Ignition Delay Time 113
3.5.2 Effect of Hydrogen Content in Fuel Mixture on Ignition Delay Time 119
3.5.3 Effect of Equivalence Ratio on Ignition Delay Time 120
4 COMBUSTION CHARACTERISTICS AND SHOCK-WAVE INTERACTION 123
4.1 Maximum Pressure in Main Chamber after Ignition 123
4.2 Flame Motion and Interaction due to Pressure Waves 129

Page

4.2.1 Flame Front Motion by Pressure Waves 129
4.2.2 Shock-Flame Interaction 129
4.2.3 Observations of Flame Behavior and Shock-Wave Interactions 134
4.2.4 Flame Front Oscillation by Shock-Flame Interactions 140
4.2.5 Comparison of Gas Motion and Pressure Oscillation Frequencies 142
4.3 Combustion Time Measurement 144
5 CONCLUSION AND RECOMMENDATIONS 146
5.1 Conclusions 146
5.2 Recommendations 148
LIST OF REFERENCES 151
APPENDICES
A MATLAB Code to Measure the Flame Front Position by Time 158
B Flame Front Position Versus Pressure History from Schlieren Test Cases 161

LIST OF TABLES

Table Page

2.1 Fuel specifications 43

2.2 The local atmospheric pressures of the test days [48] 55

2.3 Specifications of PCB pressure transducers 61

2.4 High-speed camera setting conditions 66

2.5 Experimental conditions 74

3.1 Validation results of the initial shock speed estimation 86

3.2 Validation of the diaphragm rupture moment estimation 91

4.1 Classification of combustion characteristics for all test conditions 137

LIST OF FIGURES

Figure Page

1.1 Comparison of Humphrey cycle (1-2-3-4) with Brayton cycle (1-2-3b-4b) [17] 3

1.2 Schematic configuration of a wave rotor combustion from inlet (top) and exit (bottom) views [15] 5

1.3 Schematic developed view of a wave-rotor combustor [17] 6

1.4 An example of end wall pressure trace from a shock tube experiment [28] 10

1.5 Effects of equivalence ratio on ignition for methane dominating ignition, 80% CH_4/20% H_2 [35] 13

1.6 Effects of equivalence ratio on ignition for hydrogen and methane dominating ignition, 40% CH_4/60% H_2 [35] 15

1.7 Light ray deflection by density gradients 17

1.8 The variation of the speeds of two light rays by the density difference . 17

1.9 Angle change between point 1 and 2 by the light ray deflection 20

1.10 Snell′s law 20

1.11 Contrast caused by light deflection 22

1.12 Example of the shadowgraph 22

1.13 Schlieren setup 23

1.14 Z-type Schlieren setup 23

1.15 Comparison of Schlieren and shadowgraph images (a) Schlieren image of turbulent helium jet (b) shadowgraph image of the same jet [43] 24

2.1 Combustion chambers in the wave-rotor constant volume ignition and combustion rig 27

2.2 Front plate of the pre-chamber with nozzle insert on the right, and pressure transducer insert on the left 29

2.3 Selected nozzle insert dimensions [17] 31

Figure Page

2.4 Nozzle insert, scored diaphragm, nozzle plate, and nozzle insert assembly (from left) 34

2.5 Diaphragm rupture patterns [17] 34

2.6 Diaphragm rupture process, Φ=1.1, and Ψ=1 (CH_4:H_2=50:50) (a) rupture with a cross form (b) delayed rupture 34

2.7 Path lines of the visible particles from the nozzle on the pre-chamber, Φ=1.1, and Ψ=1 (CH_4:H_2=50:50) (a) with a diaphragm (b) without a diaphragm 35

2.8 Schematic diagram of the pre-chamber ignition system 37

2.9 Locations of pressure transducers and a fueling port on the main chamber 39

2.10 Pre-chamber ignition process 41

2.11 Main chamber ignition process 41

2.12 Schematic diagram of the pre-chamber fueling system 45

2.13 Schematic diagram of the main chamber fueling system 49

2.14 Main chamber fueling procedure 49

2.15 Schematic diagram of gas components in the fueling process 52

2.16 Schematic diagram of data acquisition system 57

2.17 Synchronizing circuit diagram 58

2.18 Schematic diagram of the quasi-infinite line pressure probe [56] 64

2.19 Quasi-infinite line pressure probe with design parameters 64

2.20 Measurement ranges of the high-speed camera 66

2.21 Schematic diagram of the Schlieren setup and the view of the knife edge covering the light beam cross-section 68

2.22 Image processing procedure for extracting a flame front line from the original Schlieren image 72

3.1 Pre-chamber pressure records with three different equivalence ratios . . 77

3.2 Calculated adiabatic flame temperature of hydrogen and methane mixture with respect to equivalence ratio at 1 bar and 300 K [63] 78

3.3 Measurement of the propagation speed of the Initial shock wave using pressure records of PT1 and PT2 (Main chamber condition: Φ=0.8, H_2=50%, indentation #=2, case #=2) 81

Figure Page

3.4 Time-resolved, post-processed Schlieren images of the initial shock wave propagation, and a graph of the shock wave x-position with respect to time (Main chamber condition: Φ=1.0, H_2=70%) 83

3.5 Validation of the initial shock speed estimation 84

3.6 Top-view of the setup for the validation test of the diaphragm rupture moment (left), and an image of the diaphragm rupture moment taken by the high-speed camera (right) 88

3.7 Validation of the diaphragm rupture moment estimation 88

3.8 Diaphragm rupture pressure is controlled by the number of indentation on a diaphragm 90

3.9 Sequence of shock wave propagations in the shock tube experiment, and wave diagram [65] 94

3.10 Properties of two zones across the initial shock wave 96

3.11 Properties of two zones across the reflected shock wave 98

3.12 Definition of the amplitude of the reflected shock wave obtained from PT2 pressure record, Original PT2 record (Left) and a zoomed version in the blue square (Right) 102

3.13 Comparing the measured pressure ratio (black dots) and the calculated pressure ratio (red line) 103

3.14 x-t Diagram for the expansion fan and the initial shock wave behaviors after the diaphragm rupture, and a comparison between two driver length C_1, and C_2 [70] 105

3.15 Definition of the ignition delay time 109

3.16 Definition of the ignition moment obtained from PT1 pressure record. Original PT1 pressure record (Left) and a zoomed version in the red square (Right). The blue vertical line indicates the ignition moment in the left figure (Main chamber condition: Φ=0.8, H_2=50%, indentation #=2, case #=2) 110

3.17 Time-resolved flame luminosity images obtained by the high-speed camera for the validation of the ignition moment (Main chamber condition: Φ=0.8, H_2=50%, indentation #=2, case #=2) 111

3.18 Comparing the ignition moments obtained by PT1 pressure records and the high-speed camera 112

Figure Page

3.19 Ignition delay time variation with respect to the rupture pressure change (Black: Φ=1.0, Red: Φ=0.8, Blue: Φ=0.6, Yellow: Φ=0.4, Solid line: H_2=50%, Dotted line: H_2=70%) 115

3.20 Time-resolved temperature distribution in CVC chamber for hydrogen-methane-air mixture Φ=1.0, and H_2=70% with respect to the pre-chamber rupture pressure variation (a)2 bar, (b)4 bar and (c)6 bar [45] 116

3.21 Mach number variation of the initial shock wave with respect to the rupture pressure change for all test cases 118

3.22 Re-arranged version of the ignition delay time variation with respect to the rupture pressure change (Black : Φ=1.0, Red: Φ=0.8, Blue: Φ=0.6, Yellow: Φ=0.4, Solid line: H_2=50%, Dotted line: H_2=70%) 122

3.23 Effects of equivalence ratio on ignition delay of hydrogen and methane dominating mixture for hydrogen content 60% (a) [35], and 50% (b) [74] 122

4.1 Maximum pressure of hydrogen-methane-air mixture combustion pressure in the main chamber for all test cases 126

4.2 Adiabatic constant-volume combustion pressure and temperature for the experiment conditions obtained using the CEA NASA code 127

4.3 Laminar burning velocities for a hydrogen-methane-air mixture as a function of equivalence ratio and hydrogen content. Symbols, experiments; lines, modeling [81] 128

4.4 Illustration of slow-fast and fast-slow interactions 130

4.5 Evolution of RMI at a single-mode interface perturbation [89] 133

4.6 Time-resolved Schlieren images of (a) Φ=1.0 and H_2=50%, and (b) Φ=0.6 and H_2=70%. The numbers beside each image indicate the time after trigger 135

4.7 Pressure records in the main chamber obtained by PT2 for the test conditions of (a) Φ=1.0 and H_2=50%, and (b) Φ=0.6 and H_2=70% 137

4.8 Feedback mechanism enhancing the flame acceleration 139

4.9 Comparison of flame front movement and pressure oscillation. (a) Φ=1.0 and H_2=50% and (b) Φ=0.6 and H_2=70% are the zoomed-out version, and (c) Φ=1.0 and H_2=50% and (d) Φ=0.6 and H_2=70% are the zoomed-in version 141

4.10 Comparison of gas oscillation frequencies of the pressure before and after ignition, and the flame front. Left : H_2=50%, Right : H_2=70% 143

Figure Page

4.11 Combustion time variation with respect to the equivalence ratio and the hydrogen content 145

B.1 Φ=1.0, Time scale=5 ms, Pressure range=10∼90 psig, Flame front movement range=26∼40 cm 161

B.2 The original flame front (white line) is pushed out by the new flame bubble (black line) generated in front of the original flame 162

B.3 Φ=0.8, Time scale=4 ms, Pressure range=10∼100 psig, Flame front movement range=26∼40 cm 163

B.4 Φ=0.6, Time scale=4 ms, Pressure range=10∼80 psig, Flame front movement range=26∼40 cm 164

B.5 Φ=0.4, Time scale=10 ms, Pressure range=10∼50 psig, Flame front movement range=26∼40 cm 165

ABBREVIATIONS

NOx	Nitrogen oxide
CCD	Charge coupled device
CPRL	Combustion and propulsion research laboratory
PET	Polyethylene terephthalate
CDI	Capacitive discharge ignition
AC	Alternating current
DC	Direct current
rpm	Revolutions per minute
psi	Pounds per square inch
psig	Pounds per square inch gauge
ppm	Parts per million
FL	Flame luminosity image
Sch	Schlieren image
JFET	Junction field effect transistor
DAQ	Data acquisition
VI	Virtual instrument
DTC	Discharge time constant
PT	Pressure transducer
fps	Frames per second
PCC	Phantom camera control software
EDR	Extreme dynamic range time
LED	Light emitting diode
pix	Pixel
CVC	Constant volume combustion

MCDI	Methane chemistry dominating ignition
HCDI	Hydrogen chemistry dominating ignition
CCMHDI	Combined chemistry methane and hydrogen dominating ignition
RMI	Richtmyer-Meshkov instability
RTI	Rayleigh-Taylor instability
DDT	Deflagration-to-detonation transition process
FFT	Fast Fourier transform

NOMENCLATURE

C	Speed of light in a medium
C_o	Speed of light in a vacuum
C_i	Driver length of the shock tube setup
n	Local index of refraction
n_o	Index of refraction of the medium at 1 atm and 0 °C
K	Kelvin
ρ	Density
ρ_o	Density of the medium at 1 atm and 0 °C
ρ_i	Density of ith region
ϕ	Incident light angle change
τ_{light}	Light travelling time
$\tau_{rupture}$	Diaphragm rupture moment
$\tau_{PT1\ peak}$	First pressure rise time of PT1 pressure record
$\tau_{PT2\ peak}$	First pressure rise time of PT2 pressure record
τ_{ig}	Ignition delay time
τ_{comb}	Combustion time
θ	Incident light angle
f	Focal length of lens
l	Distance between lenses
L	Test region length
$L_{main\ chamber}$	Main chamber length
h	Size of a light source
Φ	Equivalence ratio
Ψ	Fuel ratio by volume

P	Pressure
P_n	Partial pressure of the nth component in a mixture
P_i	Pressure of ith region
$P_{ambient}$	Ambient pressure
χ_i	Mixture concentration in mole fractions
$(A/F)_{actual}$	Actual air/fuel mass ratio
$(A/F)_{stoic}$	Stoichiometric air/fuel mass ratio
N_i	The number of moles of a component i
MW_i	Molecular weight of a compoenet i
V_m	Main chamber volume
V_{ex}	External chamber volume
T	Temperature
$T_{ambient}$	Ambient temperature
T_i	Temperature of ith region
R	Gas constant
$\bar{R}$	Universal gas constant
D	Inner diameter of the pressure prove
V_T	Tap volume at the interface of the transducer and the line
γ	Specific heat ratio
a	Speed of sound
a_i	Speed of sound of ith region
M	Mach number
M_s	Mach number of the initial shock wave
M_R	Mach number of the reflected shock wave
M_i	Mach number of ith region
u	Gas velocity
u_s	Gas velocity behind the initial shock wave
u_R	Gas velocity behind the reflected shock wave
u_i	Gas velocity of ith region

U	Speed
$U_{initial\ shock}$	Propagation speed of initial shock wave
h_i	Enthalpy of ith region
e	Internal energy
C_p	Specific heat coefficient at constant pressure
A	Arrhenius constant
E	Global activation energy
ε	Length of the interface perturnation
ε_o	Initial perturbation amplitude
λ	Channel width
k	Wave number of the perturbation
At	Atwood number

ABSTRACT

Paik, Kyong-Yup. M.S.M.E., Purdue University, December 2016. Experimental Investigation of Hot-Jet Ignition of Methane-Hydrogen Mixtures in A Constant-Volume Combustor. Major Professor: M. Razi Nalim.

Investigations of a constant-volume combustor ignited by a penetrating transient jet (a puff) of hot reactive gas have been conducted in order to provide vital data for designing wave rotor combustors. In a wave rotor combustor, a cylindrical drum with an array of channels arranged around the axis spins at a high rpm to generate high-temperature and high-pressure product gas. The hot-gas jet ignition method has been employed to initiate combustion in the channels.

This study aims at experimentally investigating the ignition delay time of a premixed combustible mixture in a rectangular, constant-volume chamber, representing one channel of the wave rotor drum. The ignition process may be influenced by the multiple factors: the equivalence ratio, temperature, and the composition of the fuel mixture, the temperature and composition of the jet gas, and the peak mass flow rate of the jet (which depends on diaphragm rupture pressure). In this study, the main mixture is at room temperature. The jet composition and temperature are determined by its source in a pre-chamber with a hydrogen-methane mixture with an equivalent ratio of 1.1, and a fuel mixture ratio of 50:50 (CH_4:H_2 by volume). The rupture pressure of a diaphragm in the pre-chamber, which is related to the mass flow rate and temperature of the hot jet, can be controlled by varying the number of indentations in the diaphragm. The main chamber composition is varied, with the use of four equivalence ratios (1.0, 0.8, 0.6, and 0.4) and two fuel mixture ratios (50:50, and 30:70 of CH_4:H_2 by volume).

The sudden start of the jet upon rupture of the diaphragm causes a shock wave that precedes the jet and travels along the channel and back after reflection. The shock strength has an important role in fast ignition since the pressure and the temperature are increased after the shock. The reflected shock pressure was examined in order to check the variation of the shock strength. However, it is revealed that the shock strength becomes attenuated compared with the theoretical pressure of the reflected shock. The gap between theoretical and measured pressures increases with the increase of the Mach number of the initial shock.

Ignition delay times are obtained using pressure records from two dynamic pressure transducers installed on the main chamber, as well as high-speed videography using flame incandescence and Schileren imaging. The ignition delay time is defined in this research as the time interval from the diaphragm rupture moment to the ignition moment of the air/fuel mixture in the main chamber. Previous researchers used the averaged ignition delay time because the diaphragm rupture moment is elusive considering the structure of the chamber. In this research, the diaphragm rupture moment is estimated based on the initial shock speed and the longitudinal length of the main chamber, and validated with the high-speed video images such that the error between the estimation time and the measured time is within 0.5%. Ignition delay times decrease with an increase in the amount of hydrogen in the fuel mixture, the amount of mass of the hot-jet gases from the pre-chamber, and with a decrease in the equivalence ratio.

A Schlieren system has been established to visualize the characteristics of the shock wave, and the flame front. Schlieren photography shows the density gradient of a subject with sharp contrast, including steep density gradients, such as the flame edge and the shock wave. The flame propagation, gas oscillation, and the shock wave speed are measured using the Schlieren system. An image processing code using MATLAB has been developed for measuring the flame front movement from Schlieren images.

The trend of the maximum pressure in the main chamber with respect to the equivalence ratio and the fuel mixture ratio describes that the equivalence ratio 0.8

shows the highest maximum pressure, and the fuel ratio 50:50 condition reveals lower maximum pressure in the main chamber than the 30:70 condition.

After the combustion occurs, the frequency of the pressure oscillation by the traversing pressure wave increases compared to the frequency before ignition, showing a similar trend with the maximum pressure in the chamber. The frequency is the fastest at the equivalence ratio of 0.8, and the slowest at a ratio of 0.4. The fuel ratio 30:70 cases show slightly faster frequencies than 50:50 cases. Two different combustion behaviors, fast and slow combustion, are observed, and respective characteristics are discussed. The frequency of the flame front oscillation well matches with that of the pressure oscillation, and it seems that the pressure waves drive the flame fronts considering the pressure oscillation frequency is somewhat faster. Lastly, a feedback mechanism between the shock and the flame is suggested to explain the fast combustion in a constant volume chamber with the shock-flame interactions.

1. INTRODUCTION

1.1 History of Wave Rotor Developments

Endeavors to develop wave rotor technology have been made since the beginning of the 20th century [1, 2]. The earliest concept proposed by Knauff in 1906 was the pressure exchanger, which exchanges pressures between the inlet and outlet ports using a rotating cellular drum [3]. Burghard in 1913 [4], and Lebre in 1928 [5] also suggested pressure exchanger concepts, but like Knauff those did not utilize pressure waves in channels. Burghard in 1928 proposed the first wave rotor concept using pressure waves in both the compression and expansion process [6]. The first industrial application of the pressure-exchange wave rotor was designed by Claude Seippel (1940) of Brown Boveri Company, which was used as a high-pressure stage for a British Railways locomotive gas turbine [7]. A more developed model, a pressure wave super-charger for diesel engines, was first manufactured by the ITE Circuit Breaker Company in the U.S. [8]. This successful application led to the development of passenger car diesel engine superchargers by Comprex, being used in several car manufacturers such as Opel, Mazda, Mercedes-Benz, Peugeot, and Ferrari until the late 1980s [9]. Developments of wave rotor technology as gas turbine applications have progressed in parallel with car engines. Jendrassik in 1956 [10] proposed the wave rotor as a high-pressure stage of early aircraft engines, and a unique wave rotor was designed by Pearson in 1983, which has helical channels to produce shaft work [11]. Another new concept of the wave rotor was studied by General Electric Company in 1956 [12] that combustion occurs inside the rotor channels, enabling a reduction in the size and weight of the engines. Rolls-Royce began the research on the wave rotor in the mid-1960s to design a small helicopter engine [13]. From the late 1980s to present, working with Cornell University and NASA Glenn Research Center, Rolls-

Royce in Indianapolis, USA, has worked on wave rotor technology for future aircraft propulsion systems [14]. The present effort at Indiana University Purdue University Indianapolis has benefited from long-standing collaborations with Rolls-Royce and NASA Glenn.

1.2 Operating Principle of Wave Rotor Combustors

Skimming through the history of the wave rotor development shows that the wave rotor can be classified in two forms: the pressure exchange wave rotor, and the wave rotor combustor. The main purpose of the former is to exchange different pressure levels between fluids. Due to the sudden opening and closing ports, compression and expansion waves are generated, acting like a piston. Further information regarding the pressure exchange wave rotor is described in [15]. The later one, the wave rotor combustor, is the model for the current study that has a similar condition with the pressure exchanger that gas dynamic waves play a vital role in the channels. However, the key feature is that it includes a constant-volume combustion process, which is the purpose of the wave rotor combustor.

When constant-volume combustion is substituted for the constant-pressure combustion process of a Brayton cycle engine, it becomes the Humphrey thermodynamic cycle [16]. Figure 1.1 illustrates temperature-entropy (T-s) diagrams of the Humphrey cycle (1-2-3-4) and the Brayton cycle (1-2-3b-4b) for fixed inlet temperatures and outlet pressures. Considering heat addition processes for both cycles, the Humphrey cycle follows a constant-volume heat addition line (2-3) while the Brayton cycle follows a constant-pressure heat addition line (2-3b). This difference causes the Humphrey cycle to gain pressure, and reduce the entropy production compared to the Brayton cycle, yielding greater system power output and cycle efficiency for fixed energy input. According to Akbari [15], the ideal Humphrey cycle represents about 25% reduction in entropy production with respect to the same temperature condition of the Brayton cycle, presenting considerable thermodynamic efficiency potential.

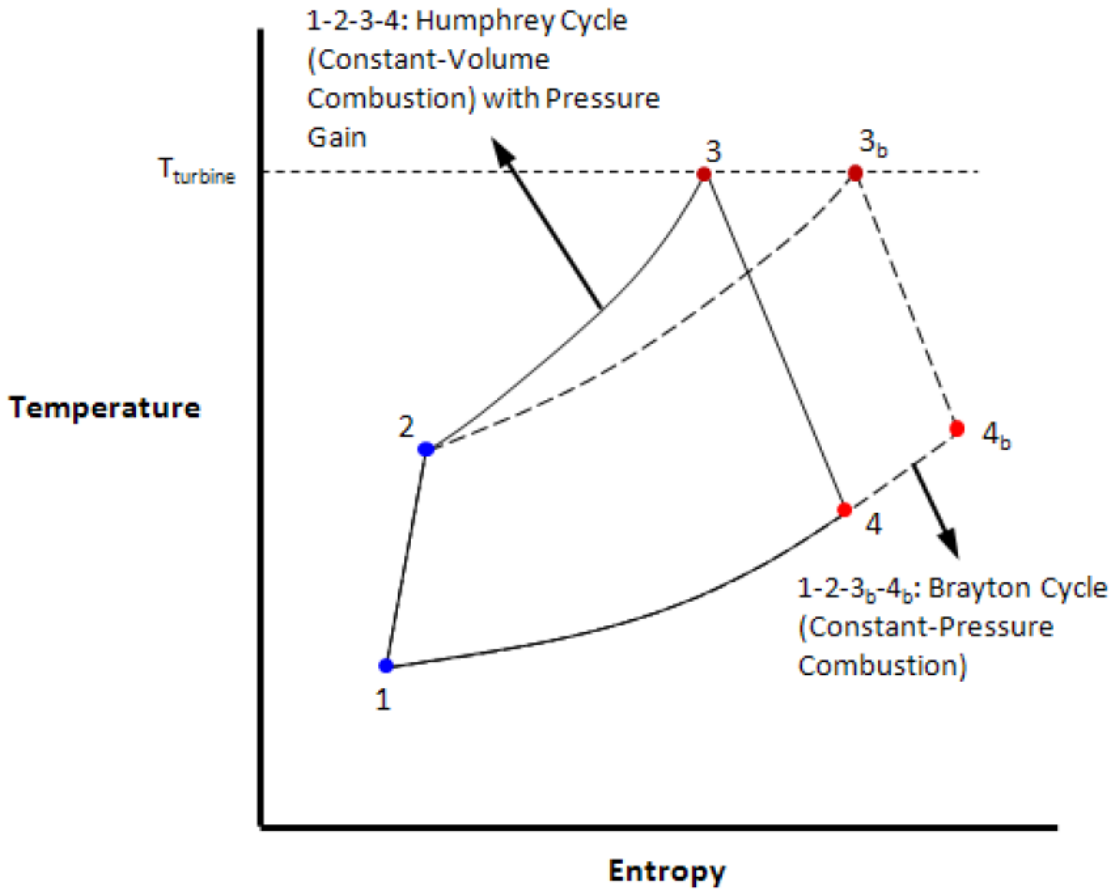

Fig. 1.1. Comparison of Humphrey cycle (1-2-3-4) with Brayton cycle (1-2-3b-4b) [17]

The wave rotor combustor consists of a cylindrical drum with an array of channels arranged around the axis, two stationary endplates with the partial-annular inlet and outlet ports, and an ignitor on the exit endplate as shown in Figure 1.2. Figure 1.3 illustrates the operating cycle of a simple wave rotor combustor, showing a successive process taking place inside a single channel. A rotating motion of a channel is expressed as a vertical motion in the upwards direction. This explanation for the process begins at the state that both inlet and outlet ports open. The channel is filled with an air/fuel mixture through the inlet port, and releases the product gas of high pressure and temperature through the exit port. As the channel moves upward, the outlet port is suddenly closed, creating a compressive wave, often referred to as a hammer shock, which propagates from the outlet port to the inlet port, but the inlet port is closed just as the hammer shock arrives, trapping the compressed mixture in the channel [18]. Figure 1.3 shows a hypothetical ignition event occurring in the center of the channel, but a more practical ignition method is the use of a transient jet or puff of hot gas injected from a torch igniter at one end wall or both end walls. When the channel reaches the torch ignitor, the mixture is ignited by mixing of mixture with hot gas, and completely combusted under the constant-volume condition at state B, obtaining higher temperature and pressure compared to the constant-pressure condition as discussed above. When the channel arrives at the outlet port, the sudden pressure drop generates expansion waves propagating toward the inlet port, accelerating the purging process of the product gas through the outlet port. The inlet port is precisely located to use the pressure rarefaction by expansion waves, helping the fresh air/fuel mixture sweep into the channel after the state C, and then the state of the channel returns to the beginning. Considering the time scales of the inherent gas dynamic process, rapid ignition and combustion are required. This also helps reduce nitrogen oxide (NOx) emissions of the product gas [19].

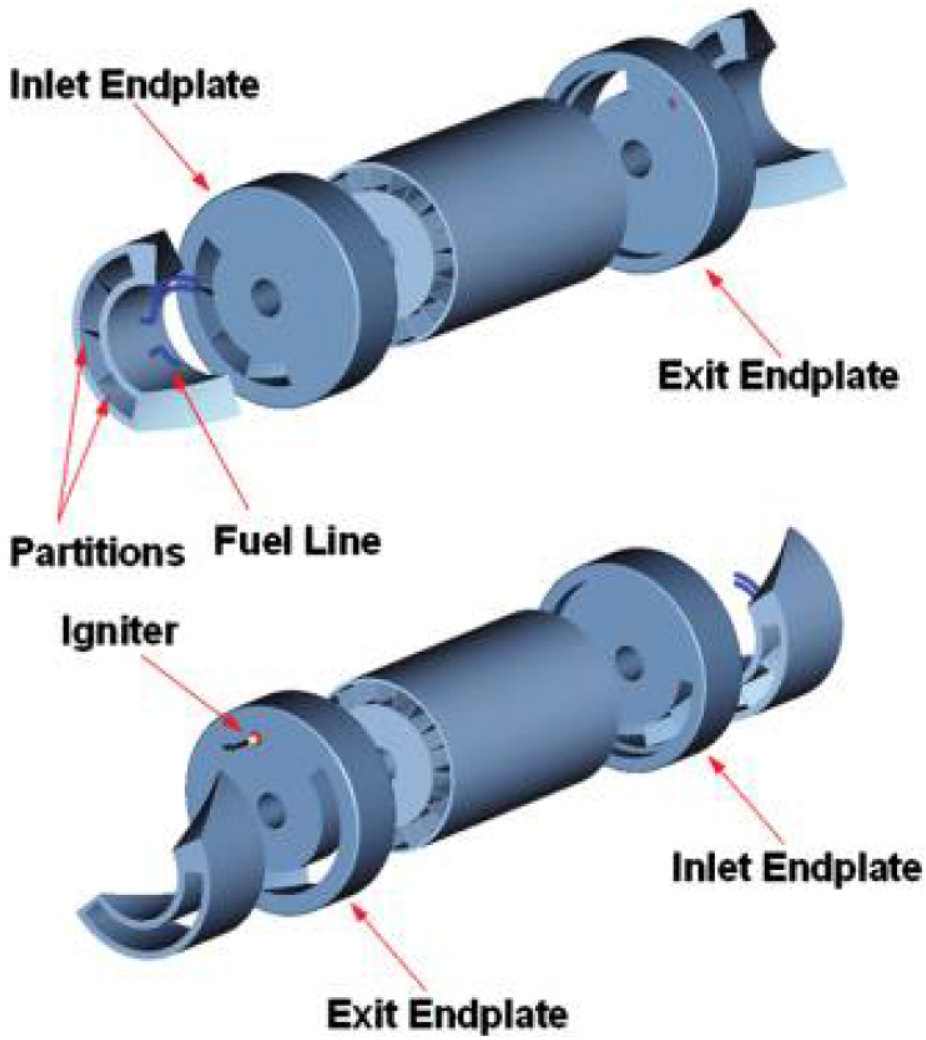

Fig. 1.2. Schematic configuration of a wave rotor combustion from inlet (top) and exit (bottom) views [15]

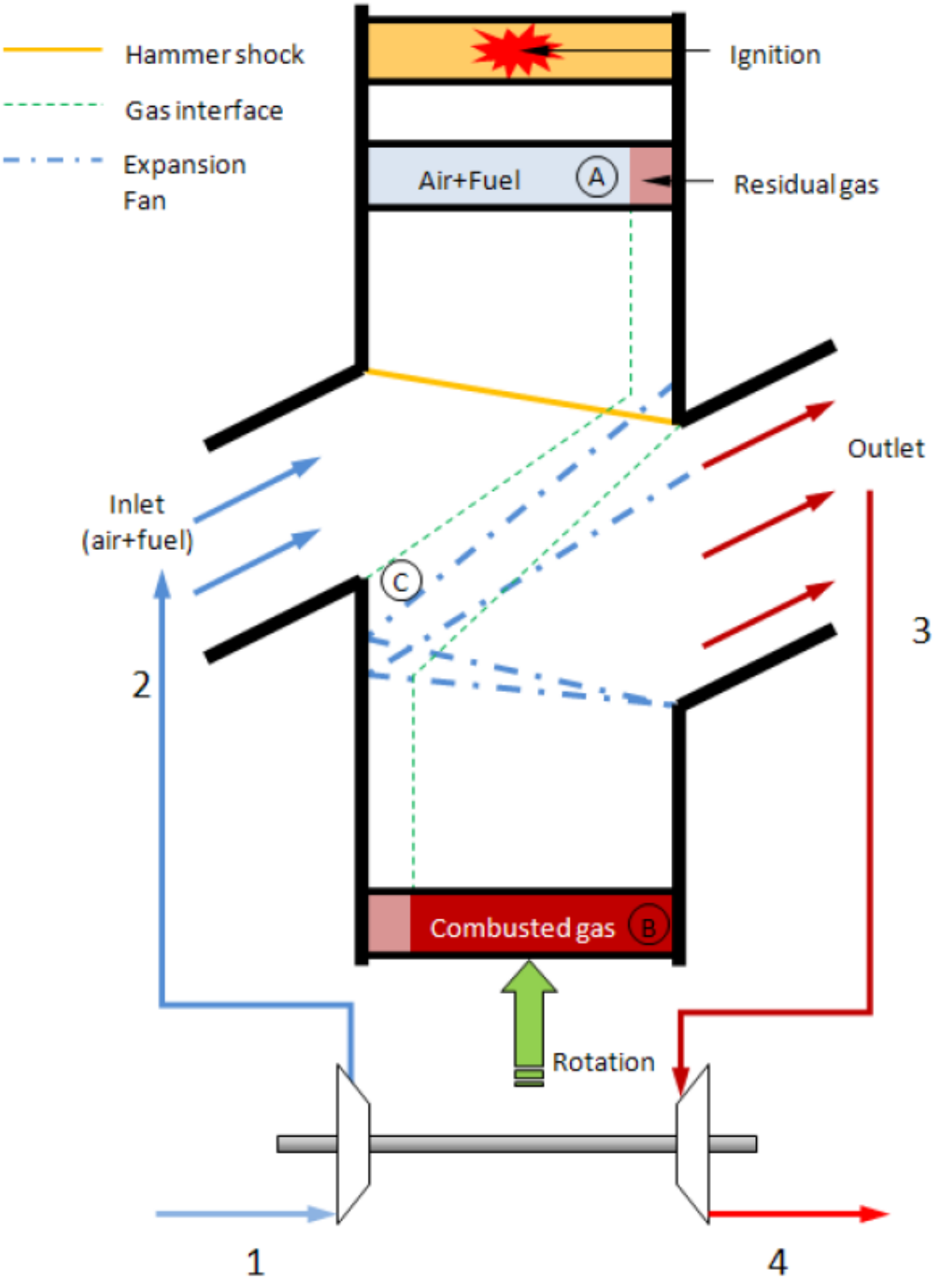

Fig. 1.3. Schematic developed view of a wave-rotor combustor [17]

1.3 Previous Research

1.3.1 Hot-Jet Ignition

For rapid ignition, or short ignition delay time, the hot-jet ignition method has been shown to be effective for premixed combustible mixtures in basic experiments where a pre-chamber is used to supply the jet. Fast turbulent mixing in the jets create a substantial mass of ignitable mixture that can ignite quickly with the help of chemically active radicals from the torch igniter. Thus it is more energetic than the conventional spark ignition method [20]. Higelin [21] and Ma [22] also reported that radical injection with high energy from the pre-chamber can overcome the relatively slow combustion velocity in lean mixtures. Elhsnawi [23] who experimentally investigated the hot inert gas (argon or nitrogen) injection into a hydrogen-oxygen mixture reported that ignition occurs in the turbulent mixing zone at the edge of the jet. However, in experiments of hot jet ignition using hydrogen/air (27% / 72% by volume) mixtures for both chambers, Sadanandan [24] observed that ignition occurs near the jet tip, and not at the lateral sides of the jet. Iglesias [25] indicated that ignition is more dependent on variations in the diffusivity of the reactant than the jet Reynolds number. In other words, ignition tends to occur in the lateral sides of the jet when the Lewis number of the reactant, which represents the ratio of thermal diffusivity to mass diffusivity of the reactant mixture, is of the order of, or larger than unity, while ignition occurs in the jet tip for very diffusive fuels, like hydrogen, with the Lewis number smaller than unity. Bilgin [26] developed a test rig for the constant-volume combustion experiment, which consists of a rotary pre-chamber and a stationary main chamber. The author proposed a correlation between the Damkohler number, which characterizes the ratio of the flow time scale to the chemical time scale, and ignition of an air/fuel mixture. According to the author, the far-field and long-pulse Damkohler numbers were more suitable to predict ignition success for the stationary experiments, and temperature of the jet had more influence on the ignition than the effect of nozzle geometry. From the previous literature research on the hot-jet ignition, the Lewis

number, the Damkohler number, amounts of radicals in the jet, and temperature of the jet simultaneously determine ignitability in a constant-volume channel.

1.3.2 Ignition Delay Time

The ignition delay time is a fundamental characteristic parameter for understanding combustion initiation. The ignition mechanism can include physical and chemical reaction processes, and requires knowledge of physical transport models and chemical kinetic models. The definition of ignition delay time varies with physical conditions of the experiment in that the direct cause of ignition is diverse for each condition. The ignition delay time in a diesel engine is defined as the time interval between the start of injection and the ignition, which includes two simultaneous delays, a physical delay of atomization, vaporization, and mixing of air/fuel, and a chemical delay attributed to pre-combustion reactions [27]. For the shock tube ignition experiments using premixed reactants, the ignition delay time is pure chemical. It is defined as the time interval between the arrival of the primary shock wave at the end wall and the measured pressure spike due to ignition, as illustrated in Figure 1.4 [28], since the ignition is induced by temperature and density rise from the reflected shock wave. In hot-jet studies, considering that the ignition occurs by the hot-reactive jet, the ignition delay time is defined as the time from jet initiation to the ignition moment in the constant-volume chamber [17].

The ignition delay time is a fundamental characteristic parameter for understanding the ignition mechanism, analyzing the chemical reaction process, and validating chemical kinetic models. The definition of ignition delay time varies with physical conditions of the experiment in that the direct cause of ignition is diverse for each condition. The ignition delay time in a diesel engine is defined as the time interval between the start of injection and the ignition, which includes two simultaneous delays, a physical delay of atomization, vaporization, and mixing of air-fuel, and a chemical delay attributed to pre-combustion reactions [27]. For the shock tube igni-

tion experiments, the ignition delay time is defined as the time interval between the arrival of the primary shock wave at the end wall and the arrival of the Von Neumann spike due to ignition, as illustrated in Figure 1.4 [28], since the ignition is induced by pressure and temperature rises from the reflected shock wave. In hot-jet studies, considering that the ignition occurs by the hot-reactive jet, the ignition delay time is defined as the time from jet initiation to the ignition moment in the constant-volume chamber [17].

The ignition event can be identified from a pressure trace with high time-resolution using a dynamic pressure transducer, or measuring the emission of specific species such as OH, CH, and C_2 radicals using a photomultiplier, or a CCD camera with spectral filters. Davidson [29] reported that a sudden pressure rise is a good indicator of the ignition event in general, and CH and OH mole fraction histories can be a clear sign of ignition. In this study, the definition of the ignition delay time used by Perera [17] has been applied. It is measured using pressure traces, and validated by high speed video images.

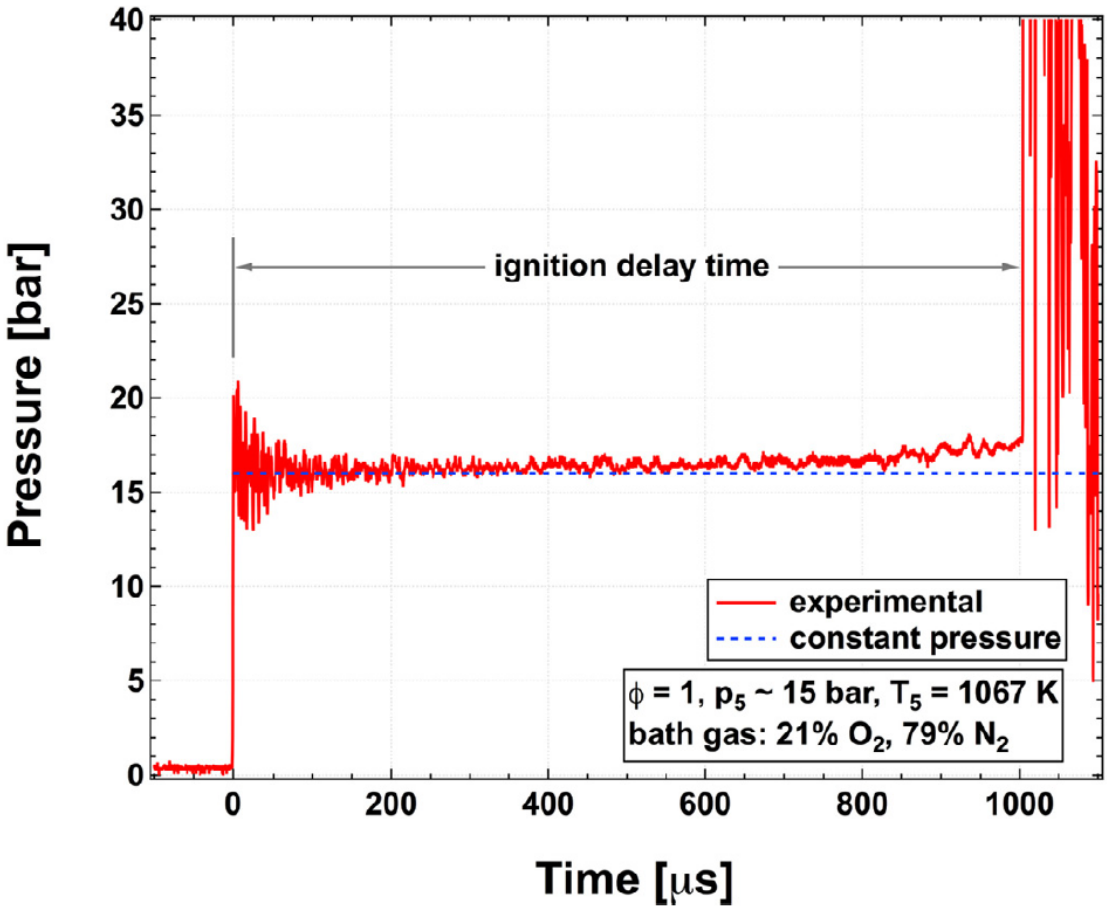

Fig. 1.4. An example of end wall pressure trace from a shock tube experiment [28]

1.3.3 Lean Premixed Methane-Hydrogen-Air Flames

The combustion of natural gas produces fewer emissions of carbon related species compared to that of gasoline and the other gas oil fuels [30]. Thus, natural gas is admitted as one of the beneficial fuels for engines and industrial boilers. Methane, the main component of natural gas, had been considered as a main fuel for this research in that it is more abundant than other hydrocarbon fuels, such as ethylene and propane. However, methane has some drawbacks, such as slow burning velocity, low thermal efficiency, and poor lean-burn capability, which reduce the engine power output and the fuel efficiency [31, 32].

The operating temperature of the actual wave rotor is much higher than room temperature because the channel walls are heated up by the combustion processes and there is hot residual gas after the outlet ports are closed. Therefore, temperature of the fresh mixture increases by heat transfer from the walls and mixing with hot residual gas. This higher initial temperature condition allows a methane-air mixture to create a faster kinetic regime in which we are interested. In order to simulate the fast ignition chemical kinetics using methane in a laboratory condition without increasing the initial temperature, mixing methane with a fuel having a characteristic of high burning velocity can be one of solutions. Hydrogen has been considered as a feasible additive to enhance the combustion of methane due to its high burning speed, which can speed up the combustion process of methane [33, 34]. Thus, the hydrogen-methane-air mixture is selected as a reactant blend for the current study.

Zhang [35] performed experimental and modeling investigations on chemical auto-ignition characteristics of methane/hydrogen mixtures. Hydrogen mole fraction was varied from 0 to 100% in shock tube experiments, pressure was kept 1.8 MPa, and temperature behind reflected shock waves were in the range of 900-1750 K. Equivalence ratios, 0.5, 1.0, and 2.0 were investigated. USC Mech 2.0 was selected to conduct sensitivity analysis. At T=1400 K, and 80% CH_4/20% H_2 conditions, R1, R93, R96 are the main ignition promotion reactions. The sensitivity coefficients of

ignition promotion reactions R1 decreases with an increase in equivalence ratio, thus the chain branching efficiency is inhibited through reaction R1, decreasing the accelerated rate of total reaction. The reactions R93 and R96, which produce CH_3O radical, promote the ignition since free radicals, O and OH, are produces by consuming the CH_3 radical respectively. The sensitivity coefficient of these reactions, R93 and R96, also decrease with an increase in the equivalence ratio, leading to the weakening on accelerated ignition tendency. Overall, the ignition of the mixtures is inhibited with an increase in the equivalence ratio, which is consistent to the experimental results in Figure 1.5. At lower temperatures, T=930K, R96 plays a vital role as the ignition promotion reaction, and the sensitivity coefficient of R96 decreases with an increase in the equivalence ratio, weakening the ignition promotion effect at higher equivalence ratios. Other ignition promotion reactions, R86 and R94, also show the similar tendency with R96. The chain termination reaction R104 plays as the ignition inhibition reaction, and its sensitivity coefficient increases with an increase in the equivalence ratio, restricting ignition. Therefore, the ignition delay time is increased with an increase in the equivalence ratio for low temperatures.

$$H + O_2 \iff O + OH \tag{R1}$$

$$OH + OH + M \iff H_2O_2 + M \tag{R14}$$

$$HO_2 + HO_2 \iff O_2 + H_2O_2 \tag{R19}$$

$$H_2O_2 + H \iff HO_2 + H_2 \tag{R25}$$

$$CH_2O + HO_2 \iff HCO + H_2O_2 \tag{R86}$$

$$CH_3 + O_2 \iff O + CH_3O \tag{R93}$$

$$CH_3 + O_2 \iff OH + CH_2O \tag{R94}$$

$$CH_3 + HO_2 \iff CH_3O + OH \tag{R96}$$

$$CH_3 + H_2O_2 \iff CH_4 + HO_2 \tag{R97}$$

$$CH_3 + CH_3 + M \iff C_2H_6 + M \tag{R104}$$

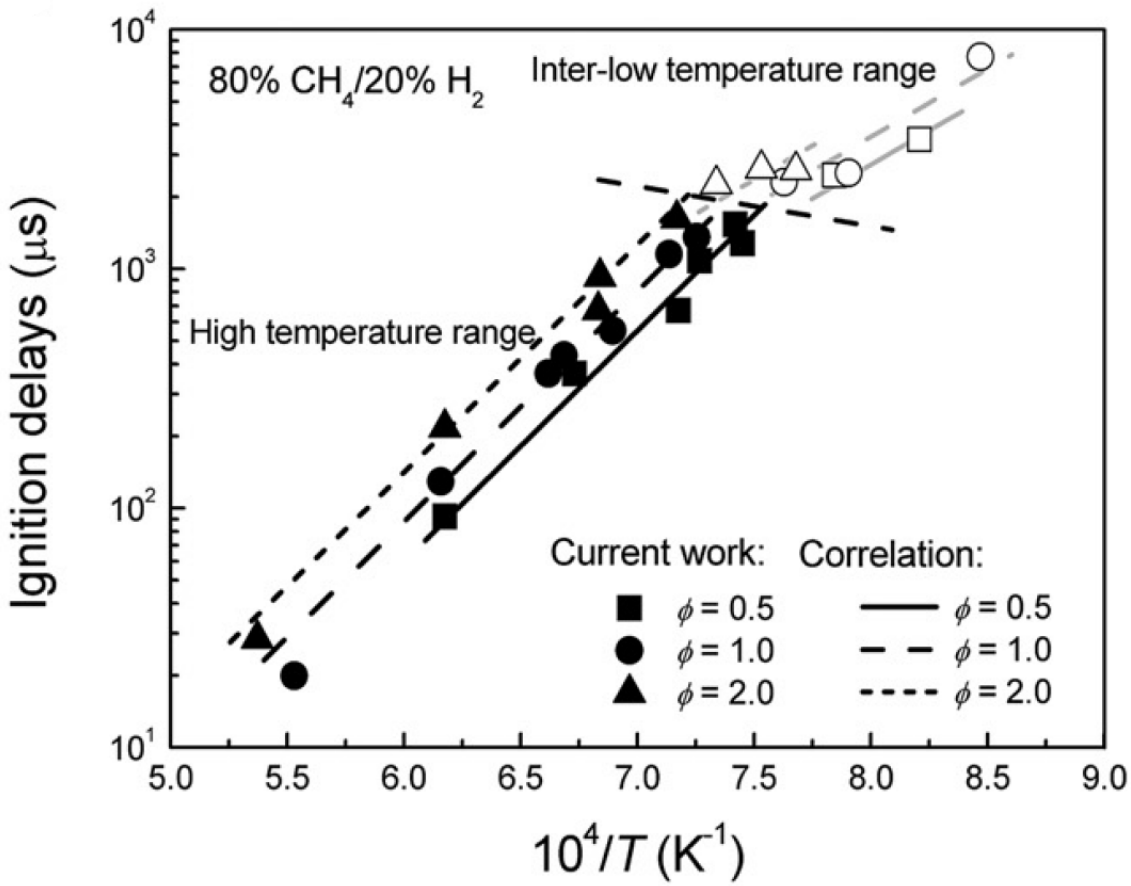

Fig. 1.5. Effects of equivalence ratio on ignition for methane dominating ignition, 80% CH_4/20% H_2 [35]

At T=1400 K, and 40% CH_4/60% H_2 conditions, most of key elementary reactions are from methane chemistry; therefore, the tendency of the ignition delay time on the equivalence ratio is similar to the reaction system in methane chemistry dominating ignition. At T=930 K, and 40% CH_4/60% H_2 conditions, however, the hydrogen chemistry becomes more important. The termolecular reaction R14, producing the H_2O_2 radical, provides the contributions toward two different aspects. R25 and R97, which enhance the ignition, are promoted, and the sensitivity coefficient of those increases with an increase in the equivalence ratio, enhancing the ignition promotion effect. At the same time, the ignition inhibition reaction R19 is also promoted by R25 generating HO_2, and the sensitivity coefficient of R19 increases with an increase in the equivalence ratio, weakening the ignition promotion effect. As a result, the ignition delay time is insensitive to the equivalence ratio at low temperatures for the 40% CH_4/60% H_2 mixture, this is validated by the experimental results in Figure 1.6. To summarize, the ignition delay time increases with the increase of the equivalence ratio under conditions where the methane chemistry dominates the ignition regime. The ignition delay time is relatively insensitive to the equivalence ratio under conditions where the combined chemistry of methane and hydrogen dominates ignition regimes.

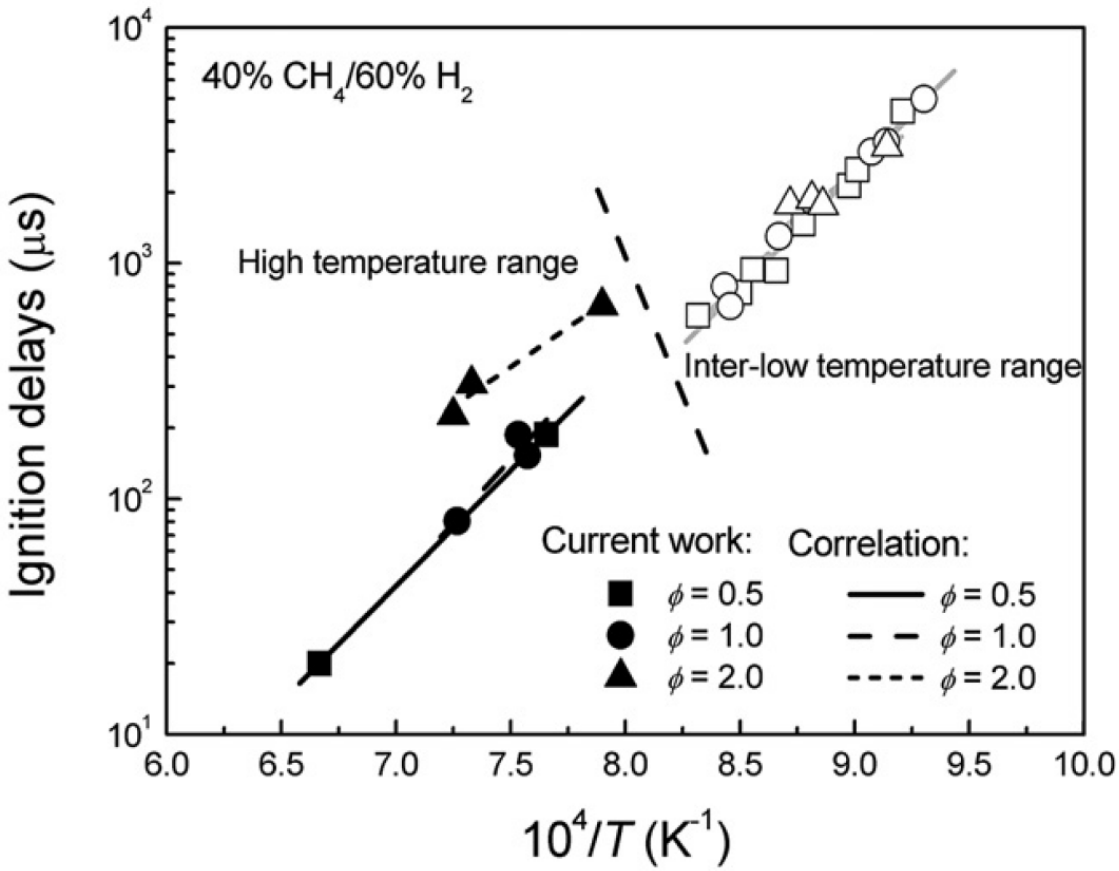

Fig. 1.6. Effects of equivalence ratio on ignition for hydrogen and methane dominating ignition, 40% CH_4/60% H_2 [35]

1.3.4 Schlieren Photography Technique

Schlieren imaging systems have been primarily applied to conduct qualitative visual studies as a straightforward tool, providing an informative, non-intrusive method for studying phenomena in transparent optically accessible media [36]. Since this technique is sensitive to density changes, and does not interfere with flow, it has been widely used in fluid dynamics studies [37, 38]. In order to measure the flame propagation speed, and the interaction between shock waves and the flame front, Schlieren photography technique is selected for the current research. Schlieren photography enables images to be obtained of light intensity variation due to the deflection of light rays by density gradients of the object as illustrated in Figure 1.7.

When light passes a medium with density, the speed of light can be expressed as [39]:

$$C = C_0/n \tag{1.1}$$

where C is a speed of light in a medium, C_0 is a speed of light in a vacuum (C_0=3∗10^8 m/s), and n is a local index of refraction. The refraction index is a function of density [39],

$$n = 1 + (n_0 - 1)(\rho/\rho_0) \tag{1.2}$$

where n_0 is index of refraction of the medium at 1 atm and 0 °C, and ρ_0 is density of the medium at 1 atm and 0 °C. The refraction index is always higher than unity, so the speed of light in a medium is slower than the speed of light in a vacuum. If two light rays pass a medium with a density gradient like Figure 1.8, speeds of two light rays are different due to the density difference.

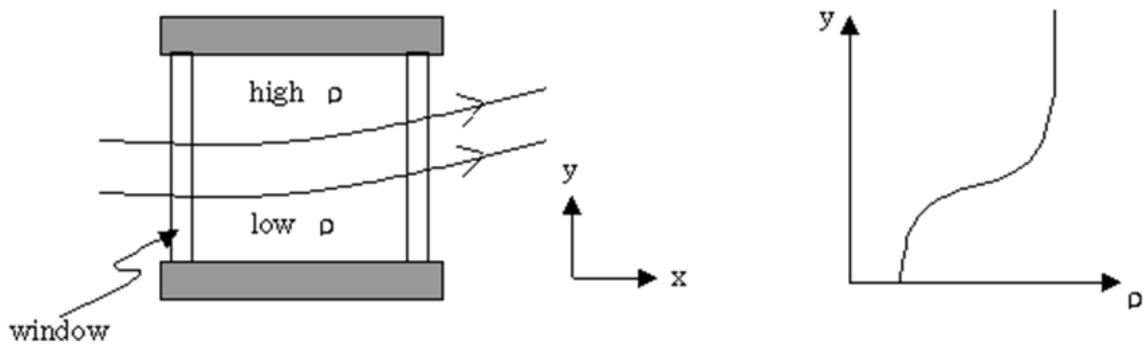

Fig. 1.7. Light ray deflection by density gradients

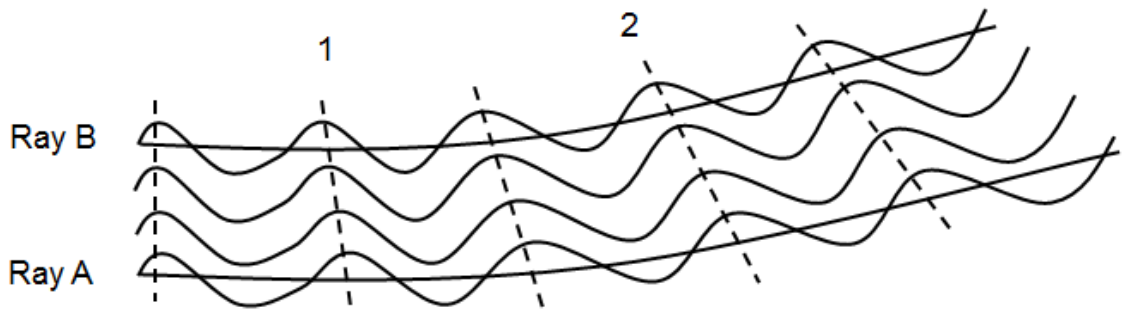

Fig. 1.8. The variation of the speeds of two light rays by the density difference

This speed variation yields an angle change between point 1 and 2 like Figure 1.9, which can be expressed as:

$$d\phi = \phi_2 - \phi_1 = \frac{\tau_{light}(C_A - C_B)}{dy} = \tau_{light}(-\frac{dC}{dy}) \tag{1.3}$$

and the light travelling time τ_{light} is:

$$dx = \tau_{light}\frac{C_A + C_B}{2} = \tau_{light} * C \tag{1.4}$$

$$\tau_{light} = \frac{dx}{C} \tag{1.5}$$

Applying Eq. (1.5) to Eq. (1.3) gives,

$$d\phi = \frac{dx}{C}(-\frac{C}{y}) \tag{1.6}$$

or,

$$\frac{d\phi}{dx} = -\frac{1}{C}\frac{dC}{dy} \tag{1.7}$$

From Figure 1.9,

$$tan\phi \approx \phi = \frac{dy}{dx} \tag{1.8}$$

$$\frac{d\phi}{dx} = \frac{d^2y}{dx^2} \tag{1.9}$$

Applying Eq. (1.9) to (1.7) gives,

$$\frac{d^2y}{dx^2} = -\frac{1}{C}\frac{dC}{dy} \tag{1.10}$$

and,

$$\frac{dC}{dy} = \frac{dC}{d\rho}\frac{d\rho}{dy} = \frac{-C(\frac{n_0-1}{\rho_0})}{1 + (n_0 - 1)\frac{\rho}{\rho_0}}\frac{d\rho}{dy} \tag{1.11}$$

Applying Eq. (1.11) to Eq. (1.10) gives,

$$\frac{d^2y}{dx^2} = \frac{1}{1+(n_0-1)\frac{\rho}{\rho_0}}\frac{n_0-1}{\rho_0}\frac{d\rho}{dy} \tag{1.12}$$

and,

$$\frac{d^2y}{dx^2} = \frac{n_0-1}{\rho_0}\frac{d\rho}{dy} \tag{1.13}$$

Eq. (1.13) is the light ray equation [40].

If ρ is constant, $\frac{d\rho}{dy} = 0$ from Eq. (1.13); therefore, $\frac{d^2y}{dx^2} = 0$, which gives $y = Ax+B$, that light path is linear in constant density, and this can be used to derive Snell′s law,

$$n_1 sin\theta_1 = n_2 sin\theta_2 \tag{1.14}$$

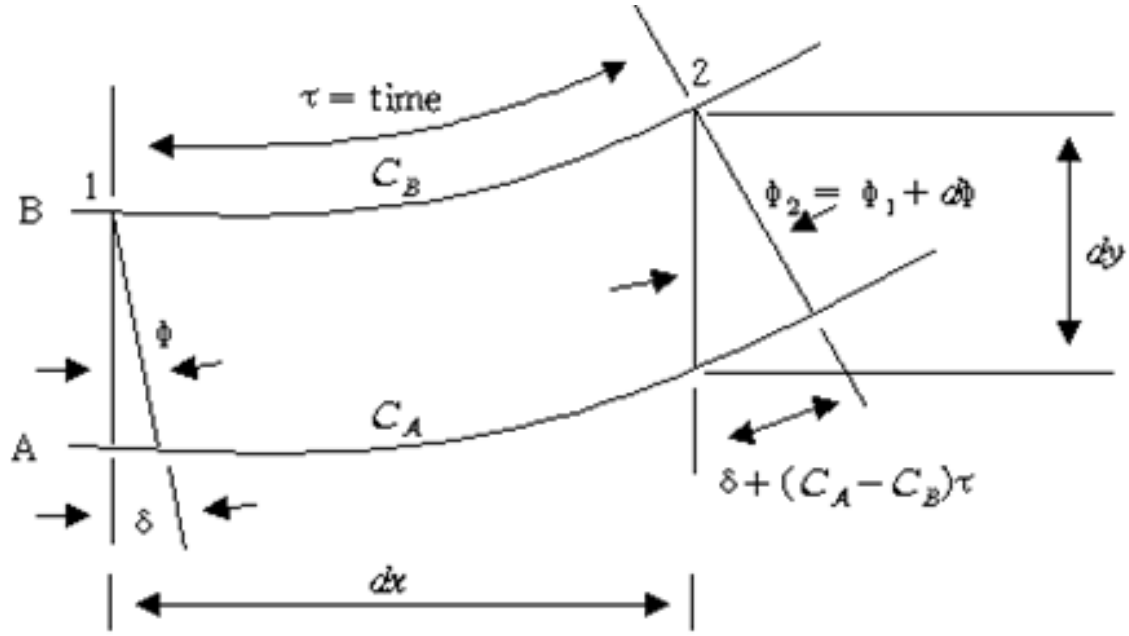

Fig. 1.9. Angle change between point 1 and 2 by the light ray deflection

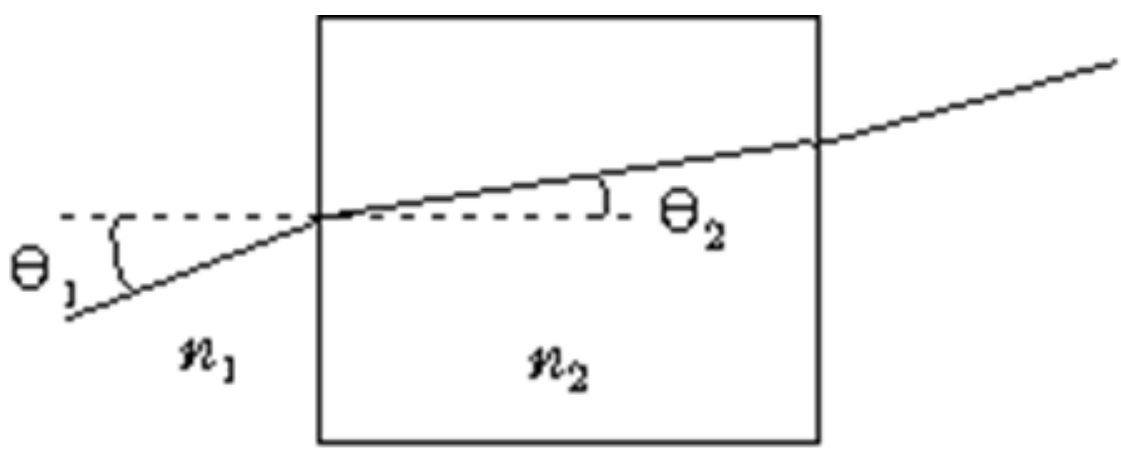

Fig. 1.10. Snell′s law

If parallel light rays pass a medium with a density gradient, as illustrated in Figure 1.11, light rays are overlapped at the higher density region, making a bright line, and there is no light at the lower density region, making a dark line. For the shadowgraph technique, white lines indicate higher density regions, and black lines indicate lower density regions like in Figure 1.12

A typical Schlieren setup, illustrated in Figure 1.13, consists of a light source, two lenses making collimated light, and a knife edge. The knife edge cuts off light rays that are deflected toward it, and illuminace levels of the Schlieren and the shadowgraph methods correspond to the first-order density-gradient and the second-order density-gradient, respectively [41], so the Schlieren technique makes more striking images than the shadowgraph like Figure 1.15. Contrast of a Schlieren image can be expressed as [42]:

$$Contrast = \frac{2f_2 + l}{h_1} \cdot \frac{L(n_0 - 1)}{\rho_0} \cdot \frac{d\rho}{dy} \tag{1.15}$$

where f_2 is a focal length of the second lens, l is a distance between the two lenses, L is a test region length, and h_1 is an original size of the light source. In order to increase contrast, the focal length of the lens, the distance between two lenses, and the density gradient of the object should be larger, and the size of the original light source should be smaller. Considering the effect of h_1, laser light is an ideal point source, and Z-type Schlieren system using two mirrors, as shown in Figure 1.14, is mainly applied to increase f_2 , and l, as much as possible for a limited laboratory space.

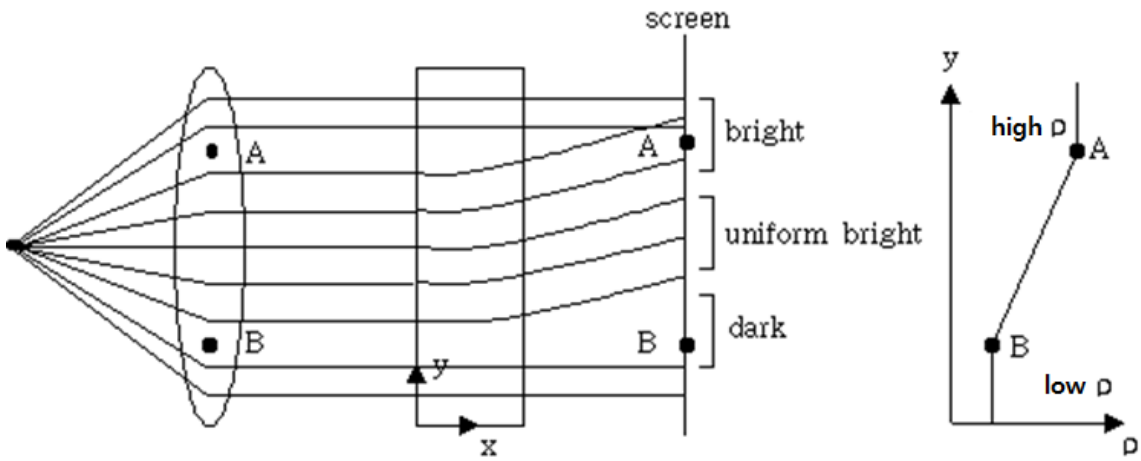

Fig. 1.11. Contrast caused by light deflection

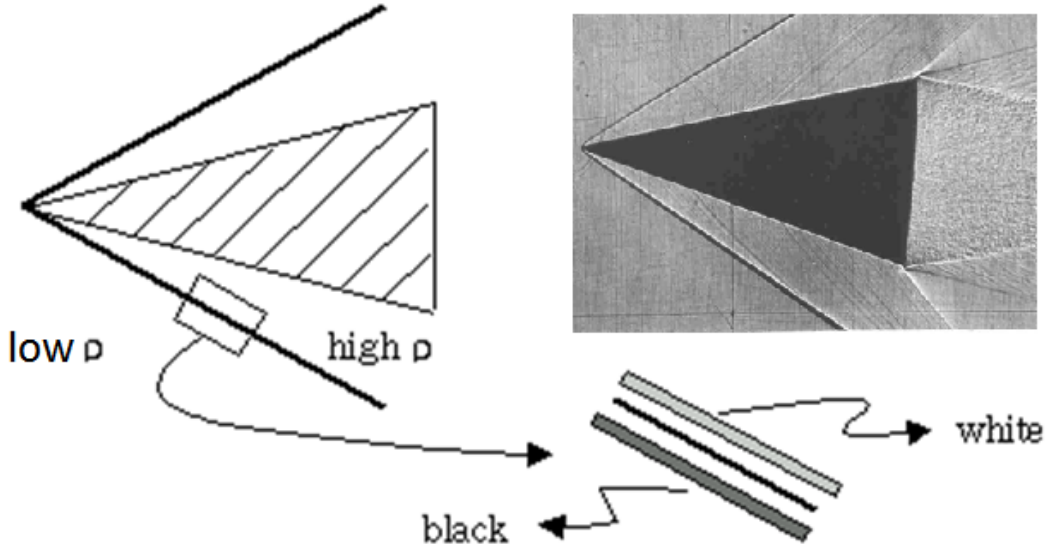

Fig. 1.12. Example of the shadowgraph

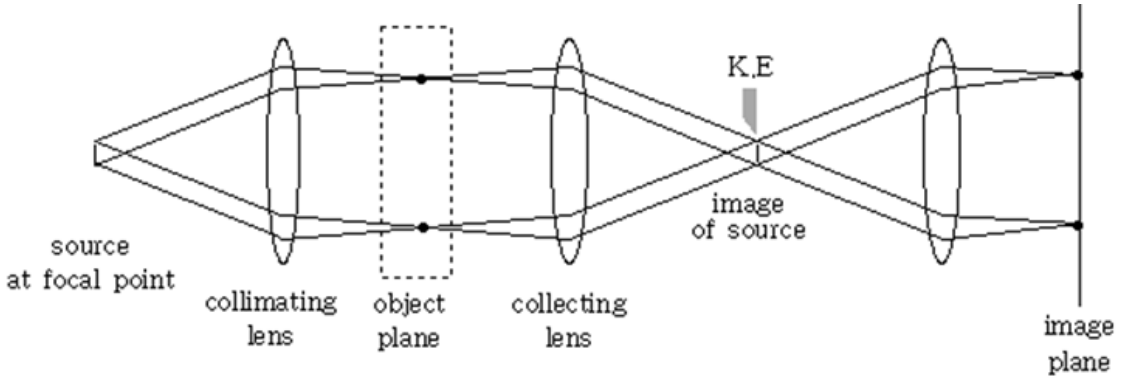

Fig. 1.13. Schlieren setup

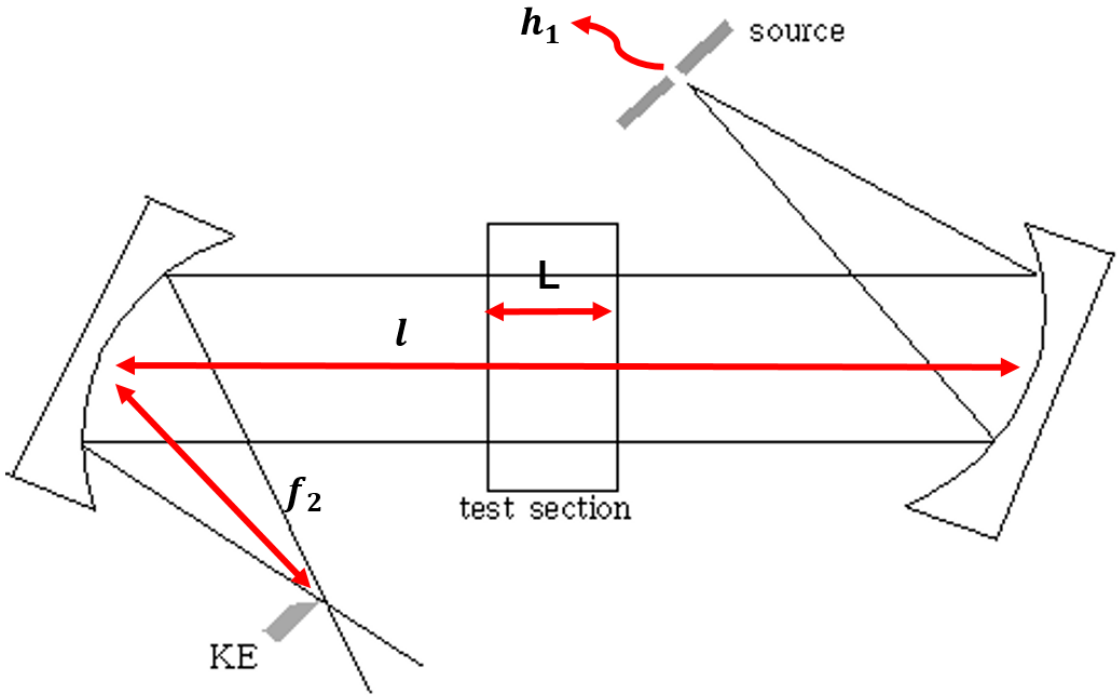

Fig. 1.14. Z-type Schlieren setup

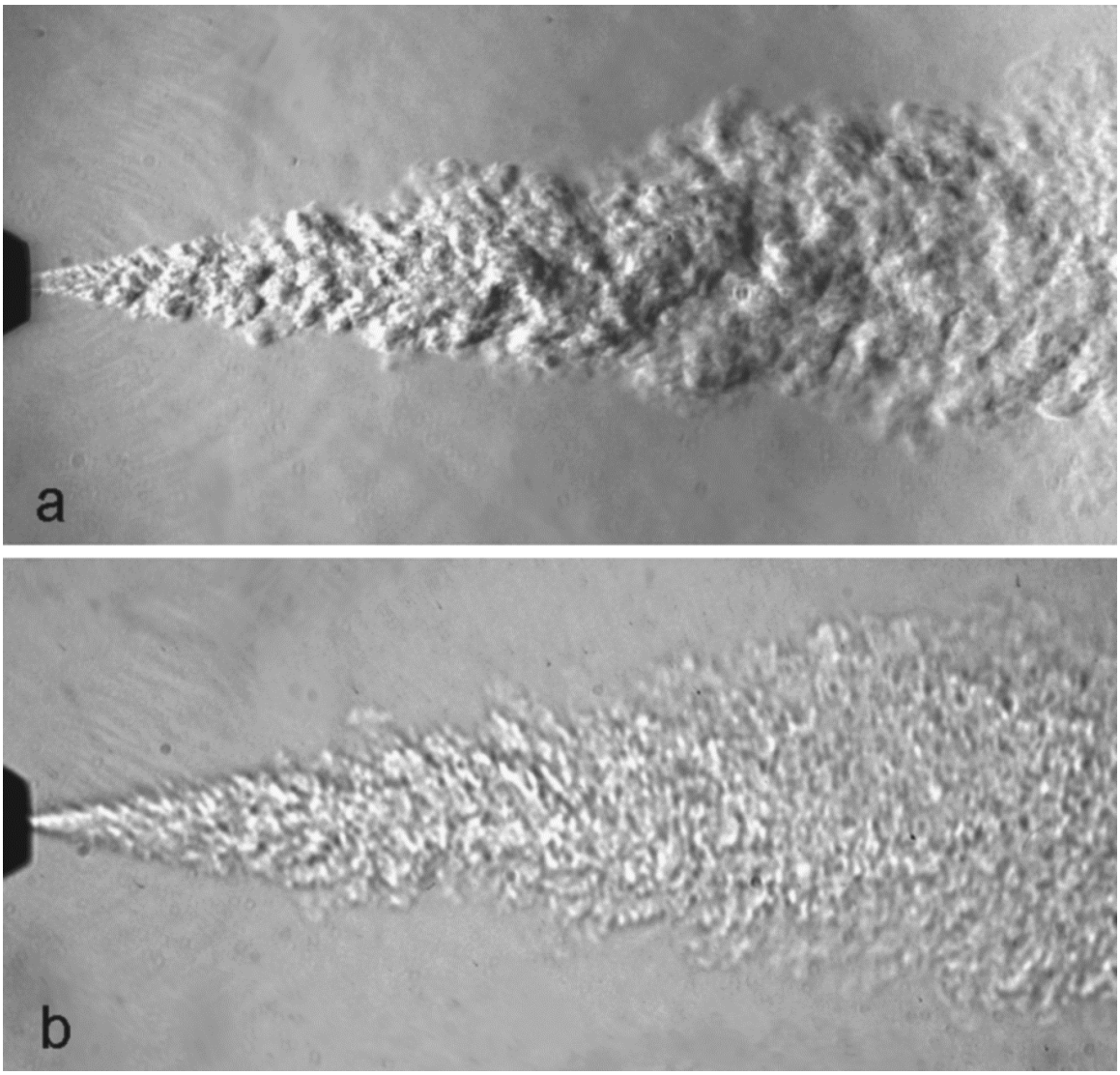

Fig. 1.15. Comparison of Schlieren and shadowgraph images (a) Schlieren image of turbulent helium jet (b) shadowgraph image of the same jet [43]

1.4 Scope of the Present Research

The objective of the current research is to comprehend the effect of the diaphragm rupture pressure, the equivalence ratio, and the amount of hydrogen in the methane/air mixture on the characteristics of ignition and combustion of the methane-hydrogen-air mixture. This research is continued from experimental procedures, and results established by Pereras [17] work on stationary hot-jet ignition experiments, and Chinnathambis [44] work on traversing hot-jet ignition experiments. In order to control the diaphragm rupture pressure, the number of indentations on the diaphragm varies from two to six times. Both chambers are stationary, and the main chamber fuel/air mixture is maintained at atmospheric pressure and room temperature throughout the study. The hydrogen volume fraction in the fuel mixture is decided as 50%, and 70% to compare with Nazmuzzamans [45] numerical results. A new methodology of measuring the ignition delay time using two pressure transducers is established, and validated by comparing with the high-speed video images. With this method measuring ignition delay time, effects of the equivalence ratio, the hydrogen content in a gas mixture, and the rupture pressure on the ignition delay time are examined. Reflected shock pressure is investigated based on the data of measured primary shock speeds, and the reasons of pressure attenuation of the reflected shock are discussed. An image processing code is developed to extract the flame front images from high-speed Schlieren images, and those images are used to obtain the data of flame propagation speed, and flame oscillation frequency. Lastly, a feedback mechanism between the shock and the flame is discussed to figure out what makes the fast combustion condition. These results may be useful to design hot-reactive jet ignition type constant-volume combustors.

2. EXPERIMENTAL SETUP AND PROCEDURE

The previous version of a wave-rotor constant volume ignition and combustion rig was designed by Bilgin [26] at the University of Washington, and the rig was improved by Perera [17], Chinnathambi [44], and Murphy [46] at the Combustion and Propulsion Research Laboratory (CPRL) at Purdue University Indianapolis. The single-channel rig consists of the pre-chamber, and the main chamber as illustrated in Figure 2.1. The pre-chamber is mounted on a shaft to be rotated by an electrical motor via a belt-drive for simulating a relative motion between a traversing hot-jet injection source and a channel in the wave-rotor drum. In the current work, the pre-chamber and thus the injected jet is stationary for all cases conducted in the current study, as the focus is on the fuel mixtures and optical techniques. In future studies, traversing jet ignition studies using a rotating pre-chamber may be accomplished. This may require better control of leakage between two chambers when rotating the pre-chamber.

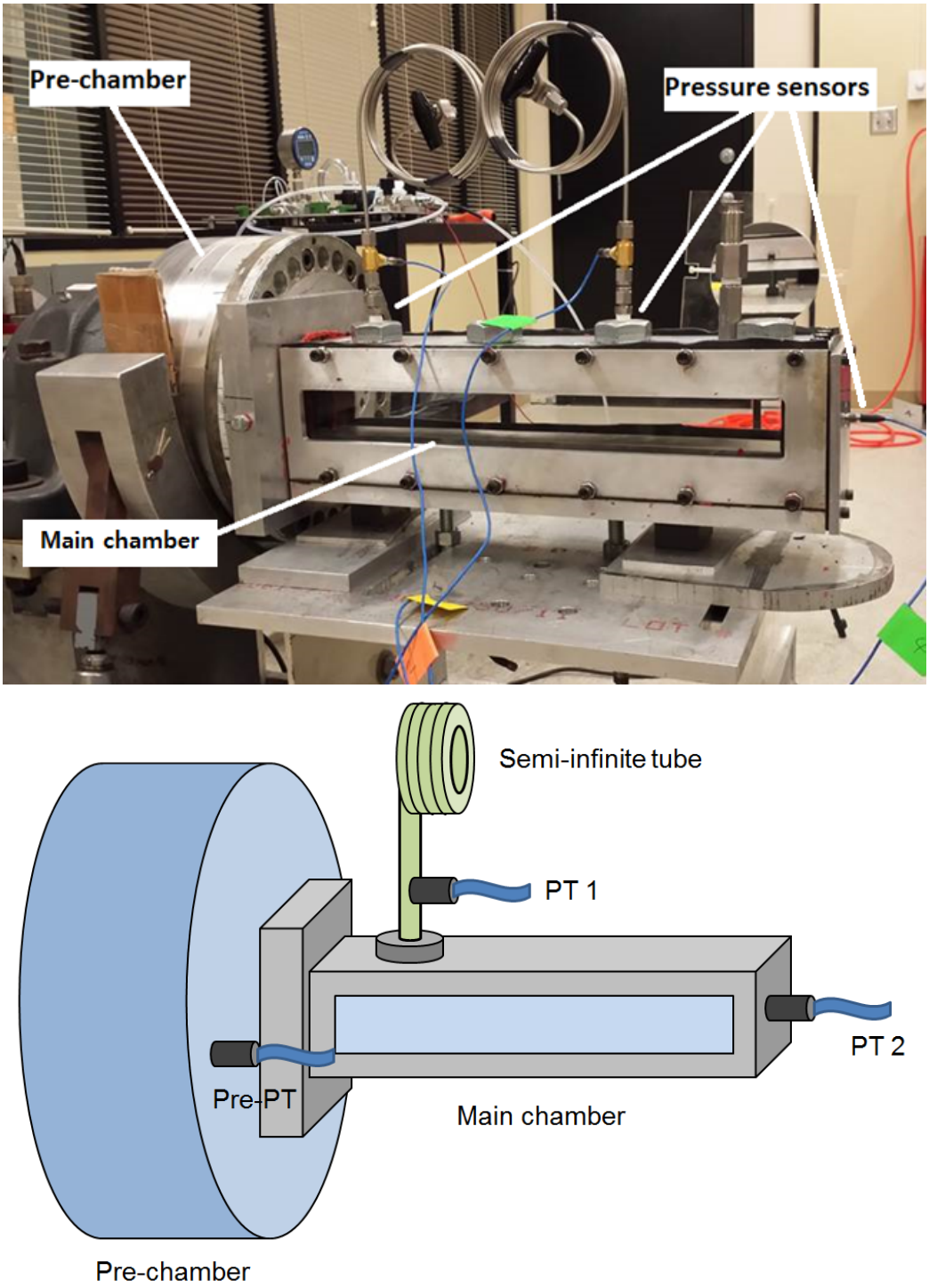

Fig. 2.1. Combustion chambers in the wave-rotor constant volume ignition and combustion rig

2.1 Pre-Chamber

The cylindrical pre-chamber produces hot combustion products by igniting a primary air-fuel mixture using a spark plug. Then the hot combustion products containing radicals are injected into the main chamber through a converging nozzle. The pre-chamber consists of three parts, a front plate, a middle ring, and a rear plate, made of stainless steel; the internal diameter, width, and volume are 6.519 inches, 1.536 inches, and 51.27 cubic inches, respectively. This nominal volume does not account for the space occupied by the heads of bolts that secure the pre-chamber to the rear plate backing. Further details, including drawings, on the dimension of the pre-chamber are discussed in [17], and [44]. Two fueling ports are located on the rear plate, and two identical cylindrical stepped cut-outs on the front plate shown in Figure 2.2, ensuring static and dynamic balance of the pre-chamber for stationary and rotary test conditions. One hole is used for the nozzle insert assembly, and another hole is used to mount a sealing cover without any hole, or a pressure transducer insert only for the stationary test.

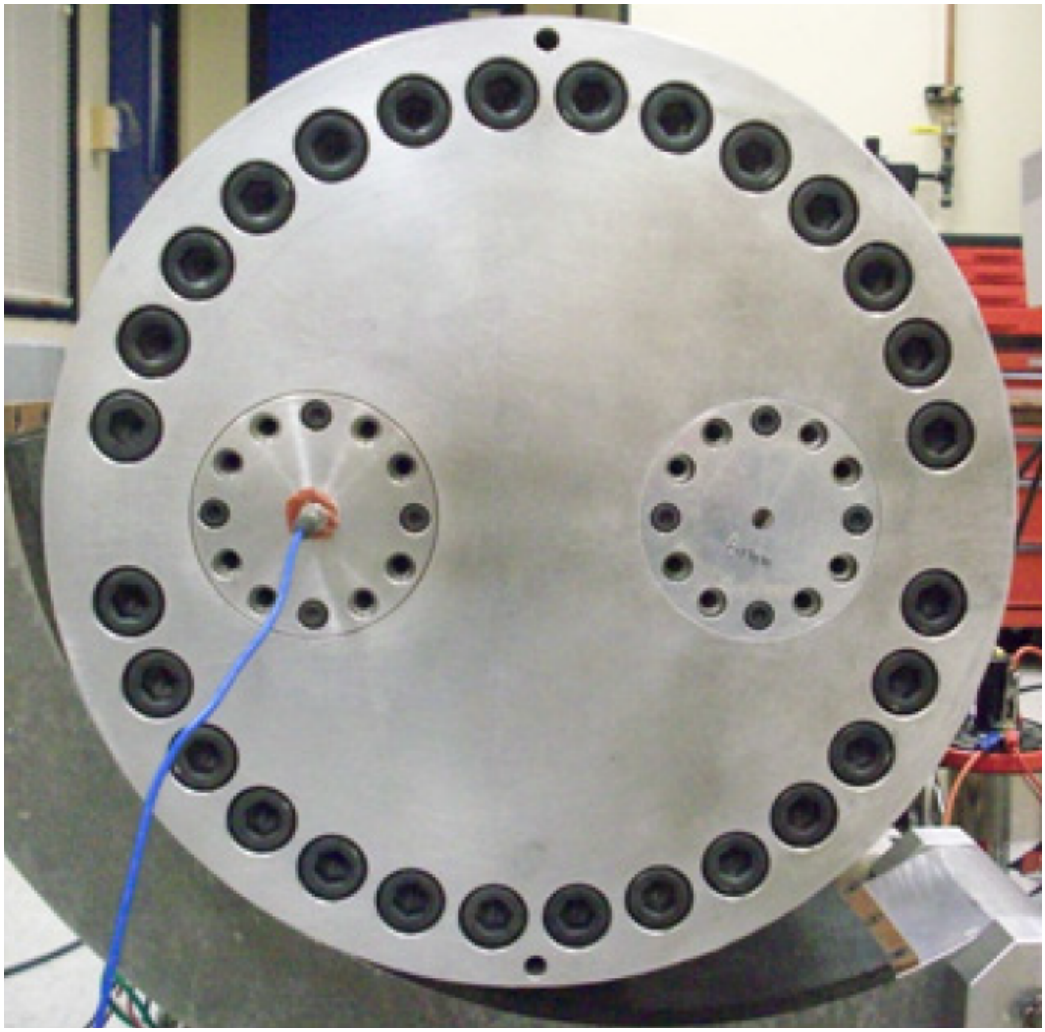

Fig. 2.2. Front plate of the pre-chamber with nozzle insert on the right, and pressure transducer insert on the left

2.1.1 Spark Plug

A spark plug, Champion model RC11ZYC4, with a single side electrode and 1 mm spark gap is installed at the center of the rear plate inside the pre-chamber. The electric current to the spark plug is synchronized with the high speed camera and the pressure transducer data acquisition system. Thus, when the current of electrons surges across the gap, it triggers recordings of the high speed camera, and the pressure signals simultaneously.

2.1.2 Nozzle

Different nozzle inserts with varying cross-sectional areas and geometries had been tested by Perera [17], and Bilgin [26]. A nozzle insert with exit diameter of 0.2362 inches (6 mm), as shown in Figure 2.3, has been selected for the current research because it showed the minimum ignition delay time among tested nozzle inserts [17].

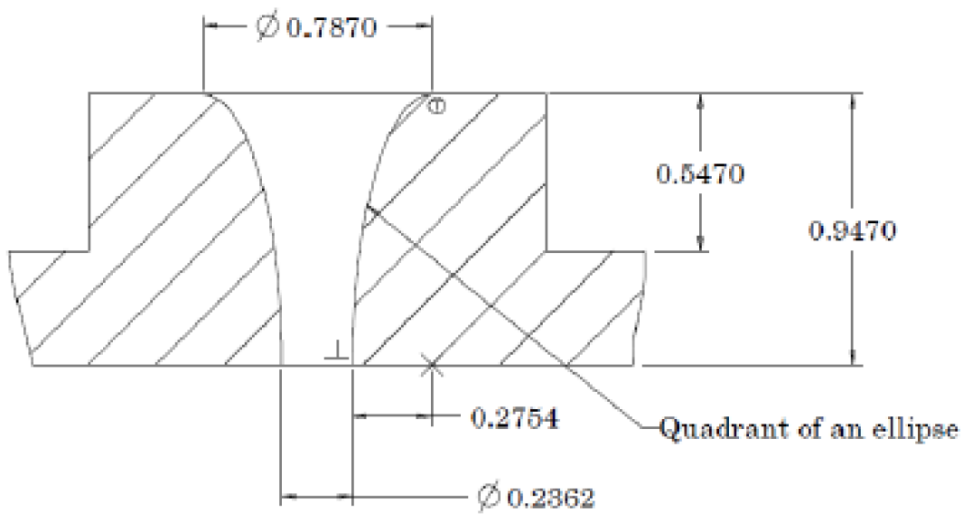

Fig. 2.3. Selected nozzle insert dimensions [17]

2.1.3 Diaphragm

A breakable diaphragm is used to isolate the pre-chamber from the main chamber by blocking the nozzle until it bursts due to combustion-developed pressure. This achieves an independent air-fuel condition when filling the pre-chamber. As Figure 2.4 shows, the nozzle insert assembly consists of three parts, a nozzle insert, a diaphragm, and a nozzle plate. The diaphragm is installed between the nozzle insert and the plate. After assembling the nozzle insert, it is fixed into the pre-chamber nozzle cavity. Perera [17] tested several diaphragms with different thicknesses and materials, and concluded that Aluminum alloy 1100 as the diaphragm material with a thickness of 0.003±0.0003 inches is suitable for the current setup whereas thicker diaphragms, 0.004 inches and 0.005 inches, were not ruptured under the desired pre-chamber combustion condition. In addition, Mylar® polyester (PET) film tried as a diaphragm was melted by the combustion heat release, and was not ruptured by the pressure rise, causing an extended diaphragm rupture time. Moreover, the melting of the polyester film produces chemical species, which may cause experimental uncertainties that cannot be clarified with the current experimental setup.

The diaphragm is scored using the ScoreOne 50050 glass cutter to promote rupturing of diaphragm into four symmetric petals as illustrated in Figure 2.5. If the rupture pattern is like 2 petals, or 3 petals after the test, the result from the test is abandoned since these asymmetrical rupture patterns cause variations in the flow field and properties of the hot-reactive jet affecting the ignition in the main chamber. However, even with apparently symmetric rupture observed post-test, it is difficult to quantify the diaphragm rupture process. Figure 2.6 is obtained by setting the high speed camera in front of the nozzle to take images of the diaphragm rupture moment, showing that most of diaphragms rupture in a cross form like Figure 2.6 (a), but 5% of cases rupture in sequence like Figure 2.6 (b). It seems that the diaphragm ruptures into 2 or 3 petals first, and then the flow passing the nozzle tears the untorn part. Although both cases show the four-petal shapes after tests, the untorn part of

the delayed rupture case may cause pressure drop, decreasing the flow rate through the nozzle, and hence the ignition delay time increases. Shallower indentation of the diaphragm tends to cause delayed rupture case. Therefore, a diaphragm should be scored with the enough indentation depth for better repeatability.

Perera [17] also discussed an issue of the diaphragm debris because of which some visible particles were detected by the high speed camera, and those particles were prompting the ignition in the main chamber. The author considered these particles the diaphragm debris, so he excluded the test cases with the visible particles in the high speed images. However, it is found that particles are present with and without the diaphragm as shown in Figure 2.7. Since the pre-chamber experiences fuel-rich premixed combustion, the critical C/O ratio for soot formation is satisfied, and therefore, soot nuclei formed by chemical reactions may become large enough to survive the re-burning process. The particles continue to grow, and begin to coagulate to form chain agglomerates [47]. When particles pass through the cold nozzle surface, they may agglomerate due to sudden heat loss to the nozzle surface, creating visible illuminating particles. To conclude, this phenomenon may be a natural consequence of the fuel-rich premixed combustion, and the case including this phenomenon should not be excluded.

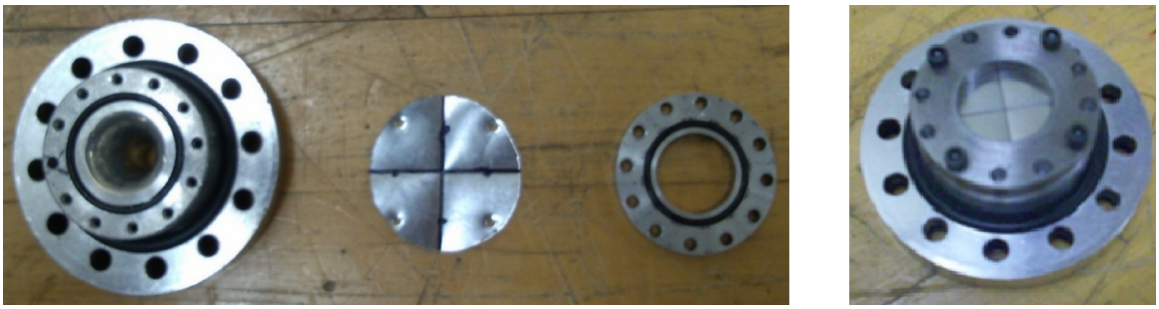

Fig. 2.4. Nozzle insert, scored diaphragm, nozzle plate, and nozzle insert assembly (from left)

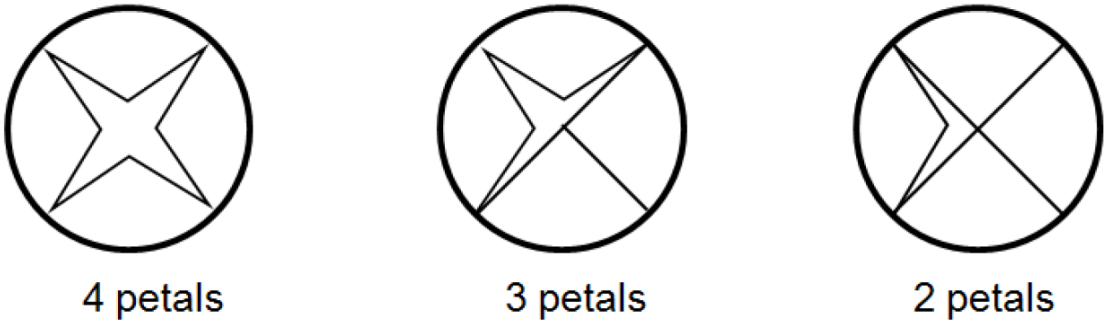

Fig. 2.5. Diaphragm rupture patterns [17]

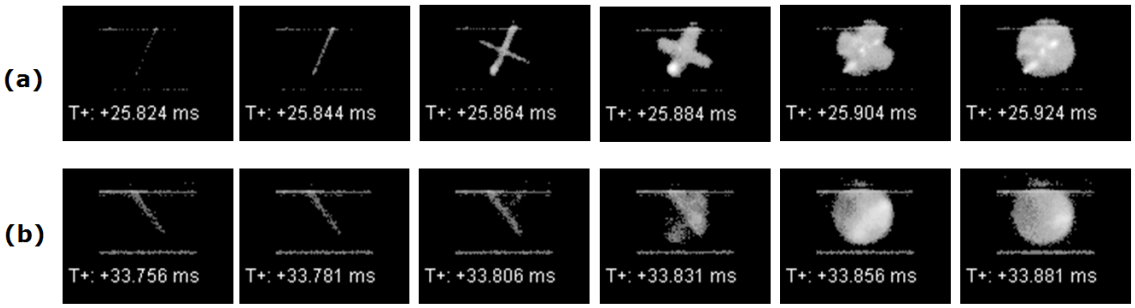

Fig. 2.6. Diaphragm rupture process, Φ=1.1, and Ψ=1 (CH_4:H_2=50:50) (a) rupture with a cross form (b) delayed rupture

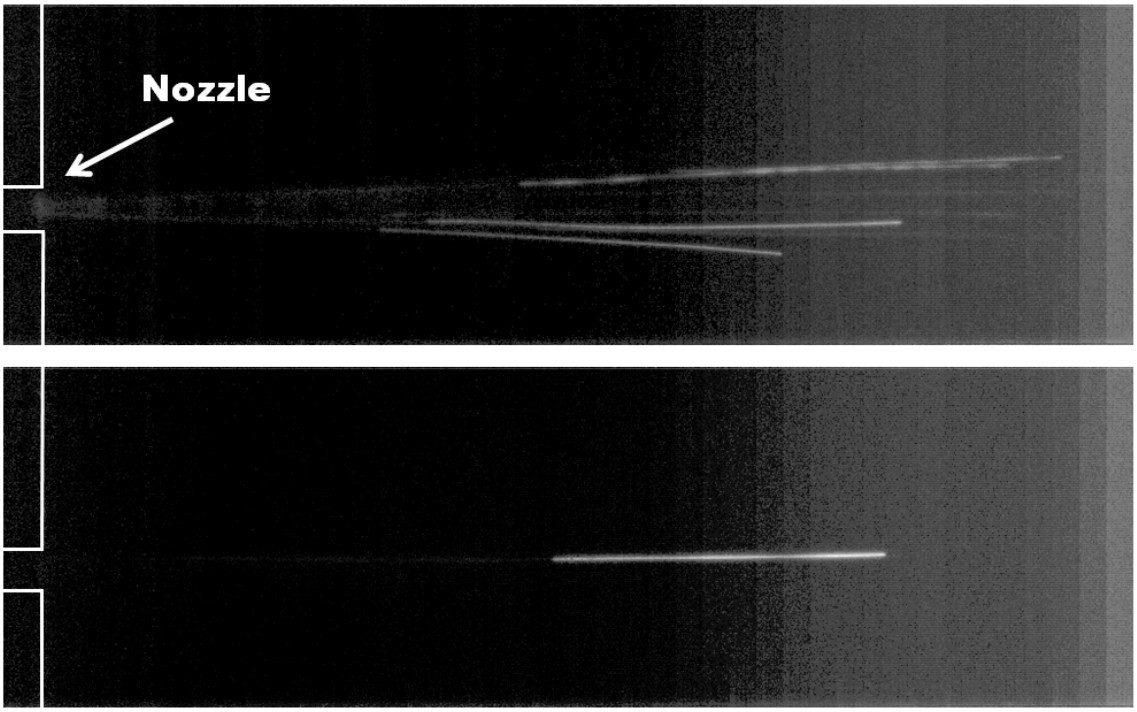

Fig. 2.7. Path lines of the visible particles from the nozzle on the pre-chamber, Φ=1.1, and Ψ=1 (CH_4:H_2=50:50) (a) with a diaphragm (b) without a diaphragm

2.2 Pre-Chamber Ignition System

The pre-chamber ignition system is employed to generate spark ignition in the pre-chamber. Figure 2.8 illustrates the ignition system including connections and components. The main components of the ignition system are the power source, the trigger button, the capacitive discharge ignition (CDI) controller, the ignition coil, and the spark plug. Perera [17] and Chinnathambi [44] used a 12 V battery as a power source, but it was inconvenient to use since the voltage of the battery drops after using it for hours, and cannot produce a spark when the voltage is less than 10 V. Whenever it happens, the battery needs to be recharged. Therefore, the battery was replaced with an AC/DC transformer from 120 VAC to 12 VDC. The trigger button is placed on a remote control box, which is located in an adjacent room to the laboratory room for safety. The remote control box contains several other features to bring all controls required for the experiment, such as control of pre-chamber rotation speed, and a pre-chamber brake. The current study deals only with the stationary pre-chamber condition, so those features are not discussed here. Detailed features of the remote control box are described in Chinnathambi [44]. An MSD 6AL unit is used as the CDI controller, which can make extremely quick compensations to the output voltage, multiple spark series, timing and rpm limits while maintaining precise timing and accurate rotation speed. A capacitor inside the CDI controller is quickly charged with 520 - 535 V and stores the voltage until the ignition is triggered. The voltage sent to the ignition coil positive terminal is always at full power even at high rpm, so the MSD controller produces full power multiple sparks for each firing of a plug. The ignition coil, MSD Blaster 2, increases the voltage from the ignition controller up to 45,000 V to create an electric spark in the spark plug. The high-tension cable from the ignition coil is connected to a copper rod that is installed in an axial hole along the pre-chamber shaft. An acrylic tube provided by Plexiglass is used to insulate the copper rod, avoiding sparking between the copper rod and the steel drive shaft. The spark plug, RC11ZYC4, is installed at the end of the copper rod.

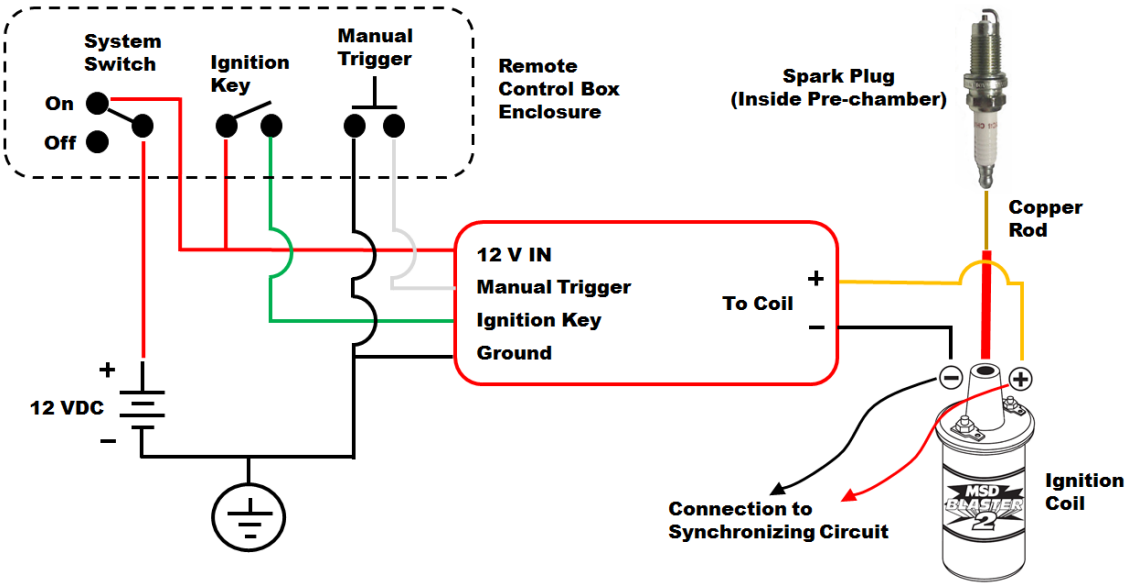

Fig. 2.8. Schematic diagram of the pre-chamber ignition system

2.3 Main Chamber

The main chamber, in Figure 2.1, is a cuboid assembly made of aluminum alloy 6061. The chamber has a long channel with a square cross-section of 1.57 x 1.57 inches, and the length is 16 inches. Two sides of the channel are composed of optical access windows allowing light pass through the channel for the Schlieren photography. The two windows are made of quartz, provided by Quality Quartz Engineering, with a thickness of 1 inch for enduring the combustion pressure in the main chamber. There are two dynamic pressure transducers, PCB 113B32, installed on the main chamber surface. In previous work, all pressure sensors were flush mounted on the top wall, but this setup caused premature failure of all sensors due to heat damage. In the current setup, one transducer is mounted on a pressure probe assembly (described in section 2.6.4), which is located on the top of the chamber, to avoid heat damage from the combustion. The other is flush mounted on the end wall of the chamber since the flame front does not reach to the end wall. A fueling port is located on the top wall at a distance of 14 inches from the main chamber entrance. The locations of pressure transducers and the fueling port are illustrated in Figure 2.9. The main chamber assembly is mounted on a sliding bed, which enables a horizontal movement of the main chamber, providing a sufficient clearance to access the front surface of the pre-chamber. When conducting a test, both chambers are attached tightly using two bolts below the main chamber and a clamping tool behind the main chamber. A sealing ring assembly is located between two chambers, preventing leakage from the main chamber, so that very nearly constant-volume combustion takes place in the main chamber, except for mass exchange with the pre-chamber.

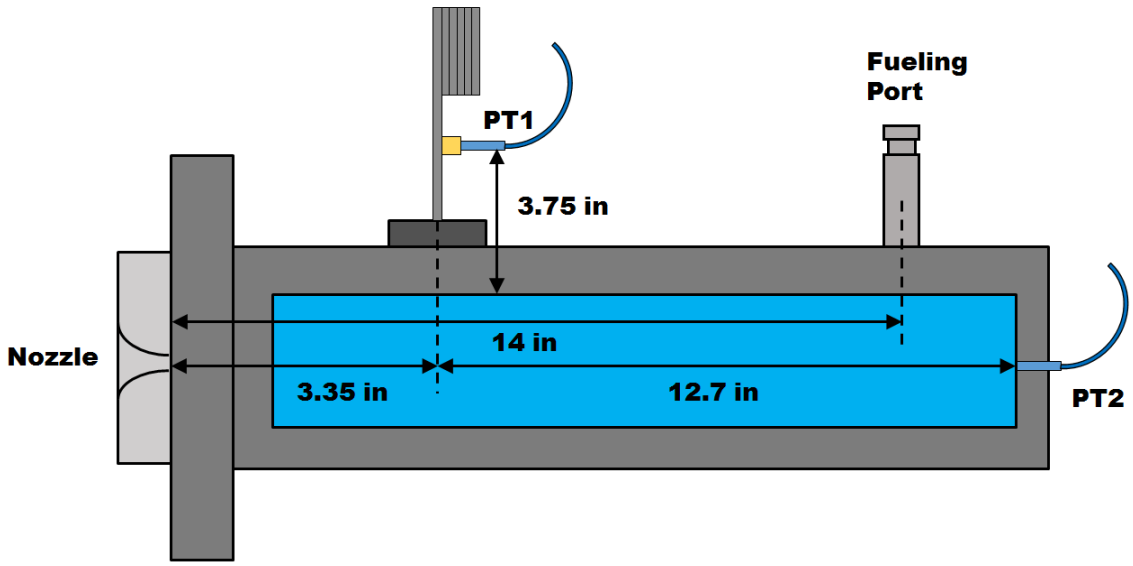

Fig. 2.9. Locations of pressure transducers and a fueling port on the main chamber

2.4 Ignition Process

As shown in Figure 2.10 (a), the hydrogen-methane-air mixture in the pre-chamber is ignited by the spark plug. A pre-mixed flame then propagates spherically with the spark plug at the center, consuming the unburned mixture. Due to a temperature increase by combustion, pressure builds up inside the pre-chamber, and at a certain level of the pressure, a diaphragm is ruptured, so the hot product gas containing radicals is injected into the main chamber through a nozzle as Figure 2.10 (c).

When the diaphragm ruptures, a sudden pressure change across the nozzle generates an initial shock wave. This shock wave is travelling inside the main chamber back and forth, increasing temperature and pressure gradually. In a shock tube experiment, a reflected shock wave ignites a combustible mixture. While shock waves are traversing the chamber, ignition of the hydrogen-methane-air mixture in the main chamber takes place by the hot-jet from the nozzle as illustrated in Figure 2.11 (b). A flame propagates from the ignition point, and later is subject to shock-flame interactions when the initial shock reflects at the end walls and refracts at density interfaces. The resulting multiple waves cause the gas in the chamber to move longitudinally back and forth, causing an apparent flame motion upon which the actual flame propagation is superimposed.

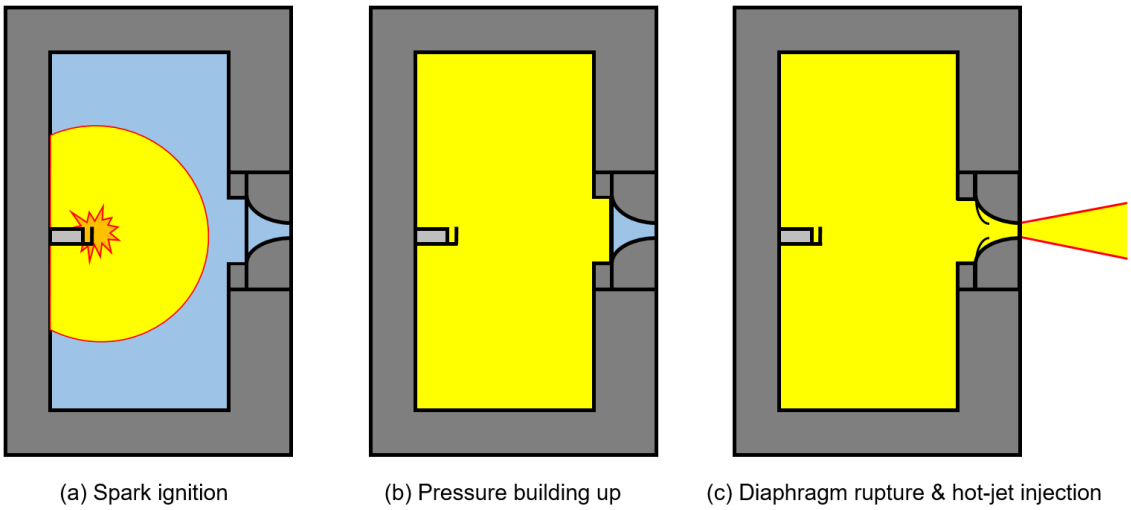

Fig. 2.10. Pre-chamber ignition process

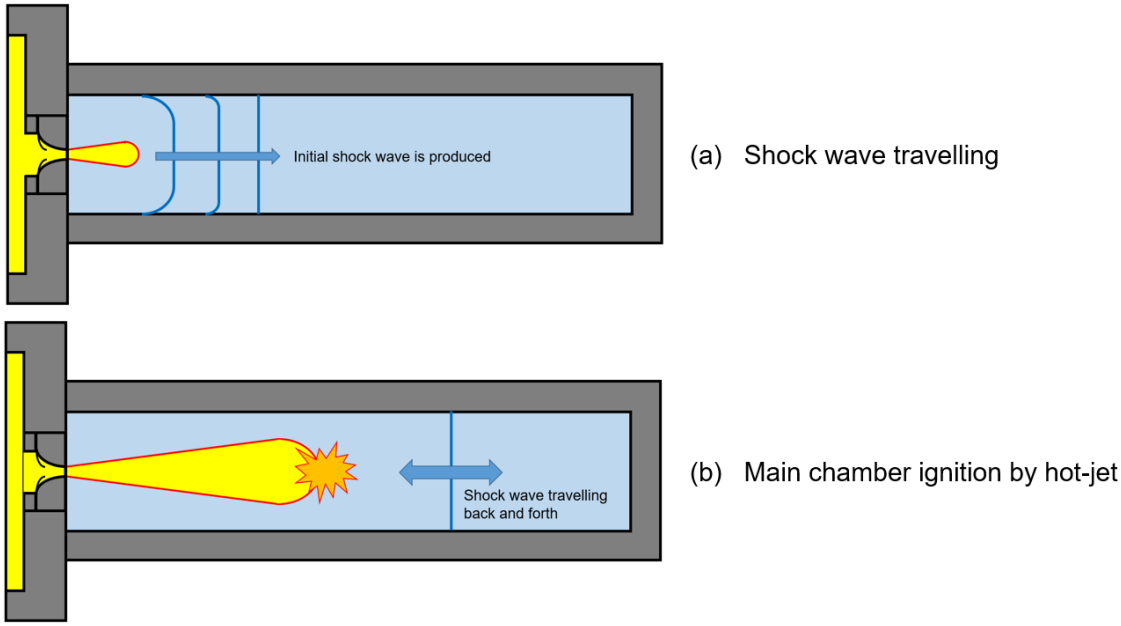

Fig. 2.11. Main chamber ignition process

2.5 Fueling System

Perera [17], and Chinnathambi [44] used the partial pressure method to fuel both chambers. In order to use the partial pressure method, which applied to the previous studies, leakage from the system should not exist during filling, since any leak in the system causes a serious increase of uncertainty on the desired air/fuel ratio. The leakage rate of the pre-chamber is about 0.001 psi/min when a vacuum of about -19 psig is created, and the fueling process of the pre-chamber finishes within 2 min. Thus the partial pressure method described in Perera [17], and Chinnathambi [44] still can apply to the pre-chamber fueling for the current study. However, after the main chamber was dismantled to install a heater inside, the leakage rate of the main chamber was about 0.02 psi/min. Therefore, another method should be adopted to make a desired air/fuel ratio in the main chamber while air leaks in. Therefore, each chamber is fueled by different means in the current study. The details of the current fueling strategy will be discussed in the next sections. Both fuels, methane and hydrogen, are supplied by Praxair, and the specifications are described in Table 2.1.

Table 2.1
Fuel specifications

Gas	Quality
Methane	CH_4 99.97% O_2 < 15 ppm H_2O < 5 ppm N_2 < 100 ppm CO + CO_2 < 10 ppm H_2 < 10 ppm C_nH_m < 100 ppm
Hydrogen	H_2 99.999 % O_2 < 1 ppm H_2O < 3 ppm THC < 0.5 ppm

2.5.1 Pre-Chamber Fueling

Figure 2.12 shows the fueling system of the pre-chamber. First, most of air in the pre-chamber is removed using a vacuum pump until the pressure gauge indicates around -10 psi. Second, hydrogen is supplied slowly and precisely using a choke valve until the pressure inside the chamber reaches the desired value on the pressure table. Third, methane is supplied in the same way. After supplying both fuels, the pressure gauge still shows a negative value. Lastly, opening the ambient air valve, deficient pressure is filled by ambient air until the gauge pressure reaches 0 psi, achieving the desired equivalence ratio, and ambient pressure condition in the pre-chamber .

Daltons partial pressure law states that the total pressure of a mixture of gases is equal to the sum of the partial pressure of the individual gases if gases are occupying the same volume.

$$P = \Sigma P_i = \Sigma \chi_i P \tag{2.1}$$

Assuming that all components of the gas mixture occupy the same volume, P is total pressure of the gas mixture, P_i is the partial pressure of the ith component in the mixture, and χ_i is the mixture concentration in mole fractions. The desired equivalence ratio is determined as follows,

$$\Phi = \frac{(A/F)_{\mathrm{stoic}}}{(A/F)_{\mathrm{actual}}} \tag{2.2}$$

where (A/F) is the actual air/fuel mass ratio, and $(\mathrm{A/F})_{\mathrm{stoic}}$ is the stoichiometric air/fuel mass ratio. Air is assumed to be a mixture of one mole of O_2 and 3.76 moles of N_2. For the fuel mixture of hydrocarbon and hydrogen, the stoichiometric chemical reaction equation of the combustion between the fuel and air would be,

$$N_{\mathrm{H_2}} H_2 + N_{\mathrm{CH_4}} + a(O_2 + 3.76 N_2) \rightarrow x CO_2 + y H_2O + a 3.76 N_2 \tag{2.3}$$

where N_i is the number of moles of a component i, x is $\Psi N_{\mathrm{H_2}}$, and y is $N_{\mathrm{H_2}} + 2\Psi N_{\mathrm{H_2}}$.

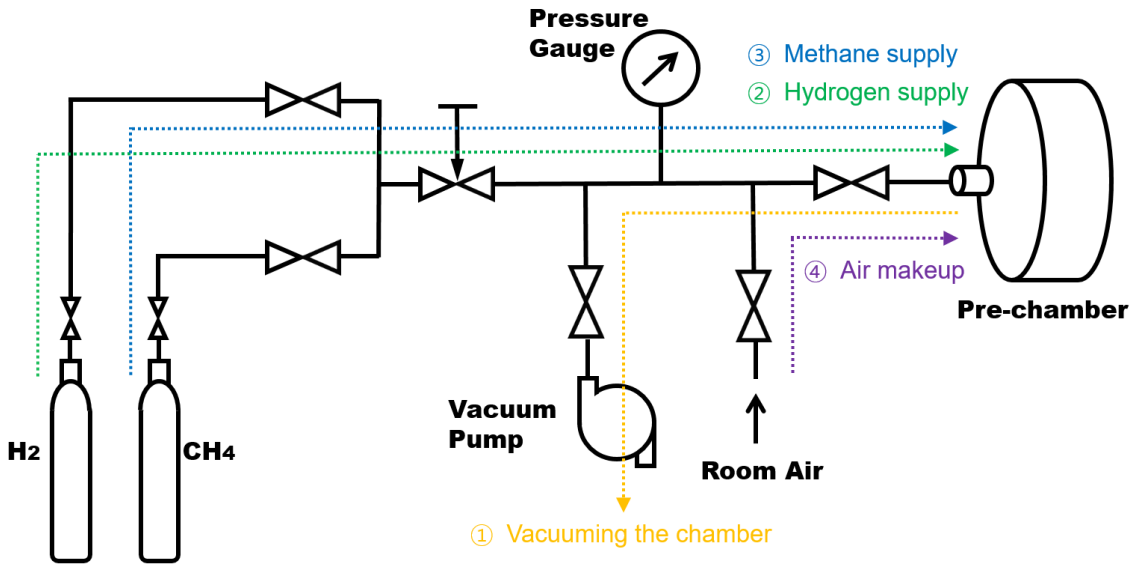

Fig. 2.12. Schematic diagram of the pre-chamber fueling system

Introducing a fuel ratio,

$$\Psi = \frac{N_{\mathrm{CH_4}}}{N_{\mathrm{H_2}}} \tag{2.4}$$

Therefore, the stoichiometric air/fuel ratio is,

$$(A/F)_{\mathrm{stoic}} = \frac{4.76 * a * MW_{\mathrm{air}}}{N_{\mathrm{H_2}} MW_{\mathrm{H_2}} + N_{\mathrm{CH_4}} MW_{\mathrm{CH_4}}} \tag{2.5}$$

From the law of conservation of moles,

$$a = 2N_{\mathrm{CH_4}} = \frac{N_{\mathrm{H_2}}}{2} \tag{2.6}$$

The desired air/fuel ratio can be represented as,

$$(A/F)_{\mathrm{actual}} = \frac{4.76 * b * MW_{\mathrm{air}}}{N_{\mathrm{H_2}} MW_{\mathrm{H_2}} + N_{\mathrm{CH_4}} MW_{\mathrm{CH_4}}} \tag{2.7}$$

Using Eq. (2.2), the unknown b can be obtained as,

$$\Phi = \frac{(A/F)_{\mathrm{stoic}}}{(A/F)_{\mathrm{actual}}} = \frac{2N_{\mathrm{CH_4}} + 0.5N_{\mathrm{H_2}}}{b} \tag{2.8}$$

$$b = \frac{2N_{\mathrm{CH_4}} + 0.5N_{\mathrm{H_2}}}{\Phi} \tag{2.9}$$

Thus, the moles of air in the chamber is,

$$N_{\mathrm{air}} = 4.76 * b = 4.76 * \frac{2N_{\mathrm{CH_4}} + 0.5N_{\mathrm{H_2}}}{\Phi} \tag{2.10}$$

The total moles of the air/fuel mixture can be expressed as,

$$N_{\mathrm{total}} = N_{\mathrm{H_2}} + N_{\mathrm{CH_4}} + N_{\mathrm{air}} = N_{\mathrm{H_2}}(1 + \Psi + 4.76 * \frac{0.5 + 2\Psi}{\Phi}) \tag{2.11}$$

From Eq. (2.1), the partial pressure of each fuel gas is,

$$P_{\mathrm{H_2}} = \frac{N_{\mathrm{H_2}}}{N_{\mathrm{total}}} P = \frac{\Phi}{\Phi(1 + \Psi) + 4.76(0.5 + 2\Psi)} P \tag{2.12}$$

$$P_{\mathrm{CH_4}} = \frac{\Psi N_{\mathrm{H_2}}}{N_{\mathrm{total}}} P = \frac{\Psi\Phi}{\Phi(1+\Psi) + 4.76(0.5+2\Psi)} P \tag{2.13}$$

Therefore, if the pre-chamber pressure is $\mathrm{P_{residual}}$ after vacuuming the pre-chamber and the final pressure of the pre-chamber is P, a pressure table for achieving the desired equivalence ratio can be prepared using the following equation.

$$P = P_{\mathrm{residual}} + \frac{\Phi}{\Phi(1+\Psi) + 4.76(0.5+2\Psi)} P + \frac{\Psi\Phi}{\Phi(1+\Psi) + 4.76(0.5+2\Psi)} P + P_{\mathrm{makeup}} \tag{2.14}$$

where $\mathrm{P_{makeup}}$ is the pressure rise when the pre-chamber is brought up to ambient pressure by makeup ambient air after fueling both gases. Since the desired pre-chamber initial condition is fixed as below,

P=ambient pressure

$\Phi = 1.1$

$\Psi = 1$

Eq. (2.14) can be expressed as,

$$P_{\mathrm{ambient}} = P_{\mathrm{residual}} + \frac{1.1}{2*1.1 + 4.76*2.5} P_{\mathrm{ambient}} + \frac{1.1}{2*1.1 + 4.76*2.5} P_{\mathrm{ambient}} + P_{\mathrm{makeup}} \tag{2.15}$$

2.5.2 Main Chamber Fueling

Due to the leakage into the main chamber, the partial pressure cannot be applied. Therefore, the desired mass amount of each gas should be precisely calculated and supplied into the main chamber. Before discussing calculations of gas masses required for fueling of the main chamber, the fueling process should be introduced first to help understand the calculations.

Figure 2.13 is the schematic diagram of the main chamber fueling system, and Figure 2.14 demonstrates the fueling procedure for the main chamber. At stage 1, an external chamber and the main chamber hold only air at ambient pressure. At

stage 2, hydrogen is supplied into the external chamber, increasing pressure of the external chamber to P_{ex1}. At stage 3, methane is supplied into the external chamber, increasing pressure of the external chamber to P_{ex2}. At stage 4, the external chamber holds a mixture of air, hydrogen, and methane at pressure P_{ex2}, and most of air in the main chamber is vacuumed using the vacuum pump until the pressure gauge indicates around -10 psi. At stage 5, the gas mixture in the external chamber is precisely supplied into the main chamber using pressure information and a choke valve. During this filling, room air leaks into the main chamber; hence, the gauge pressure in the main chamber cannot measure the amount of gas mixture transferred. Instead, gauge pressure in the external chamber is used to meter the transferred mass. Note that this fueling process is isothermal in that the gas mixture in the external chamber is slowly discharged to the main chamber so that heat can be transferred through the external chamber wall, maintaining the temperature of the external chamber as ambient temperature. After supplying the mixture, pressure of the external chamber drops to P_{ex3}, and the main chamber is holding the desired amount of hydrogen and methane with some air at negative pressure $-P_2$. At stage 6, the deficient pressure of the main chamber is filled with room air, achieving the desired equivalence ratio and fuel ratio of the air-fuel mixture in the main chamber at ambient pressure.

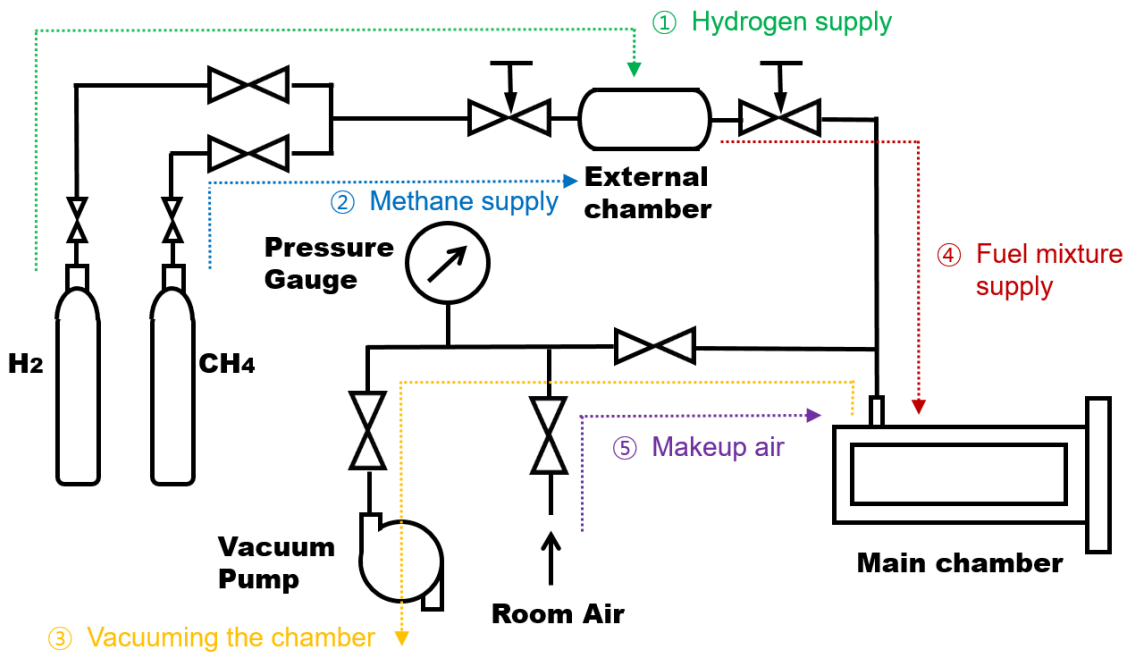

Fig. 2.13. Schematic diagram of the main chamber fueling system

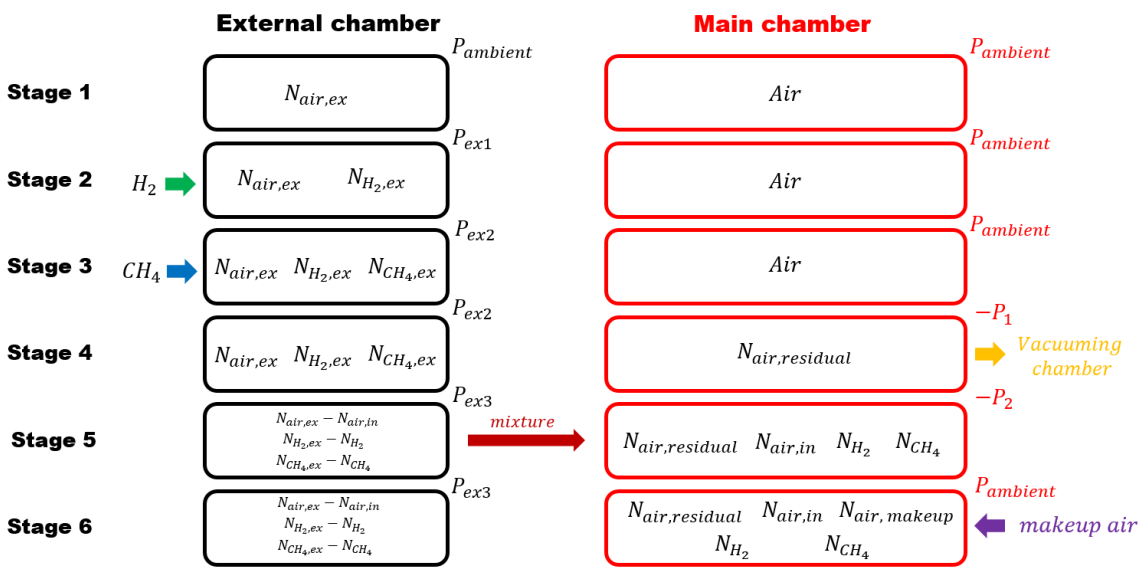

Fig. 2.14. Main chamber fueling procedure

The total mole number of the gas mixture in the main chamber is defined as Eq. (2.11), and it can be modified as an explicit form of $N_{\mathrm{H_2}}$.

$$N_{\mathrm{total}} = N_{\mathrm{H_2}} + N_{\mathrm{CH_4}} + N_{\mathrm{air}} = N_{\mathrm{H_2}}(1 + \Psi + 4.76 * \frac{0.5 + 2\Psi}{\Phi}) = \frac{PV_m}{\bar{R}T} \tag{2.11}$$

$$N_{\mathrm{H_2}} = \frac{P_{\mathrm{ambient}} V_m}{\bar{R}T_{\mathrm{ambient}}} * (1 + \Psi + 4.76 * \frac{0.5 + 2\Psi}{\Phi})^{-1} \tag{2.16}$$

$\mathrm{V_m}$ is the volume of the main chamber, $\mathrm{P_{ambient}}$ and $\mathrm{T_{ambient}}$ are ambient pressure and temperature, respectively, and $\bar{R}$ is the universal gas constant. Therefore, if the fuel ratio Ψ and the equivalence ratio Φ are decided, the required moles of hydrogen and methane can be calculated from Eq. (2.4), and Eq. (2.16).

The moles of air in Eq. (2.11) can be split into three parts as Eq. (2.17).

$$N_{\mathrm{air}} = N_{\mathrm{air,residual}} + N_{\mathrm{air,in}} + N_{\mathrm{air,makeup}} \tag{2.17}$$

$\mathrm{N_{air,residual}}$ is the moles of residual air after vacuuming the main chamber, $\mathrm{N_{air,in}}$ is the moles of air supplied into the main chamber from the external chamber, and $\mathrm{N_{air,makeup}}$ is the moles of air filling the negative pressure after fueling hydrogen and methane into the main chamber.

As described above, two fuels, hydrogen and methane, pressurizes the external chamber, and are mixed with air in it, which can be expressed as below.

$$N_{\mathrm{ex}} = N_{\mathrm{air,ex}} + N_{\mathrm{H_2},ex} + N_{\mathrm{CH_4},ex} \tag{2.18}$$

$\mathrm{N_{ex}}$, $\mathrm{N_{air,ex}}$,$\mathrm{N_{H_2,}}_{ex}$,and $\mathrm{N_{CH_4,}}_{ex}$ represent the moles of the mixture, air, hydrogen, and methane in the external chamber, respectively. Some of this mixture is then supplied into the main chamber. The moles of the mixture supplied from the external chamber, $\mathrm{N_{in}}$, can be expressed as three parts, the moles of air, hydrogen, and methane, which are delivered into the main chamber.

$$N_{\mathrm{in}} = N_{\mathrm{air,in}} + N_{\mathrm{H_2}} + N_{\mathrm{CH_4}} \tag{2.19}$$

These gas components are well illustrated in Figure 2.15. Note that there is a limit of the amount of air supplied into the main chamber, $N_{air,in}$. If $N_{air,makeup}$, the moles of replenishing air, is less than zero, the main chamber is pressurized in that the total amount of air in the chamber, N_{air}, is set to ambient pressure. In other words, some of air in the main chamber should be vented in order to make ambient pressure in the main chamber if air is supplied from the external chamber too much. Therefore, $N_{air,makeup}$ must be higher than zero that can be expressed as Eq. (2.20) by modifying Eq. (2.17).

$$N_{\text{air,makeup}} = N_{\text{air}} - N_{\text{air,residual}} - N_{\text{air,in}} > 0 \tag{2.20}$$

Then, the limit of $N_{air,in}$ can be defined as,

$$N_{\text{air}} - N_{\text{air,residual}} > N_{\text{air,in}} \tag{2.21}$$

Eq. (2.21) can be expressed as Eq. (2.22) using Eq. (2.9) and the ideal gas law.

$$(4.76 \cdot \frac{N_{\text{H}_2}(2\Psi + 0.5)}{\Phi}) - \frac{P_{\text{residual}} V_{\text{m}}}{\bar{R} T_{\text{ambient}}} > N_{\text{air,in}} \tag{2.22}$$

where $P_{residual}$ is the pressure after vacuuming the main chamber.

Since the mole fractions of the mixtures supplied into the main chamber and contained in the external chamber are identical, the following relationship comes into existence:

$$\frac{N_{\text{air,in}}}{N_{\text{H}_2}} = \frac{N_{\text{air,ex}}}{N_{\text{H}_2,ex}} \tag{2.23}$$

Note that left term is the mole fraction of air and hydrogen supplied into the main chamber, and right term is the mole fraction of those in the external chamber. Combining Eq. (2.21), and (2.23) yields:

$$N_{\text{air}} - N_{\text{air,residual}} > \frac{N_{\text{H}_2} N_{\text{air,ex}}}{N_{\text{H}_2,ex}} \tag{2.24}$$

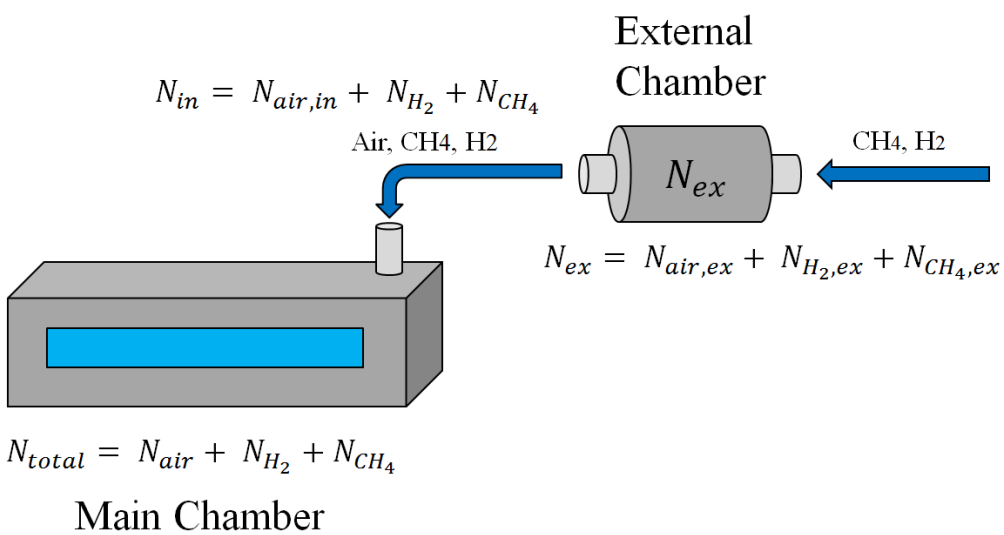

Fig. 2.15. Schematic diagram of gas components in the fueling process

The external chamber goes through three different steps of the pressure change. First, the chamber only holds air at ambient pressure. After fueling hydrogen, the pressure of the external chamber will be P_{ex1}, and then it will be P_{ex2} after fueling methane. Lastly, the external chamber releases some of the mixture into the main chamber, the pressure will drop to P_{ex3}. When the chamber is pressurized, the temperature of the chamber slightly increases. The increased temperature will rapidly drop to ambient temperature by heat transfer, decreasing the pressure of the chamber as well. In order to prevent the additional pressure decrease, the procedure of supplying fuels into the external chamber is carried out slowly enough to maintain temperature, and set the desired pressure precisely.

The mole numbers of hydrogen, methane, and air contained in the external chamber can be decided using the ideal gas assumption.

$$N_{\mathrm{H}_2,ex} = \frac{(P_{\mathrm{ex1}} - P_{\mathrm{ambient}})V_{\mathrm{ex}}}{\bar{R}T_{\mathrm{ambient}}} \tag{2.25}$$

$$N_{\mathrm{CH}_4,ex} = \Psi N_{\mathrm{H}_2,ex} = \frac{(P_{\mathrm{ex2}} - P_{\mathrm{ex1}})V_{ex}}{\bar{R}T_{ambient}} = \Psi\frac{(P_{\mathrm{ex1}} - P_{ambient})V_{ex}}{\bar{R}T_{ambient}} \tag{2.26}$$

$$N_{air,ex} = \frac{P_{ambient}V_{ex}}{\bar{R}T_{ambient}} \tag{2.27}$$

where V_{ex} is the external chamber volume. P_{ex2} can be expressed as a function of P_{ex1} from Eq. (2.26).

$$P_{ex2} = P_{ex1} + \Psi(P_{ex1} - P_{ambient}) \tag{2.28}$$

And the minimum of P_{ex1} is determined by Eq. (2.24) and (2.25)

$$P_{ex1} > P_{ambient} + \frac{N_{\mathrm{H}_2}N_{air,ex}\bar{R}T_{ambient}}{(N_{air} - N_{air,residual})V_{ex}} \tag{2.29}$$

If P_{ex1} does not satisfy the minimum value of Eq. (2.29), the mole fractions of hydrogen and methane are too small so that air in the external chamber will be too much, and Eq. (2.21) will not be satisfied.

Using Eq. (2.10), (2.19), (2.23), and the ideal gas law, N_{in} can be expressed as:

$$N_{in} = N_{air,in} + N_{\mathrm{H_2}} + N_{\mathrm{CH_4}} = \frac{N_{\mathrm{H_2}} N_{air,ex}}{N_{\mathrm{H_2},ex}} + N_{\mathrm{H_2}}(1+\Psi) = \frac{(P_{ex2} - P_{ex1})V_{ex}}{\bar{R}T_{ambient}} \quad (2.30)$$

P_{ex3} is obtained from Eq. (2.30)

$$P_{ex3} = P_{ex2} - \frac{\bar{R}T_{ambient}}{V_{ex}}(N_{\mathrm{H_2}}(1+\Psi) + \frac{N_{\mathrm{H_2}} N_{air,ex}}{N_{\mathrm{H_2},ex}}) \quad (2.31)$$

To summarize, $P_{ambient}$, $T_{ambient}$, $\bar{R}$ and V_{ex} are decided, and $N_{air,residual}$ is obtained from measured pressure after vacuuming the main chamber, so P_{ex1} can be calculated from Eq. (2.9), (2.16), (2.27), and (2.29). P_{ex2} can be calculated using P_{ex1}, and Eq. (2.28). P_{ex3} is obtained from Eq. (2.16), (2.25), (2.27), and (2.31). Using these pressure values, a pressure table can be prepared for supplying the exact amount of methane, and hydrogen into the external chamber, and the main chamber to achieve the desired fuel ratio, and the equivalence ratio. Since all calculations are very sensitive to two volumes, V_{ex} and V_m, All volumes of not only two chambers, but also tubing parts related to each volume are precisely measured, and applied in the calculations. Ambient temperature in all calculations is fixed as 298.15 K since the temperature in the laboratory is regulated by a central control system in the building. Ambient pressure varies hour by hour, so the actual atmospheric pressure at the time of the experiment is used as the ambient pressure for all calculations. The local atmospheric pressures of the test days are organized in Table 2.2. The average value of the local pressure is applied as the ambient pressure in calculations, and abbreviations FL and Sch in the column of corresponding test cases represent tests of flame luminosity image and schlieren image, respectively.

Table 2.2
The local atmospheric pressures of the test days [48]

Experiment Date and Time	Local Pressure (hPa)	Mean Pressure (psi)	Corresponding Test Cases
Oct-22-2015 pm 4 ~ 9	1021.5 ~ 1022.9	14.825809	FR) Φ : 1 , Ψ : 1 #1~2 (6 cases)
Oct-29-2015 pm 2 ~ 4	1010.0 ~ 1010.6	14.653214	FR) Φ : 1 , Ψ : 1 #3 (3 cases)
Oct-31-2015 am 10 ~ pm 3	1016.0 ~ 1009.8	14.690924	FR) Φ : 1 , Ψ : 3/7 #1~3 (9 cases)
Nov-2-2015 am 9 ~ pm 6	1017.4 ~ 1016.5	14.750389	FR) Φ : 0.8 all (18 cases)
Nov-3-2015 pm 2 ~ pm 10	1020.0 ~ 1020.8	14.799702	FR) Φ : 0.6 all / Φ : 0.4 , Ψ : 1 #1 (21 cases)
Nov-4-2015 pm 1 ~ 8	1020.8 ~ 1019.8	14.798252	FR) Φ : 0.4 , Ψ : 1 #2~3, Ψ : 3/7 #1~3 (15 cases)
Dec-31-2015 pm 12 ~ 4	1027.6 ~ 1026.4	14.895428	Sch) Φ : 1 , Ψ : 1 / Φ : 0.8 , Ψ : 1 (4 cases)
Jan-5-2016 pm 3 ~ 5	1033.2 ~ 1032.2	14.978099	Sch) Φ : 0.6 , Ψ : 1 / Φ : 0.4 , Ψ : 1 (4 cases)
Jan-6-2016 pm 3 ~ 7	1025.9 ~ 1025.3	14.875122	Sch) Φ : 1~0.4 , Ψ : 3/7 (8 cases)

2.6 Data Acquisition

In order to access combustion events of millisecond-timescales, the fast-response pressure data acquisition system, and the high-speed image acquisition system are employed. Figure 2.16 illustrates the data acquisition system for both pressure and image recording. In order to synchronize the data acquisition with the spark ignition in the pre-chamber, the voltage from the ignition coil is used as the trigger signal.

2.6.1 Synchronizing Circuit

The synchronizing circuit, an electric circuit triggering both pressure and image data acquisitions simultaneously, is prepared. When the ignition coil voltage with +24 V, pulsed square waves is applied on the synchronizing circuit, the voltage drops to +10 V through resistors at a Zener diode, NTE5156A, and is applied to a n-channel silicon junction Field Effect Transistor (JFET), NTE 312, as shown in Figure 2.17. The JFET, which is composed of three terminals, a gate, a drain, and a source, acts as a switch. When the +10 V voltage is not applied to the gate, the source (camera +5 V trigger, and DAQ trigger) and the drain (grounds) are not connected. When the voltage is applied, the source and the drain are connected, allowing the connection between the camera trigger signal and the camera ground, and voltage at the pressure DAQ to rise towards +5 V. The Zener diode is employed to protect the JFET from the voltage overshooting. The high-speed camera starts to record images when the +5 V trigger pin is connected to the camera ground pin, and the pressure DAQ starts to record pressure data when more than 4 V is applied to the DAQ trigger box, SCXI 1302. When the pulsed signal from the ignition coil arrives at the NTE 312, the source and the drain terminals are connected, so the +5 V trigger signal from the high-speed camera goes into the pressure DAQ trigger box and the camera ground, triggering both systems at the same time. Both systems are set to be triggered by the rising edge signal of +5 V.

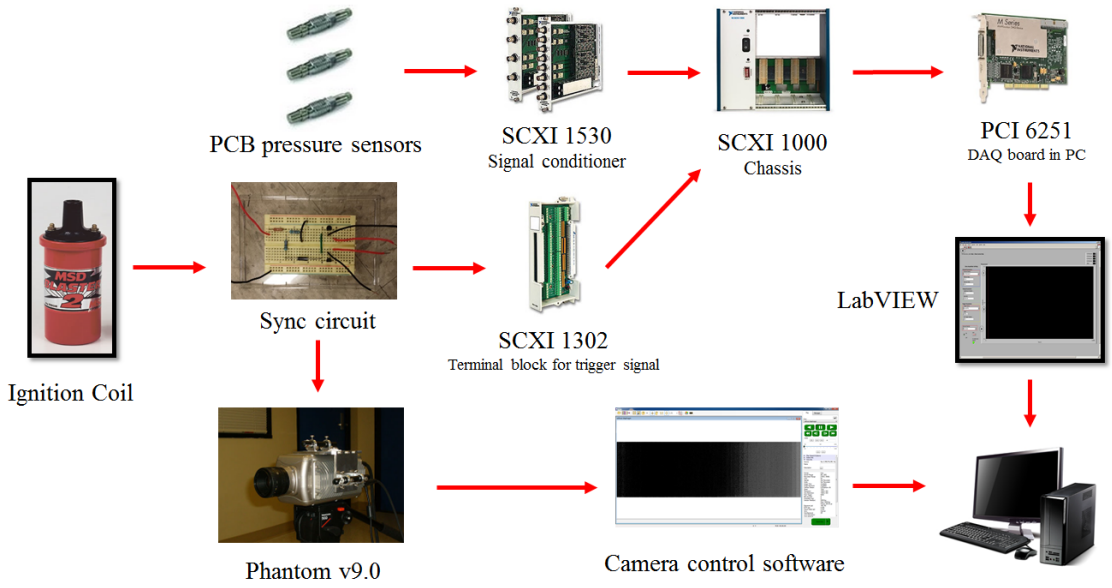

Fig. 2.16. Schematic diagram of data acquisition system

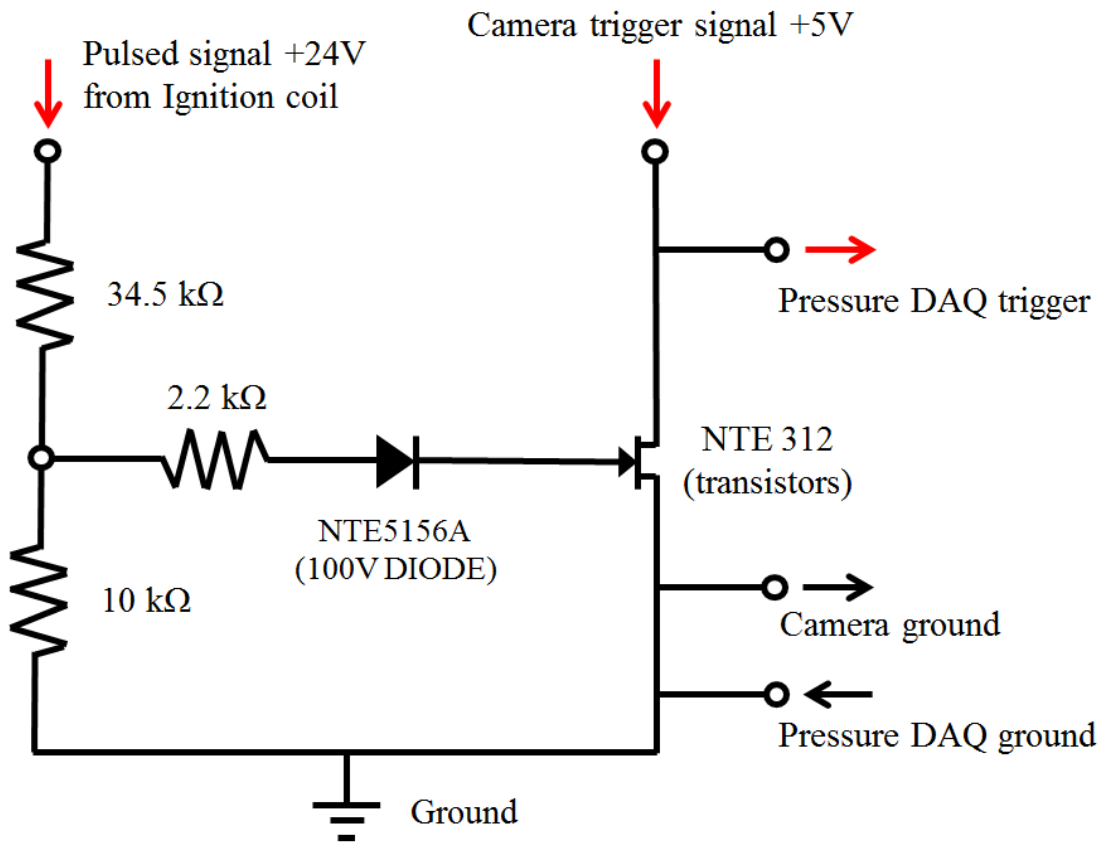

Fig. 2.17. Synchronizing circuit diagram

2.6.2 Pressure Data Acquisition System

The DAQ trigger box, SCXI 1302, and the signal conditioner, SCXI 1530, are put together in the chassis, SCXI 1000. SCXI 1302 receives the trigger signal from the synchronizing circuit, and SCXI 1530 supplies the excitation voltage of 24 V to pressure sensors, amplifies the signal, and reduces noise of the signal. The M-series data acquisition device, PCI 6251, which is assembled in a computer, connects the SCXI 1000 with the computer. National Instruments LabVIEW 2013 was used to develop a virtual instrument (VI) that controls the hardware in the pressure data acquisition system. The main functions of the VI are to identify the trigger event and start recording the pressure data as a tab delimited test file. The number of input channels, sampling rate, and the number of samples can be controlled using the front panel of the VI.

2.6.3 Dynamic Pressure Transducer

As illustrated in Figure 2.1, three dynamic pressure transducers manufactured by PCB Piezotronics are utilized in the current study, PCB 111A26 is installed on the pre-chamber, and one of two PCB 113B32 mounted on the pressure probe with a quasi-infinite tube installed on the front part of the main chamber, and the other is flush mounted on the back wall on the main chamber. All three sensors record pressure as a 500 kHz sampling rate. Some features to be considered in specifications of dynamic pressure transducers are shown in Table 2.3. All sensors are calibrated by PCB Piezotronics to obtain the sensitivity information before conducting the experiment, so that the voltage data released from the sensors can be converted to the precise pressure data. The resonant frequency of the transducer determines the upper frequency limit that approximately 20% of the sensor resonant frequency is the usable frequency response with the measurement error of 5% [49]. If the frequency of interest is close to the resonant frequency of the sensor or higher, the magnitude of measured pressure will be highly distorted. Rise time is the length of time for the

output of a transducer to rise from 10% of its final value to 90% of its final value when excited by a step change in pressure [50]. The shorter rise time a transducer has, the faster response it shows to the pressure change.

The discharge time constant (DTC) controls the low frequency response of the transducer. It is the time required for the output voltage from a transducer to decline to 37% of its peak value in response to a step increase in input pressure [51]. The lower frequency limit is equal to 0.16/DTC. The piezoelectric pressure transducer is not suitable for static pressure measurements in that the charge output generated from the piezoelectric crystal decreases when there is no input change. Considering the characteristic of the DTC, however, it is able to measure quasi-static pressures. The general rule of thumb for such measurements is that the output signal loss and time elapsed over the first 10% of a DTC have a one-to-one relationship [52]. For example, if a sensor has a DTC of 50 seconds, 10% of the original input signal decays over the first 5 seconds, which is 10% of the DTC. For the pressure transducers employed in the current study, 111A26 has the DTC of 50 seconds, and 113B32 has that of 1 seconds. If the 5% error is allowed, therefore, each sensor is able to measure the static pressure for the event during 2.5 seconds and 50 ms, respectively.

Although the maximum operating temperature of the sensors, 275 °F, is much lower than the flame temperature of the mixtures of hydrogen and methane, the combustion event of the current study is transient, and has the time scale of milliseconds, so the effect of thermal shock and associated signal error should be considered rather than the maximum operating temperature. Heating of the diaphragm and case of a piezoelectric pressure sensor can expand the case, loosening the preload force on the internal crystals, causing a negative signal output [52]. All piezoelectric pressure sensors are practically sensitive to thermal shock, so various methods to minimize the effect of the thermal shock are available. In the current study, the sensor, PT1, measuring pressure of the transient flame in the main chamber is mounted on the pressure probe assembly, so as not to be directly exposed to the thermal shock. Note that the temperature sensitivity coefficient of the sensor is known for steady temperature applied to the sensor, so the coefficient cannot be applied to the thermal shock effect [52].

Table 2.3
Specifications of PCB pressure transducers

	Pre-PT (111A26)	**PT1 and PT2 (113B32)**
Measurement Range	500 psi	5000 psi
Sensitivity (±1.0 mV/psi)	9.906 mV/psi	9.992 mV/psi
Resonant Frequency	≥400 kHz	≥400 kHz
Rise Time	≤1.5 μ sec	≤1.5 μ sec
Discharge Time Constant	≥50 sec	0.3 to 1.0 sec
Temperature Range (Operating)	-100 to +275 °F	-100 to +275 °F
Temperature Coefficient of Sensitivity	≤0.2 %/°F	≤0.1 %/°F
Maximum Flash Temperature	3000 °F	3000 °F
Excitation Voltage	20 to 30 VDC	20 to 30 VDC

2.6.4 Pressure Sensor Probe

Pressure sensor PT2 is flush mounted on the far end wall to measure exact timing and the pressure magnitude of shock wave reflection and other waves. Because the flame front does not reach the end wall during the period of interest, it does not suffer significant temperature effects. In contrast, as mentioned in Section 2.3, PT1 is mounted on the side of the pressure probe assembly, using a stand-off tube in order to avoid heat damage from the flame inside the chamber. This means that pressure magnitude and timing of main-chamber events measured by PT1 are modulated by the tube [53–55]. A transfer function between the actual pressure and the measured pressure is required to use the pressure from PT1. The long coiled tube is connected to the probe to eliminate the effect of the reflected pressure wave in the tube, during the time period of interest. If long enough, the tube may be considered quasi-infinite for the purpose of the experiment. When such reflections of the pressure wave at the end of the tube travel back to the sensor, they would change the pressure signal. Also, the quasi-infinite tube reduces the resonance of the pressure probe [53]. Without the tube, the probe would act like a helmholtz resonator, generating an amplification of the pressure magnitude at a certain frequency.

Englund [56] well described the design parameter effects of the quasi-infinite line pressure probe on measured pressure. Figure 2.18 shows design parameters of the pressure probe. D is the inner diameter of the line, L is the total length of the line, l is the tap length from the measurement end of the line to the transducer, and V_T is the tap volume at the interface of the transducer and the line. Englund reported that attenuation of pressure amplitude decreases and the amplitude of oscillation due to the reflection from the end of the line increases with the increase of the line diameter, the oscillation due to reflection is reduced with the increase of the total length of the line, the reflection effect is somewhat reduced with the decrease of the tab length, and changes in tap volume alter the magnitude of the oscillation from the tap volume at high frequency. From these results, the inner diameter D should

be smaller, the total length L should be longer, the tap length l should be shorter, and the tap volume V_T should be smaller to reduce the reflection effect from the end of the line. Oh [57] suggested that the ratio of the total length to the inner diameter, L/D, should be greater than 200 to provide the advantage of reduction of wave reflection and interruption. The pressure probe with a quasi-infinite tube utilized in the current study is designed as Figure 2.19. The total length is 93 in, and the inner diameter of 1/8 inches tube is 0.069 inches, so the ratio of the total length to the inner diameter, L/D, is 1347.83, which is greater than 200 suggested by Oh. The tab volume is designed as zero, and the tab length is set to 3.75 inches.

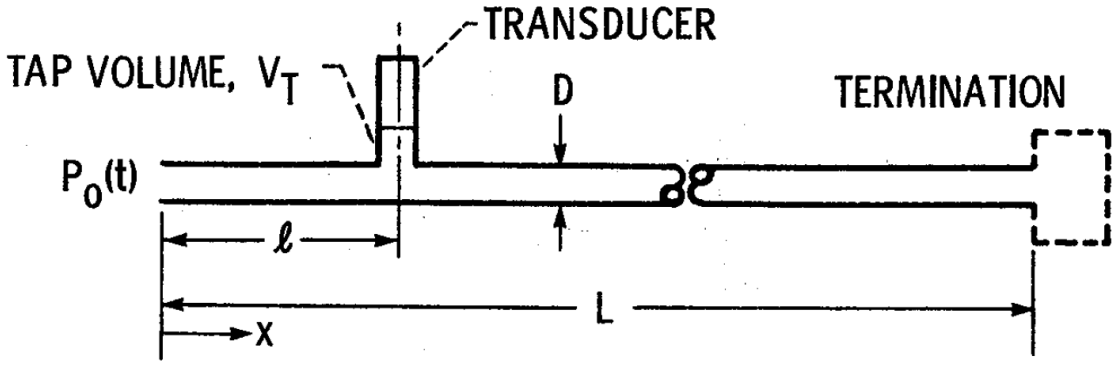

Fig. 2.18. Schematic diagram of the quasi-infinite line pressure probe [56]

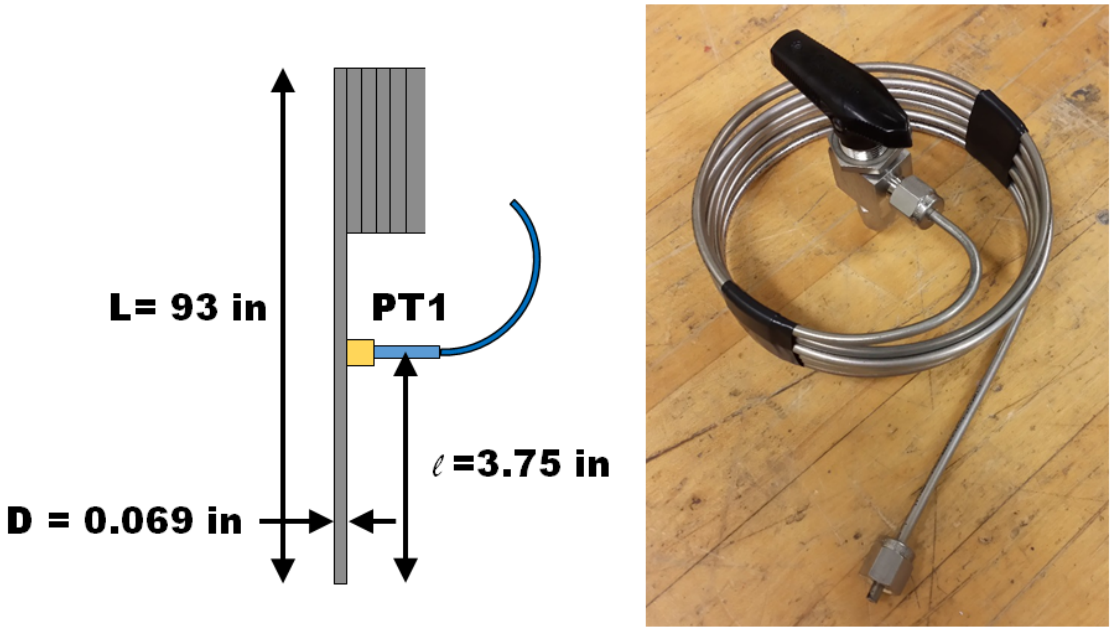

Fig. 2.19. Quasi-infinite line pressure probe with design parameters

2.6.5 High-Speed Image Acquisition System

A Phantom v9.0 monochrome high-speed camera manufactured by Vision Research is used in the current study to record the transient combustion process. A Nikon F-AF Nikkor 50 mm f/1.8 D lens is mounted on the high-speed camera. The minimum focus distance of the lens is 1.5 ft that must be considered when deciding the distance between the camera and the object. Due to the limit of memory capacity inside the camera, the maximum video frame rate in frames per second (fps) is inversely proportional to the image resolution, or the image size. In other words, the image resolution should be smaller to increase the frame rate. By carefully choosing the image size, flame luminosity images and Schlieren images are measured at 20,000 fps and 30075 fps, respectively, which are higher than the experiments of Perera [17] and Chinnathambi [44] which were conducted at 10,000 fps. Further details of the camera conditions are described in Table 2.4.

For these frame rates and correspondingly smaller image resolution, the frame cannot encompass the entire image of the optical window in the main chamber. The main purpose of the measurement of the flame luminosity images is to capture the ignition moment, so the measurement range of the luminosity images is set as 7.5 inches of 14.4 inches from the beginning of the optical window. The Schlieren images are acquired to investigate the interaction of the flame front and the shock waves, which occurs at the end of the main chamber, so the measurement range of the Schlieren images is set as 4.73 inches of 14.4 inches from the end of the optical window. These are illustrated in Figure 2.20.

Table 2.4
High-speed camera setting conditions

	Flame luminosity images	Schlieren images
Frames per second	20000 fps	30075 fps
Image period	50 μs	33.25 μs
Image resolution	400 x 80 pixels	336 x 112 pixels
Pixel per inch	53.34 pix/in	71 pix/in
Exposure time	46.75 μs	30 μs

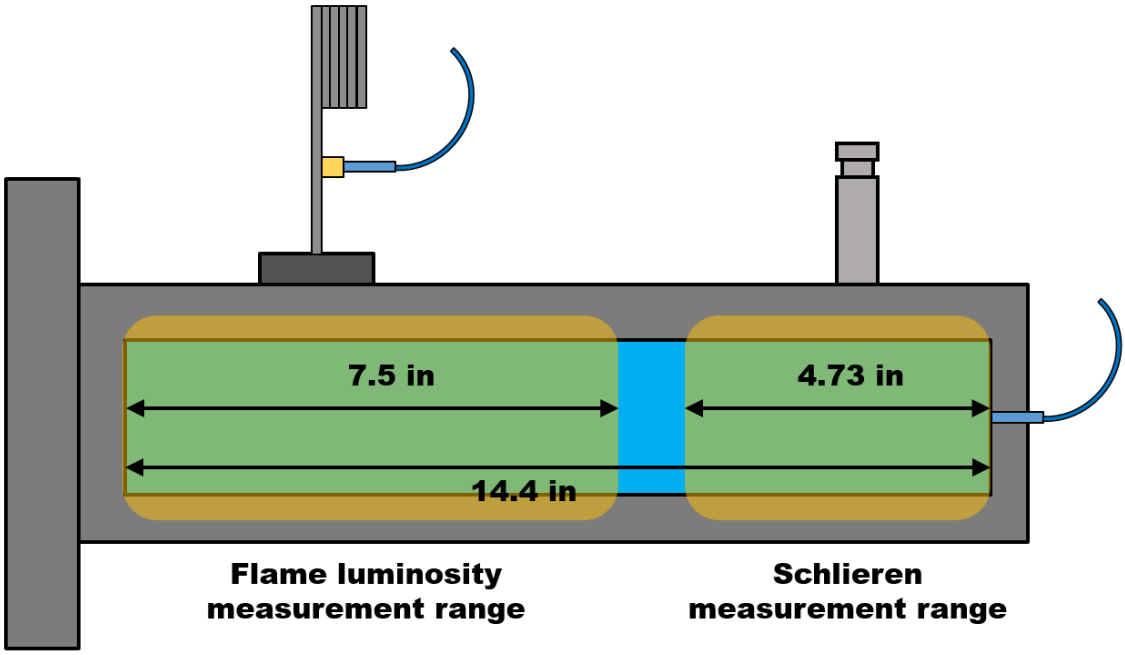

Fig. 2.20. Measurement ranges of the high-speed camera

Gallimore [58] conducted the spectrographic studies for four hydrocarbon fuels, methane, ethylene, propylene, and propane. The author found that the emission wavelengths of radicals and products from the hydrocarbon fuels, such as C_2, H, H_2, CH, and CH_2, are within the range between 400 nm and 700 nm. Boettcher [59] carried out experiments to investigate ignition and flame propagation of a mixture of hexane and air based on the fact that CH* emits light between 420 and 440 nm. Phantom v9.0 has a spectral response in the range of 400-1000 nm, which covers the wavelength ranges of such radical species, so that the high-speed camera is able to identify ignition in the main chamber.

Phantom camera control software (PCC) is used to control and adjust the camera settings. Like the VI of the LabVIEW software, the PCC also recognizes the trigger event and begins to record images as a Cine file automatically. The exposure time, and the extreme dynamic range time (EDR) can be adjusted using the PCC. The exposure time, or the length of time when a cameras shutter is open, varies with the fps, and is set as the maximum allowable exposure times for both flame luminosity and Schlieren measurements in order to capture the slightest illumination in the main chamber to determine ignition accurately. The EDR time, which can be used to adjust exposure on pixel level to reduce over-exposure at certain regions due to bright spots, is maintained at 0 μs for all cases to make the exposure time unchanged for all captured images.

2.7 Schlieren Photography Setup

The Schlieren photography technique is used to investigate the interaction of a flame front and shock waves. The Z-type Schlieren system is employed in the current study in order to maximize the contrast of images in a long, narrow laboratory space as demonstrated in Eq. 1.16. The system is composed of a light source, two concave mirrors, a knife edge, and the high-speed camera as shown in Figure 2.21.

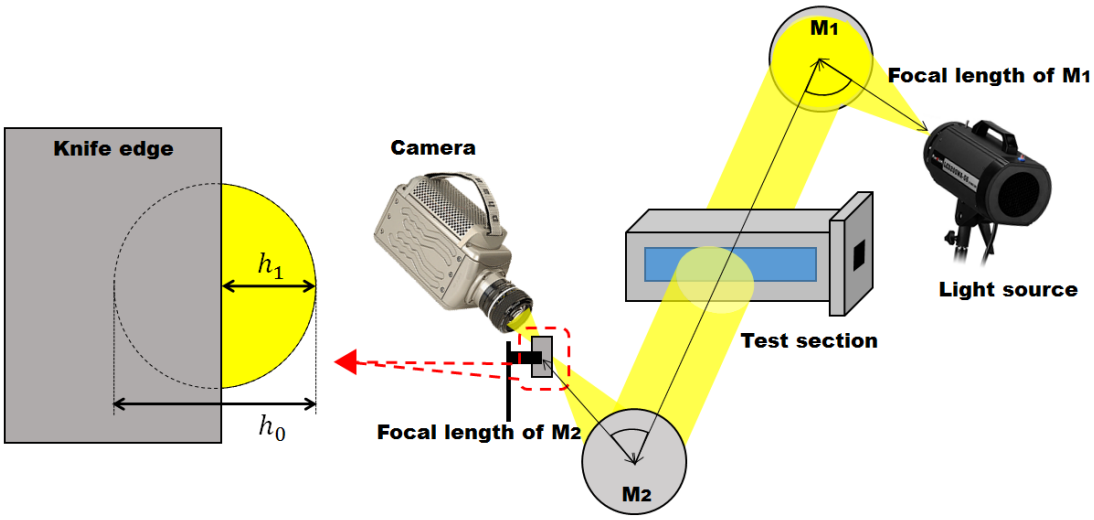

Fig. 2.21. Schematic diagram of the Schlieren setup and the view of the knife edge covering the light beam cross-section

A laser is usually best as the light source of the Schlieren system. A laser system generates a Gaussian beam with high-intensity, from which a tiny circular light source can be derived using an optical lens, to allow an image bright enough in spite of the loss of light intensity by the knife edge. However, due to resource constraints, a high-intensity LED light, LED200WA manufactured by Fotodiox, has been selected instead of a laser system. The LED light is technically used for a studio lamp, but it is able to create a point light source by covering the front of its reflector with a circular plate that has a hole at the center. Two concave mirrors, which have 12.5 inches diameter, and 75 inches focal length, provided by Edmund optics, are located at both right and left sides of the main chamber. In order to make a parallel light beam between the two mirrors, the light source must be placed at the focal point at a distance of 75 inches away from the first mirror. It should be noted that the angle between the light path from the light source to the first mirror and the parallel light path is adjusted no more than 10 degrees to avoid image distortion. The knife edge must be placed at a distance of 75 inches away from the second mirror, at its focal point. The angle of the light path between the knife edge and the second mirror should be no more than 10 degrees with respect to the parallel light path. The distance between two mirrors should be far enough to allow the focal length and the angle issues described above. The camera lens should be placed as close as possible to the knife edge for best image quality, and the aperture in the camera lens should be open at maximum to obtain the shortest depth of focus, otherwise the camera may capture not only images in the test region, but also the images reflected on the second mirror due to the longer depth of focus. Setting the appropriate position of the knife edge can be achieved by checking the Schlieren image acquired by the camera. First, the surface of the knife should be perpendicular to the incident light. If the knife edge is placed at the focal point of the second mirror, the image shows uniform grey color; otherwise either left or right part of the image is dark. The knife edge is moved slightly back and forth near the focal point until the image becomes uniform grey color. The image brightness depends on h_1 in Eq. 1.16, which is the height of the beam cross-section

uncovered by the knife edge, and the intensity of the light source as illustrated in Figure 2.21. The shorter h_1, the higher contrast of the image would be; however, the image will be too dark to recognize if the beam is covered too much. A proper h_1 should be obtained by checking the Schlieren image under the given light intensity.

2.8 Schlieren Image Processing

Due to the interaction with traversing shock waves, the premixed flame in the main chamber has a highly corrugated front. Also, the Schlieren images represent the overlapped effect of all of density gradients in the frame along the line of sight through the cross-section. Thus the observed boundary of the flame front is a two-dimensional projection of the actual three-dimensional front. Nevertheless, the propagation speed of the corrugated flame front, can be estimated by extracting the front line of the flame using image processing.

An image processing code written in MATLAB has been applied to extract the flame front line from Schlieren images. Figure 2.22 shows the procedure of the image processing. It is acknowledged that the overlapped density gradients make the boundary of the flame front ambiguous. However, the flame front edge has very high density gradients such that even a line-of-sight projection should be easily distinguished. First, a Gaussian filter is used to remove relatively lower density gradients by smoothing the image. $Imgaussfilt$, a MATLAB function of the Gaussian filter, has been applied with a standard deviation value, which is found by trial and error method for each case. Second, a flame front edge is roughly found using the Canny edge-detecting function. The Canny algorithm basically detects edges where the gradient of the greyscale intensity of the image is the highest. Gradients at each pixel in the Gaussian filtered image are determined by applying what is known as the Sobel-operator [60]. After applying the Canny edge-detection function, the point which has the highest density gradient is expressed as a pixel value of 255, otherwise the pixel values are 0. The image shows that the flame edge is connected to two lines at the

top and bottom sides, which are the optical window cover, and may have unnecessary lines as shown in (3) of Figure 2.22. If the unnecessary lines are removed, the position of the flame edge can be detected regardless of the top and bottom lines because only the first point which has a pixel value of 255 in a row is counted as a position of the flame edge. Several MATLAB functions are utilized to remove these lines. The *imdilate* function enlarges the size of each point to a designated size, connecting adjacent points to create a closed part including the flame edge, and then, the closed part is filled using the *imfill* function, creating a lump of 255 pixel points. After applying the *imerode* function, which puts back the size of each point, redundant points or lines are clearly separated from the big white part like the picture (6) of Figure 2.22. The *bwareaopen* function deletes areas of 255 pixel value smaller than a designated pixel size, removing the redundant points or lines. Lastly, the lump of 255 pixel points gets empty using the *bwperim* function, remaining only the flame edge with two top and bottom lines. The image processing code reads the value of pixels one by one from the top-left corner of the processed image, and if a pixel has a 255 value, record the x and y position of the pixel, reading the next below row. When all positions of pixels consisting of the flame edge are recorded, an average value of x positions is calculated, which represents the flame edge position.

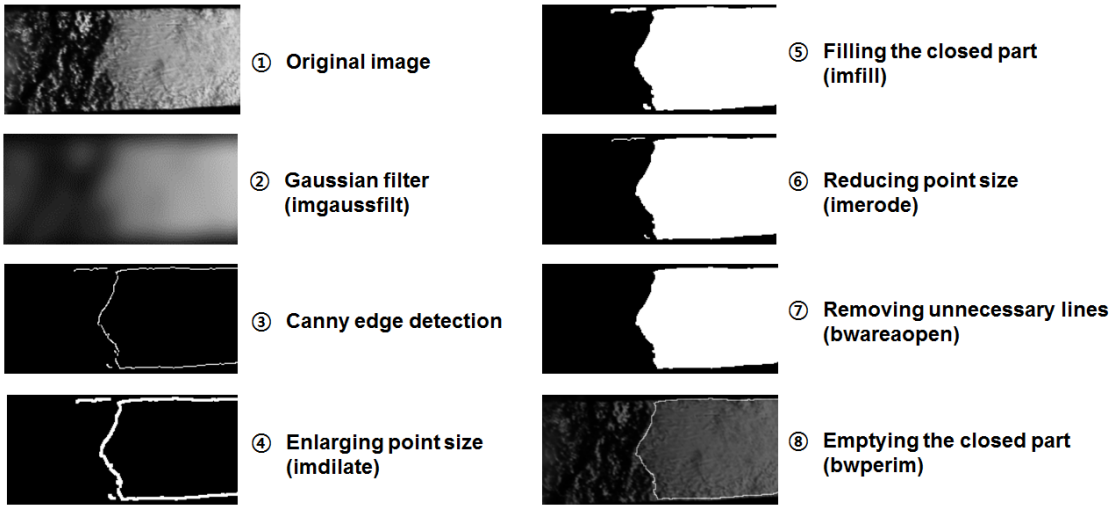

Fig. 2.22. Image processing procedure for extracting a flame front line from the original Schlieren image

2.9 Experimental Procedure

The preparation for the experiment begins with assembling the nozzle insert. An aluminum diaphragm is properly scored, and installed in the nozzle insert. The nozzle insert is then fixed in the cavity on the pre-chamber. Using a vacuum pump shown in Figure 2.12, the inside of the pre-chamber is vacuumed until the gauge pressure of the pre-chamber approximately reaches to -10 psig. Desired amounts of hydrogen and methane can then be precisely supplied into the pre-chamber by adjusting a choke valve according to the pressure table developed from Eq. 2.14 for achieving the desired air/fuel ratio in the pre-chamber.

Fueling the external chamber is performed by following the procedure suggested in Section 2.5.2. Once the external chamber is ready to fuel, the main chamber is tightly fixed, and attached on the pre-chamber with no gap between the two chambers. The main chamber is then vacuumed, and the fuel mixture in the external chamber is supplied into the main chamber according to the pressure table prepared in Section 2.5.2.

After the chambers are fueled, the data-acquisition LabVIEW VI front panel and the camera control software are primed to be ready to accept the trigger signal from the synchronizing circuit, by pressing the stand-by buttons for each recording system. Then, a trigger button on the remote control box in Figure 2.8 is pressed, causing the spark plug in the pre-chamber to fire. This ignites the air/fuel mixture, and the camera and the pressure DAQ start to record data simultaneously.

After the spark ignition, the air/fuel mixture in the pre-chamber is combusted, building up pressure inside the pre-chamber. The diaphragm is ruptured at certain pressure, called the rupture pressure. Once the diaphragm is ruptured, hot reactive jet is injected into the main chamber, igniting the air/fuel mixture after a few or several milliseconds, called the ignition delay time.

When combustion is finished in both chambers, the main chamber is disengaged, and the nozzle insert is detached from the pre-chamber. Each run of the experiment is terminated by purging the product gases in each chamber using high-pressure air.

2.10 Experimental Conditions

The experimental conditions are described in Table 2.5. Mixtures of hydrogen and methane are selected as fuel, and the oxidizer is assumed to be room air with humidity of 50%. For the pre chamber, the CH_4:H_2 fuel ratio by volume is fixed at 50:50, and the equivalent ratio is fixed at 1.1. For the main chamber, two fuel ratios are adopted, with CH_4:H_2 by volume set at 50:50 and 30:70, to investigate the effect of the change of the hydrogen enrichment to methane on ignition and combustion processes. The equivalent ratio of the main chamber varies from 0.4 to 1.0. In order to observe the effect of the amount variation of the hot reactive jet injection on the main chamber ignition process, diaphragm rupture pressure is varied from 30 psig to 55 psig by varying the number of indentation on the diaphragm.

Table 2.5
Experimental conditions

Fuel	$\boldsymbol{H_2, CH_4}$
Oxidizer	Room Air
Pre-chamber Fuel Ratio ($\boldsymbol{CH_4 : H_2}$)	50:50
Pre-chamber Equivalent Ratio	1.1
Main Chamber Fuel Ratio ($\boldsymbol{CH_4 : H_2}$)	50:50 , 30:70
Main Chamber Equivalent Ratio	1.0, 0.8, 0.6, 0.4
Diaphragm Rupture Pressure (psig)	30~55

3. IGNITION DELAY TIME INVESTIGATION

3.1 Repeatability Test of Pre-chamber Combustion

Combustion repeatability is tested with a hydrogen-methane-air mixture in the pre-chamber to evaluate the reliability and consistency of the torch jet production under fixed initial conditions. The tests are performed with a fixed fuel ratio, 50:50 (CH_4:H_2 by volume), and three different equivalence ratios, 0.9, 1.0, and 1.1 to determine the best condition reducing the diaphragm rupture time, and each condition repeats three times. Figure 3.1 illustrates pre-chamber pressure records with three different equivalence ratios. Three pressure records of each equivalence ratio condition show similar results, and it is presumed that slight differences of each condition are resulted from variations of the spark energy, and minor changes of the depth of the diaphragm indentation, in addition to any measurement errors in preparing the mixtures.

The pressure increase rate is the fastest at equivalence ratio 1.1, and the slowest at 0.9. This is highly related to the laminar burning velocity of the pre-mixed air/fuel mixture. The pre-mixed mixture is consumed at the laminar burning velocity, increasing pressure in a constant volume by releasing heat; therefore, the faster the burning velocity, the faster the pressure increase rate. Hermanns [61] experimentally investigated the laminar burning velocities of hydrogen-methane-air mixtures with varying hydrogen contents using a heat flux method, and the maximum laminar burning velocity is close to the equivalence ratio 1.1 as the hydrogen content increases from 0 to 40%. Hu [62] also experimentally measured the laminar burning velocity of hydrogen-methane-air mixtures with different amounts of hydrogen in a constant volume chamber, and found that the laminar burning velocity is maximum at the equivalence ratio 1.1 when the hydrogen content is less than 50%. Hu reported that

there is a clear relationship between the laminar burning velocity and the radical concentrations of H and OH in the reaction zone of premixed flames, so it is expected that the concentration of H and OH radicals is maximum at the equivalence ratio 1.1, leading to the fastest burning velocity and pressure increase rate in a constant-volume chamber.

The highest pressure in the pre-chamber is observed at 1.1 among three equivalence ratios. The maximum pressure in the pre-chamber is determined by a combination of four effects; the adiabatic flame temperature of the mixture, the laminar burning velocity, heat loss through the wall, and the product gas release through the nozzle after the diaphragm rupture. According to Boushaki [63], the highest adiabatic flame temperature of the hydrogen-methane mixture, 50:50 by volume is at equivalence ratio 1.0, calculated by GRI-Mech 3.0 as shown in Figure 3.2. However, assuming that the diaphragm ruptures at the same pressure for all cases, the 1.1 condition can develop a higher maximum pressure in the constant volume chamber due to the faster laminar burning velocity. It is expected that the time scale of heat loss through the chamber wall is significant compared to the flame propagation time according to laminar burning velocity. Thus, the faster burning condition will tend to lose relatively less heat. In order to clarify the trend of the maximum pressure in the pre-chamber, more investigations including the flame temperature and the heat loss rate through the wall are necessary.

The equivalence ratio 1.1 has been selected as a condition of the pre-chamber combustion considering that it has a faster pressure increase rate and higher maximum pressure compared to other conditions of the equivalence ratio, increasing the amount of hot-jet mass injected into the main chamber. Furthermore, a fuel-rich mixture contains more active radicals when burning, with the radicals expected to be active through the nozzle discharge process. Both reasons contribute to the decrease of the ignition delay time of the air/fuel mixture in the main chamber in that the former increases the ignition energy, and the later rises the reactivity.

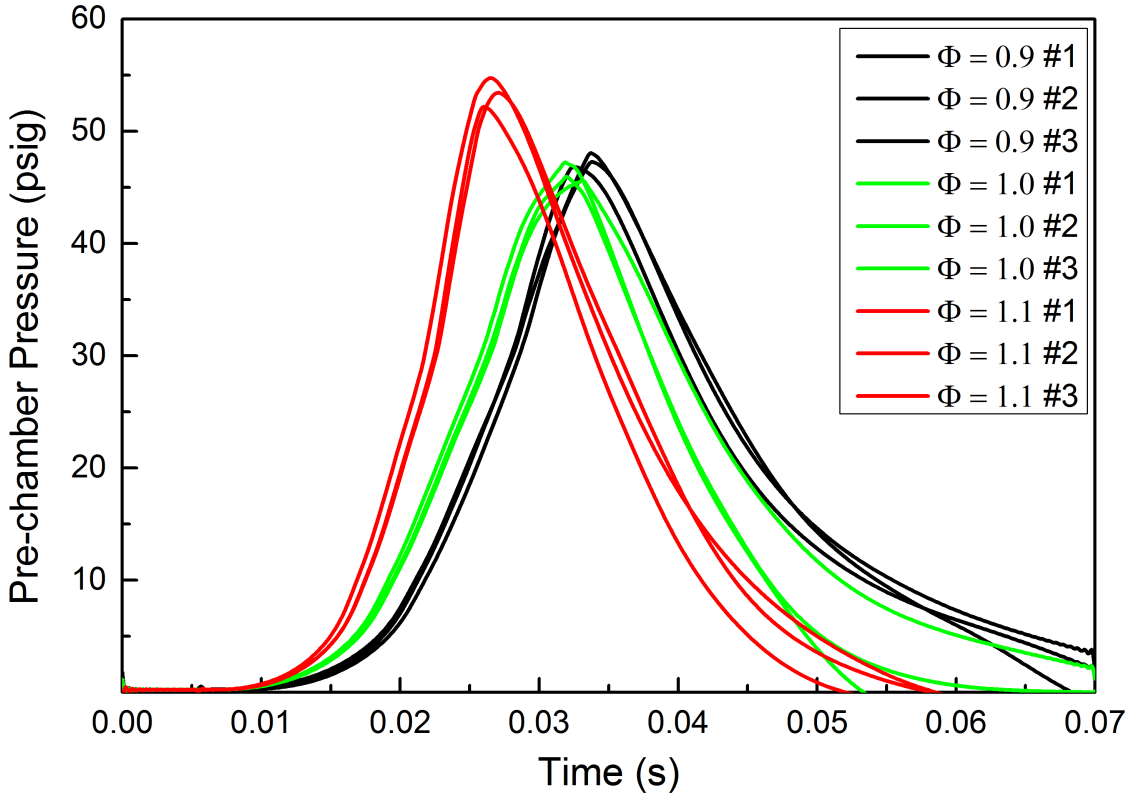

Fig. 3.1. Pre-chamber pressure records with three different equivalence ratios

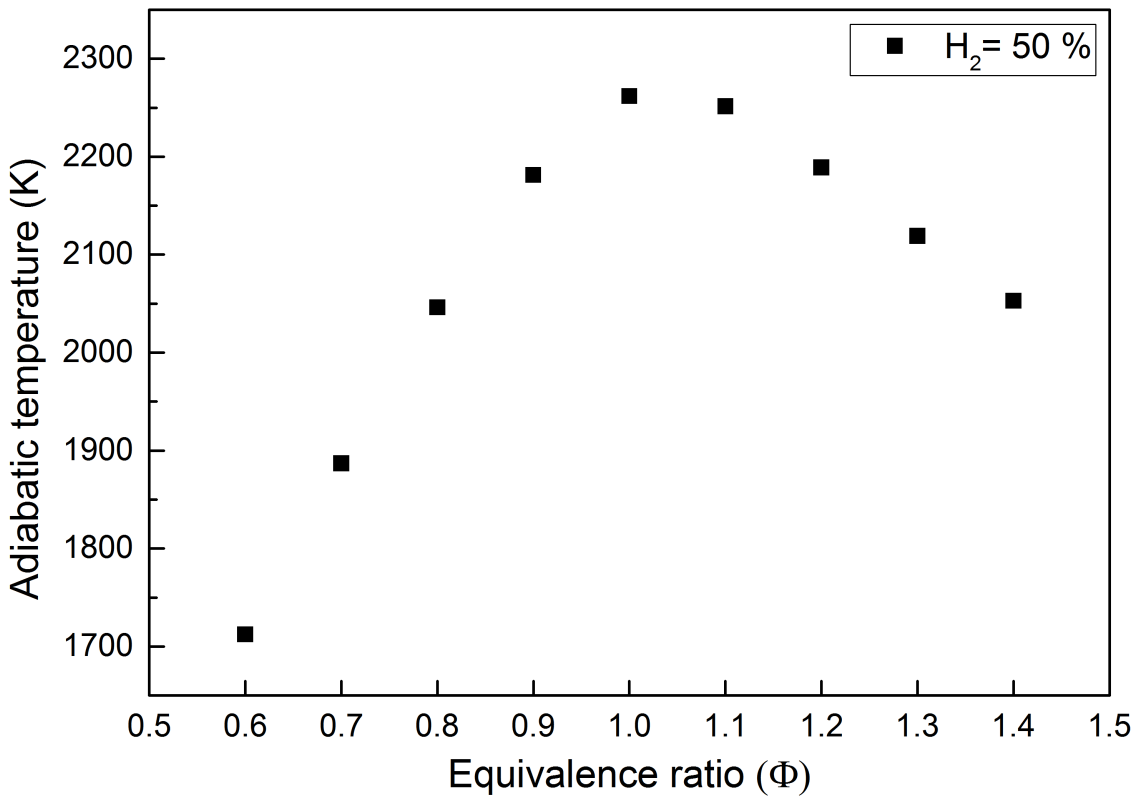

Fig. 3.2. Calculated adiabatic flame temperature of hydrogen and methane mixture with respect to equivalence ratio at 1 bar and 300 K [63]

3.2 Initial Shock Speed Measurement

When the diaphragm ruptures, an initial shock is generated by the sudden pressure difference between two chambers, propagating inside the main chamber prior to the ignition of the air/fuel mixture in the main chamber. In the current study, tracking of the initial shock is utilized to obtain precisely the diaphragm rupture time, and thus the ignition delay time. In previous studies, the delay was calculated based on the average diaphragm rupture time, causing uncertainty in that the rupture time slightly varies with cases. We also evaluate the effect of the rarefaction waves, which influences the ignition delay time by weakening the effect of the compression waves.

In an actual wave rotor, a hammer shock is generated by a sudden closure of the outlet port in a wave rotor drum, increases pressure and temperature of the mixture in the chamber, contributing to reducing the ignition delay time. Ideally, the hammer shock is mostly cancelled by proper timing of the inlet port closing, but some strong residual shock waves remain. These waves are not present in the present experiment.

The propagation speed of the initial shock is assumed as constant along the main chamber until the shock wave is reflected at the end wall given that the cross section area of the chamber is constant, the gas mixture is well mixed, and the travelling time of the shock along the length of the main chamber, 16 inches, is at most 1.13 ms with the sound speed of the air/fuel mixture, 360 m/s, so that the decrease of the shock propagation speed by friction and heat transfer can be ignored. When the shock wave passes by the diaphragm of a piezoelectric pressure transducer, which has a diameter of 0.218 inches providing a good spatial resolution, the transducer measures the pressure difference between the front and the rear of the shock, expressing a sudden pressure rise. The initial shock speed is measured using the time information of the sudden pressure rise from two pressure transducers, PT1 and PT2, and validated using high-speed Schlieren images. As shown in Figure 3.3, the red line and the blue line indicate pressure records of PT1 and PT2, respectively. Both lines show sudden pressure rises by the shock wave, and the moment of the shock wave passing is defined

as the peak of 1st order differential of the pressure record. Note that PT1 is mounted on a pressure probe, 3.75 inches away from the chamber inner surface, so the shock travelling time in the pressure probe should be considered. The propagation speed of the shock in the pressure probe varies with that in the main chamber due to a sudden geometry change; however, it is anticipated that the speed change is not substantial considering the length between PT1 and the chamber, therefore, it is assumed that the propagation speeds of the shock in the main chamber and the pressure probe are identical. In Figure 2.9, the distance between the pressure probe and PT2 is 12.7 inches, but the actual distance between PT1 and PT2 is 8.95 inches in light of the shock propagation in the pressure probe. The propagation speed of the initial shock wave is calculated as the distance between PT1 and PT2 over the time gap between two peaks of 1st order differential of pressure records. For example, the time gap between two peaks of 1st order differential of the case in Figure 3.3 is 0.56 ms , and the distance between two PTs is 8.95 inches, so the shock propagation speed of the case is 15980 in/s, or 406 m/s.

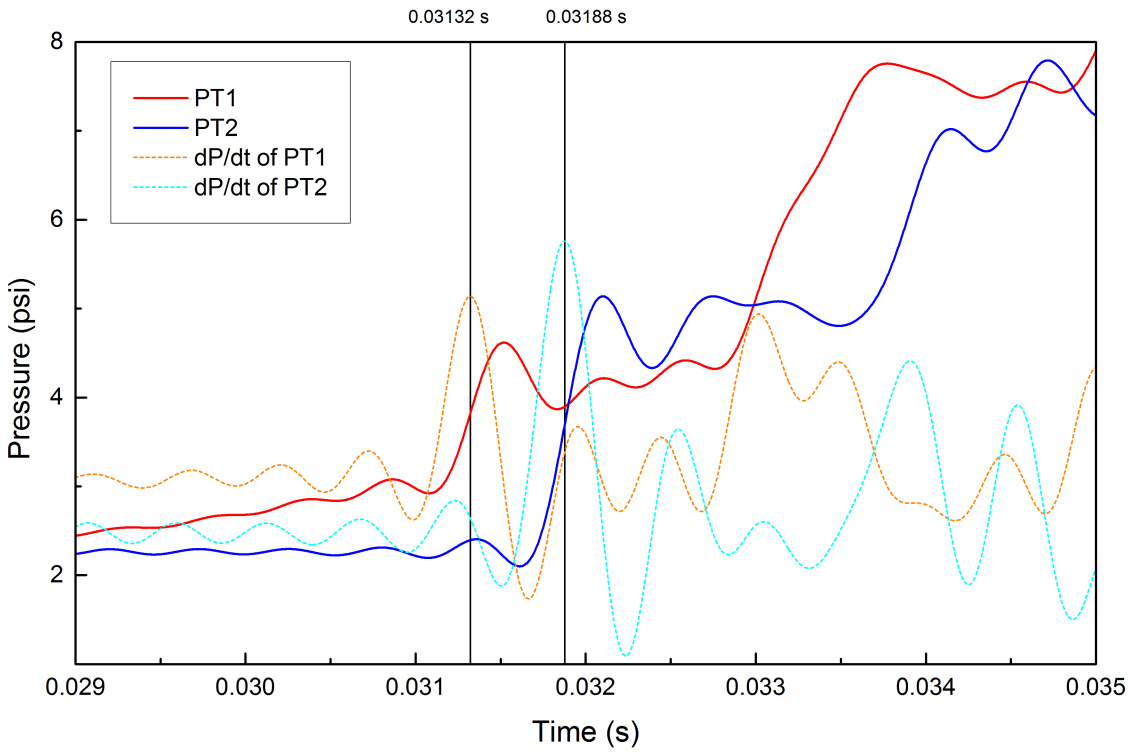

Fig. 3.3. Measurement of the propagation speed of the Initial shock wave using pressure records of PT1 and PT2 (Main chamber condition: Φ=0.8, H_2=50%, indentation #=2, case #=2)

The high-speed Schlieren photography technique visualizing the image of shock waves by optically capturing the sharp density gradient across a shock wave as described in Chapter 1.3.4 is utilized to validate the propagation speed of the initial shock wave using a known time interval of Schlieren images and shock wave positions. Figure 3.4 shows a series of time-resolved, post-processed Schlieren images representing the initial shock propagation, and a graph of the shock wave x-position with respect to time for a case of the equivalence ratio Φ=1.0 and the hydrogen content 70%. The time interval between images is 33.25 μs, and pixel per inch is 71 pix/in as described in Table 2.3. In the Schlieren images, the shock wave is the right edge of the thick white line. Although the light path passing through the main chamber is perpendicular to the side of the chamber when setting up the Schlieren system, a thick white line following the shock observed. It is assumed that poor quality of recently replaced quartz windows causes light spreading. Window replacement is highly recommended for further experiments. At 6th and 7th images, a second discontinuity is observed following the initial shock wave with a certain distance is observed. This discontinuity is known as a contact surface, that will be discussed later, separating the mixture gas in the main chamber from the hot-jet of the pre-chamber. The graph shows a clear linear trend between the shock x-position and the time, indicating that the initial shock propagation speed is constant. This trend is observed for all Schlieren test cases, so the assumption that the initial shock speed is constant is reasonable. The propagation speed of the initial shock wave can be measured using the high-speed Schlieren technique in this manner, and the result of all cases are represented in Figure 3.5 and Table 3.1 with the propagation speed measured using the pressure data.

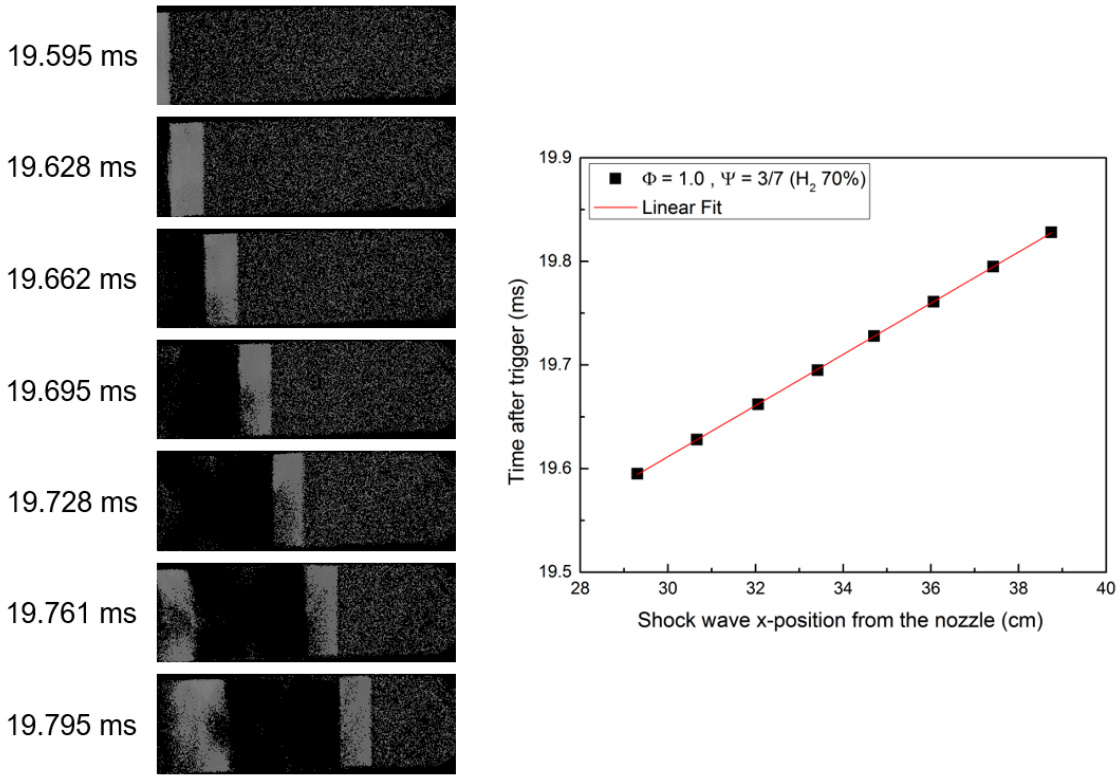

Fig. 3.4. Time-resolved, post-processed Schlieren images of the initial shock wave propagation, and a graph of the shock wave x-position with respect to time (Main chamber condition: Φ=1.0, H_2=70%)

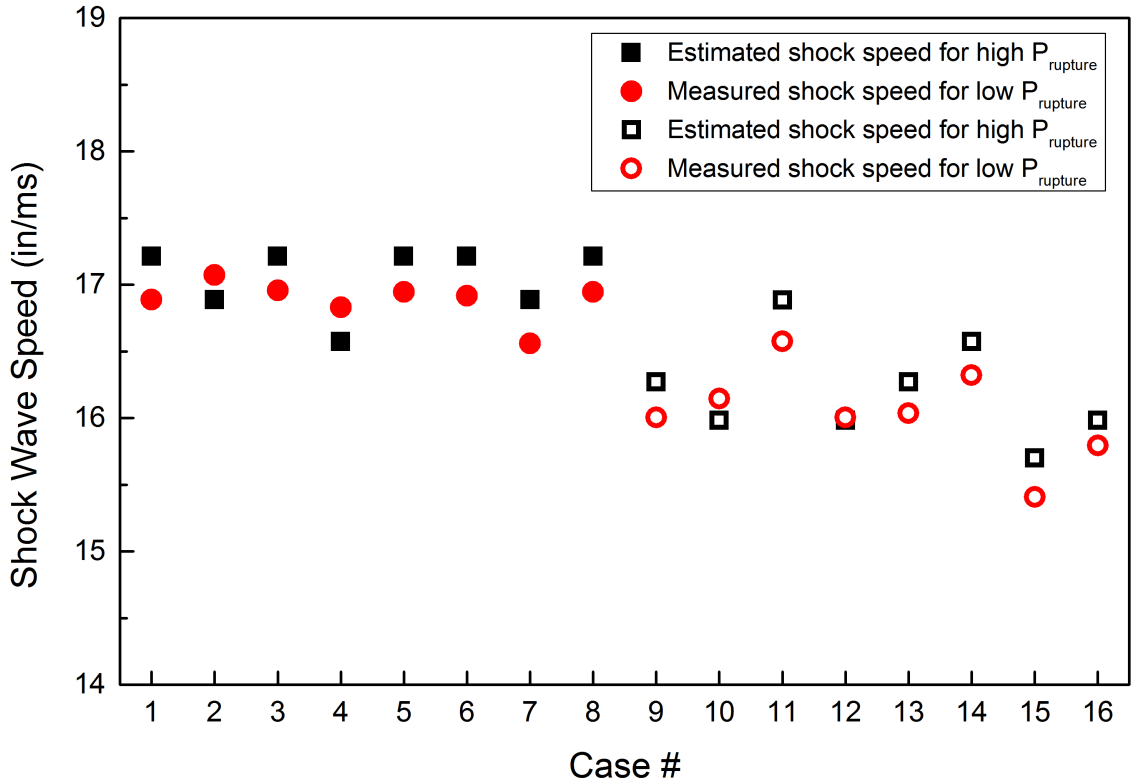

Fig. 3.5. Validation of the initial shock speed estimation

In order to examine the effect of the diaphragm rupture pressure, two different indentation depths on the diaphragm are applied. The higher rupture pressure and the lower rupture pressure correspond to scoring the diaphragm one time and three times, respectively. Each case number corresponds to different test conditions of the equivalence ratio, the hydrogen content in the fuel mixture, and the diaphragm rupture pressure as represented in Table 3.1. In Figure 3.5, the initial shock speed highly depends on the diaphragm rupture pressure as the trend of the initial shock wave speed with respect to the diaphragm pressure ratio, or the driver-to-driven pressure ratio. Liepmann [64] explains that a higher driver-to-driven pressure ratio causes a faster initial shock wave speed when the diaphragm ruptures. Eq. 3.1 [65] is the shock tube relation which is suitable to explain the result of Figure 3.5.

$$\frac{P_4}{P_1} = \frac{2\gamma_1 M_S^2 - (\gamma_1 - 1)}{\gamma_1 + 1} \cdot [1 - \{\frac{a_1(\gamma_4 - 1)}{a_4(\gamma_1 - 1)}\}\{M_S - \frac{1}{M_S}\}]^{-\frac{2\gamma_4}{\gamma_4 - 1}} \tag{3.1}$$

In Eq. 3.1, P is pressure, γ is the specific heat ratio, a is the speed of sound, and Ms is the Mach number of the initial shock wave. The subscripts 1 and 4 refer to the conditions of the shock front and inside the pre-chamber, respectively. The diaphragm pressure ratio is mainly affected by Ms, which is hundreds meter per seconds, due to the square term, but the specific heat ratio does not affect the pressure ratio change since the range of its variation within the test condition is small, from 1.3999 to 1.4009, therefore, the shock wave speed with respect to the case number does not show a notable increasing or decreasing trend.

Considering errors which are less than 2% in Table 3.1 between the calculated shock speed based on the pressure data and the measured shock speed obtained by the Schlieren test, the initial shock speed can be estimated in this manner for convenience and consistency of the calculation in the current study. It appears that the systematic error arises from the way to define the shock travelling time between PT1 and PT2 described in Figure 3.3. The shock arrival time on each pressure transducer is decided as the peak of 1st order differential of the pressure record, and the time slightly varies

with a low-pass filter which is applied to the pressure signal to reduce the background noise. The 2000 Hz low-pass filter is applied to all pressure data.

Table 3.1
Validation results of the initial shock speed estimation

Case #	Condition	Calculated shock speed (in/ms)	Measured shock speed (in/ms)	Error (%)
1	Φ= 1.0 H_2=50% $P_{rupture}$: high	17.21	16.89	-1.89
2	Φ= 1.0 H_2=70% $P_{rupture}$: high	16.89	17.07	1.05
3	Φ= 0.8 H_2=50% $P_{rupture}$: high	17.21	16.96	-1.47
4	Φ= 0.8 H_2=70% $P_{rupture}$: high	16.57	16.83	1.54
5	Φ= 0.6 H_2=50% $P_{rupture}$: high	17.21	16.95	-1.53
6	Φ= 0.6 H_2=70% $P_{rupture}$: high	17.21	16.92	-1.71
7	Φ= 0.4 H_2=50% $P_{rupture}$: high	16.89	16.56	-1.99
8	Φ= 0.4 H_2=70% $P_{rupture}$: high	17.21	16.95	-1.53
9	Φ= 1.0 H_2=50% $P_{rupture}$: low	16.27	16.01	-1.62
10	Φ= 1.0 H_2=70% $P_{rupture}$: low	15.98	16.15	1.05
11	Φ= 0.8 H_2=50% $P_{rupture}$: low	16.89	16.58	-1.87
12	Φ= 0.8 H_2=70% $P_{rupture}$: low	15.98	16.01	0.19
13	Φ= 0.6 H_2=50% $P_{rupture}$: low	16.27	16.04	-1.43
14	Φ= 0.6 H_2=70% $P_{rupture}$: low	16.57	16.32	-1.53
15	Φ= 0.4 H_2=50% $P_{rupture}$: low	15.70	15.41	-1.88
16	Φ= 0.4 H_2=70% $P_{rupture}$: low	15.98	15.79	-1.20

3.3 Diaphragm Rupture Timing and Pressure

In order to determine the diaphragm rupture pressure, a way to measure the diaphragm rupture moment, which also can be used to estimate the ignition delay time, is suggested in this section. The rupture pressure is defined as a pressure corresponding to the moment when the diaphragm ruptures. The rupture moment can be estimated using the information of the initial shock wave speed. On an assumption that the initial shock is generated right after a rupture of the diaphragm, and propagates with a constant speed until reaching the end of the main chamber, the diaphragm rupture moment can be obtained following Eq. 3.2. The diaphragm rupture moment is equal to the shock arrival time at the end wall minus the shock travelling time from the nozzle to the end wall.

$$\tau_{rupture} = \tau_{PT2\ peak} - \frac{L_{main\ chamber}}{U_{initial\ shock}} \tag{3.2}$$

A test has been conducted to validate Eq. 3.2. The high-speed camera is set as shown in Figure 3.6 to observe the nozzle outlet so that the diaphragm rupture time can be directly measured by the camera with a high sampling rate, 40000 fps, and simultaneously, the pressure data is recorded to obtain the rupture time calculated by Eq. 3.2, which is compared with the measured one. All conditions of the hydrogen content and the equivalence ratio employed in the current study are examined. As the result of the test showing in Figure 3.7 and Table 3.2, the error between the times from the calculation and from the measurement of the high-speed camera is 0.5% at most, so it is verified that the diaphragm rupture moment can be estimated in this manner.

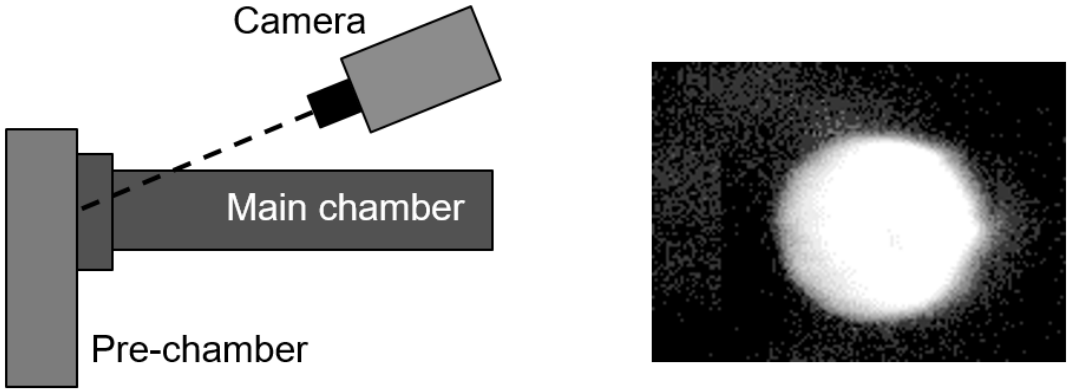

Fig. 3.6. Top-view of the setup for the validation test of the diaphragm rupture moment (left), and an image of the diaphragm rupture moment taken by the high-speed camera (right)

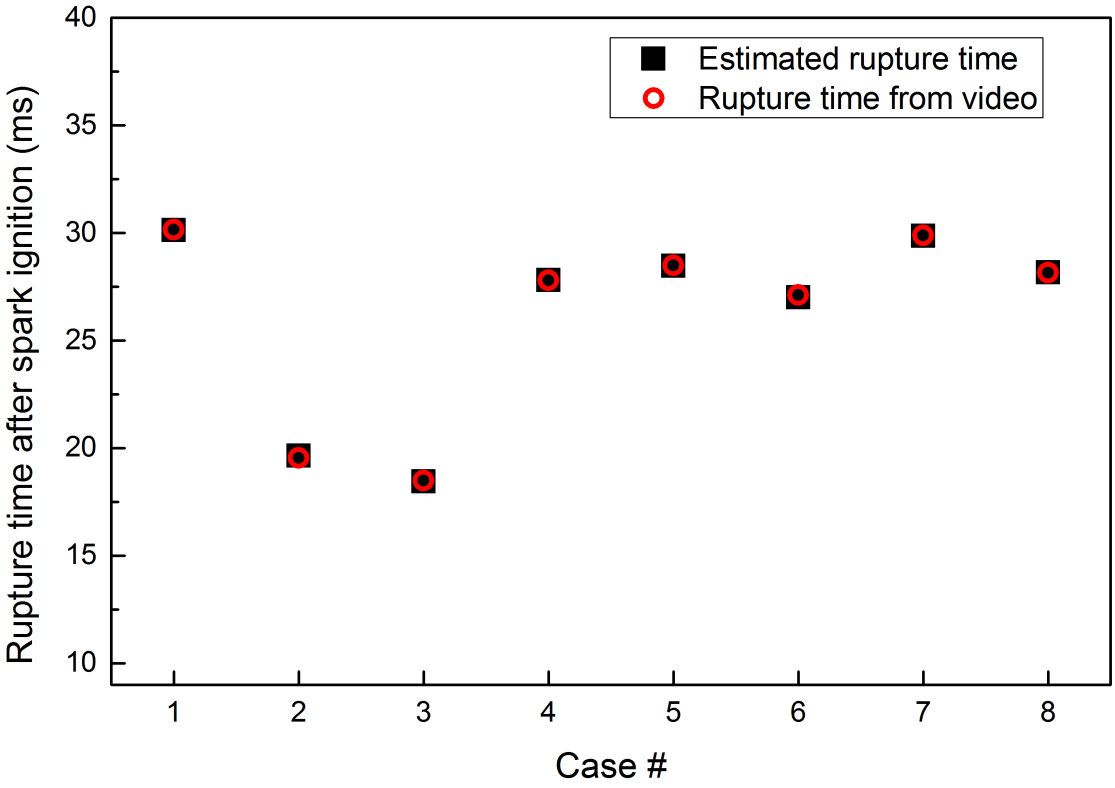

Fig. 3.7. Validation of the diaphragm rupture moment estimation

The amount of hot-jet mass injection through the nozzle and the propagation speed of the initial shock speed are strongly related to the diaphragm rupture pressure, and both the mass injection amount and the initial shock speed affect the ignition delay time of the air/fuel mixture in the main chamber. Therefore, the diaphragm rupture pressure is controlled by varying the number of indentation on the diaphragm in order to investigate the effect of the diaphragm rupture pressure on the ignition delay time. The diaphragm, as described in Section 2.1.3, is scored as a cross form, and it can be ruptured at lower pressures of the pre-chamber as the number of indentation increases. Diaphragm rupture tests with the different indentation number has been performed, and the result is presented in Figure 3.8.

Indentation #1 indicates that a diaphragm is scored back and forth one time, and the indentation number varies from one to three. A total of five cases are conducted for each indentation number. The indentation number one, two and three show average rupture pressures of 50.19, 40.59, and 33.88 in psig, respectively, revealing that the diaphragm rupture pressure can be controlled by varying the indentation number on a diaphragm. However, it is difficult to obtain the same rupture pressure although diaphragms are scored with the same number of indentation since the depth of indentation on diaphragms cannot be perfectly the same. So the rupture pressure of each test case should be considered for analysis of the ignition delay time.

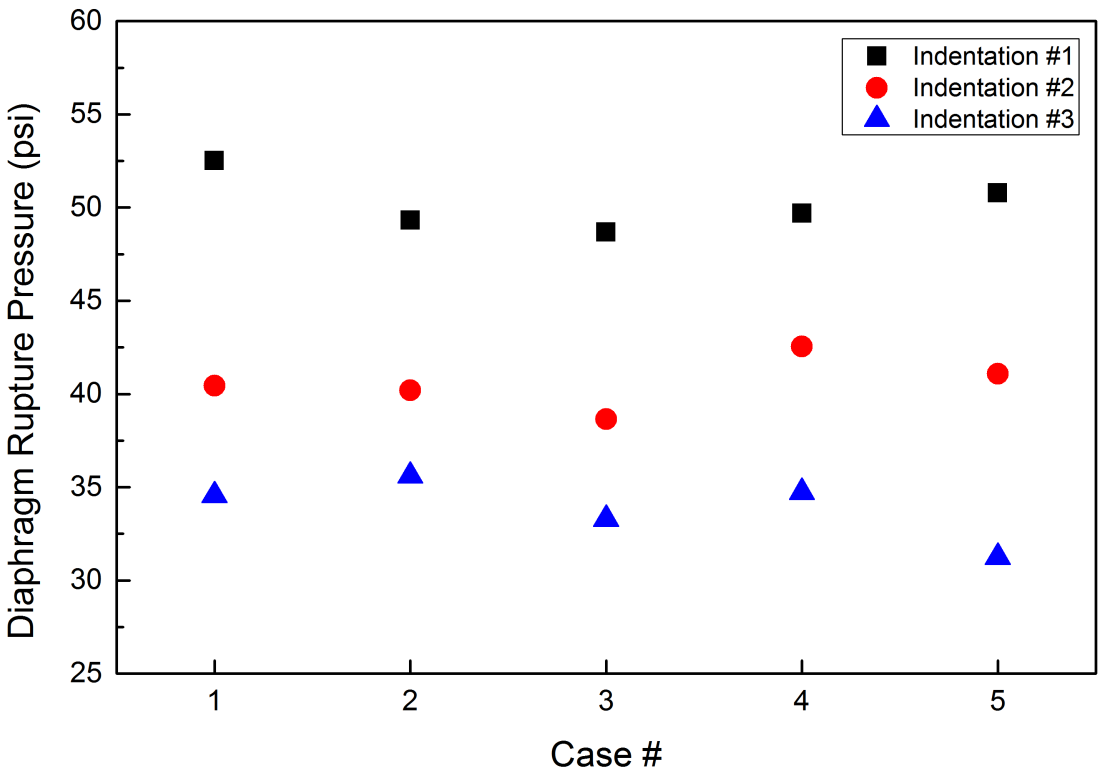

Fig. 3.8. Diaphragm rupture pressure is controlled by the number of indentation on a diaphragm

Table 3.2
Validation of the diaphragm rupture moment estimation

Case #	Φ	H_2 (%)	PT1 dP/dt peak (ms)	PT2 dP/dt peak (ms)	Shock speed (in/ms)	Rupture moment from calculation (ms)	Rupture moment from video (ms)	Error (%)
1	1	50	30.57	31.12	16.27	30.13	30.16	0.08
2	1	70	19.98	20.41	20.81	19.64	19.54	0.50
3	0.8	50	18.88	19.43	16.27	18.44	18.49	0.25
4	0.8	70	28.19	28.68	18.27	27.80	27.79	0.03
5	0.6	50	28.91	29.47	15.98	28.47	28.49	0.07
6	0.6	70	27.45	28.02	15.70	27.00	27.13	0.47
7	0.4	50	30.29	30.83	16.57	29.86	29.88	0.06
8	0.4	70	28.58	29.10	17.21	28.17	28.15	0.06

3.4 Reflected Shock Pressure Measurement

The shock tube experiment is used to investigate compressible flow phenomena, gas phase combustion reactions, or aerodynamic phenomena with a broad range of temperatures and pressures which are difficult to be conducted in other types of test facilities. Among several types of the shock tube setup designed to suit its own purpose, especially a type of combustion heating of the driver section has a few similarities with the current study setup. The shock tube setup using combustion generates an initial shock wave by bursting a diaphragm with combustion in the driver section so that a greater shock strength can be achieved due to high temperature of the driver gas which increases a sound speed [66, 67]. In the shock tube studies of chemical kinetics, a reactant mixture in the driven section is ignited by compression through a reflected wave, which increases temperature and pressure of the mixture higher than the auto ignition point. In contrast, the current study the mixture in the main chamber equivalent to the driven section is ignited by hot-reactive gas from the pre-chamber equivalent to the driver section. The reason that the shock tube experiment is mentioned at the beginning of this section is that both systems, the shock tube and the current study, have some resemblance in several steps before ignition, so these will be briefly introduced to help understanding attenuation of the reflected shock strength. However, it is noted that in a classical shock-tube there is no flow restriction or nozzle between the two sections, and the two sections are usually tubes with equal cross-section. This is a major difference with respect to the present experiment.

3.4.1 Simple Shock Tube Model

The shock tube is initially separated into two parts, zone 1 and zone 4, which correspond to subscripts 1 and 4 of the top image in Figure 3.9. The two parts are posited to have the same cross-section area. A diaphragm located between two zones maintains the initial state that gas in zone 1 has a pressure P_1, a sound speed a_1,

and a specific heat ratio γ_1, and gas in zone 4 has a pressure P_4 which is higher than P_1, and a sound speed a_4, and a specific heat ratio γ_4. At a particular instant, the diaphragm ruptures and disappears to have the two sections connected with no obstruction. Thereupon, as shown in the second image of Figure 3.9, an initial shock wave, or incident shock wave propagates into zone 1 at Mach number Ms, changing the gas state from zone 1 to zone 2 behind the shock, so the gas in zone 2 has higher pressure and temperature than those of the gas in zone 1. On the other side, expansion or rarefaction waves move into zone 4, changing the gas state from zone 4 to zone 3, so the gas in zone 3 has lower pressure, temperature, and density than those of the gas in zone 4. Between zone 2 and zone 3, a contact surface follows the incident shock wave, and pressure P and gas velocity u are same across the contact surface, but temperature T and density are not. The bottom image of Figure 3.9 illustrates movements of all waves as a distance-time diagram.

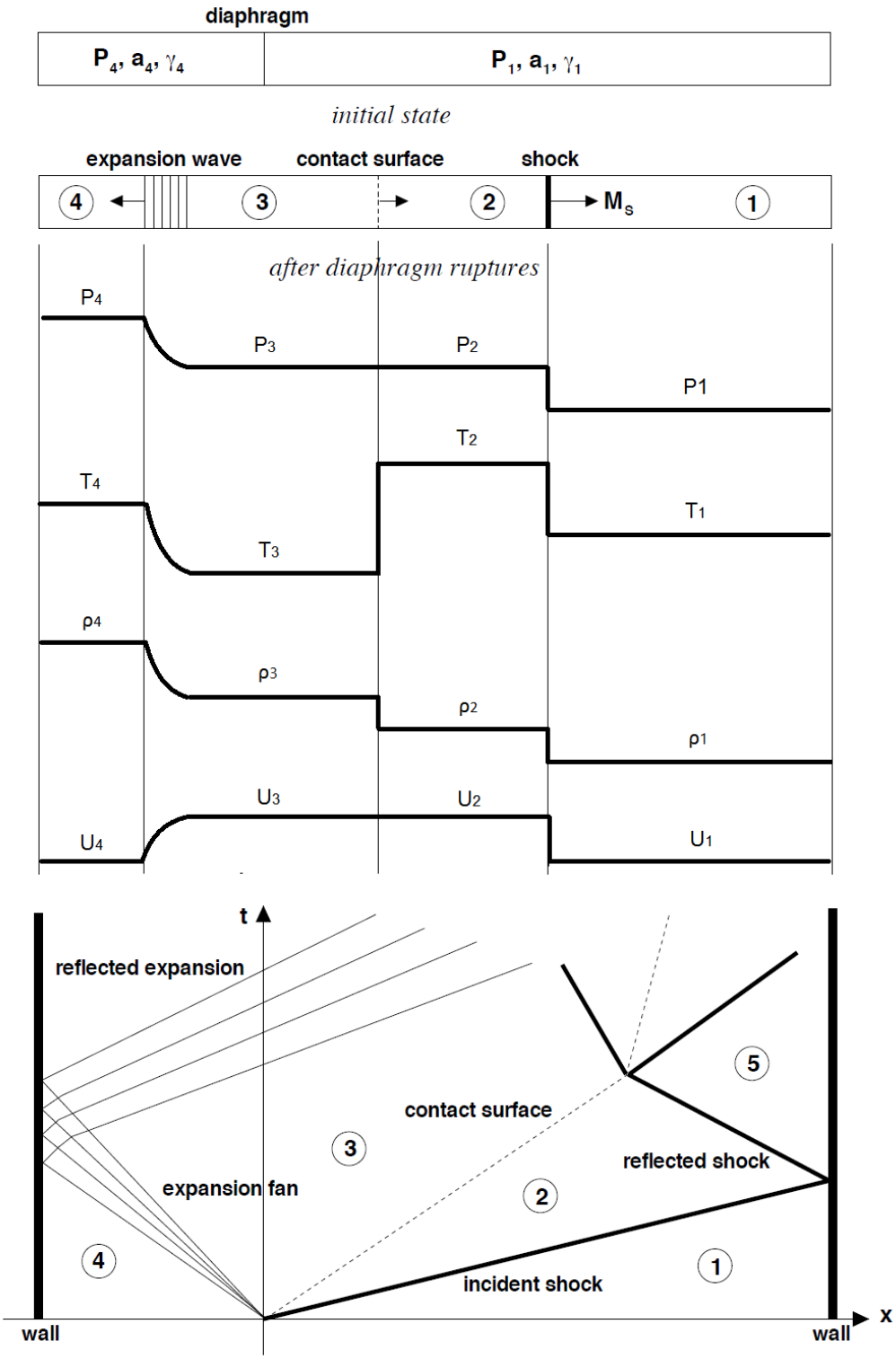

Fig. 3.9. Sequence of shock wave propagations in the shock tube experiment, and wave diagram [65]

3.4.2 Pressure Ratio Across Initial Shock Wave

P_2/P_1, the pressure ratio between zone 1 and zone 2 can be expressed as a function of the initial shock wave Mach number Ms, and the specific heat ratio of zone 1. If the two zones across the initial shock wave is illustrated as Figure 3.10, the gas velocity behind the initial shock wave, u_2, which is in a stationary coordinate, can be expressed as u_2' in a coordinate moving with the shock. In this moving coordinate, the gas velocity ahead of the shock is u_s, and the shock wave is stationary. Therefore, the three conservation laws, mass, momentum, and energy across the initial shock wave are as follows:

$$\rho_1 u_s = \rho_2 u_2' \tag{3.3}$$

$$P_1 + \rho_1 u_s^2 = P_2 + \rho_2 u_2'^2 \tag{3.4}$$

$$h_1 + \frac{u_s^2}{2} = h_2 + \frac{u_2'^2}{2} \tag{3.5}$$

Note that subscripts 1 and 2 in equations represent the states of zone 1 and zone 2, respectively. If the gas is regarded as ideal gas, and Mach numbers of the gas in front of and behind the shock are defined as $M_2 = \frac{u_2'}{a_2}$ and $M_s = \frac{u_s}{a_1}$, respectively, Eq. 3.3 will be:

$$\frac{T_2}{T_1} = (\frac{P_2}{P_1})^2 (\frac{M_2}{M_s})^2 \tag{3.6}$$

where, $M = u/a$. If the process is isentropic, $a^2 = \gamma RT$ can be applied, so,

$$\rho u^2 = \frac{P}{RT}(Ma)^2 = \frac{P}{RT} M^2 \gamma RT = \gamma P M^2 \tag{3.7}$$

Eq. 3.4 can be changed to:

$$\frac{P_2}{P_1} = \frac{1 + \gamma M_s^2}{1 + \gamma M_2^2} \tag{3.8}$$

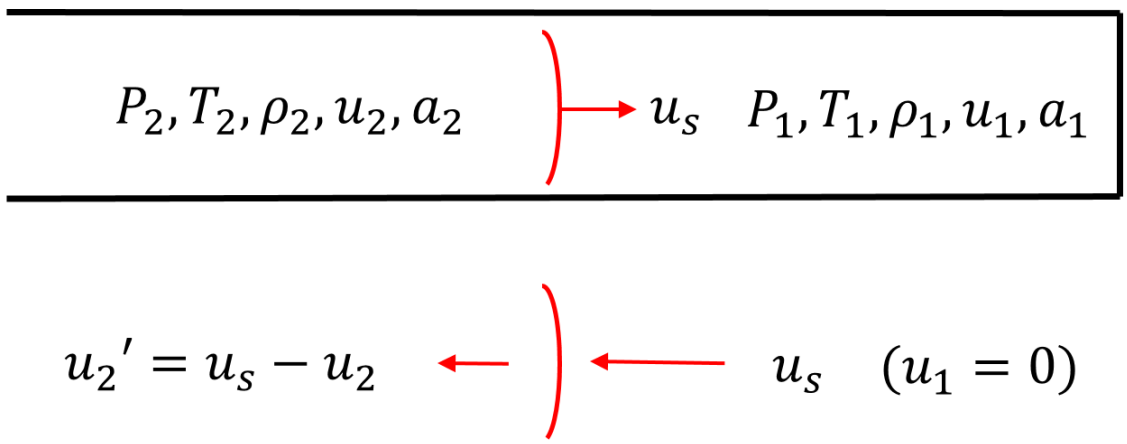

Fig. 3.10. Properties of two zones across the initial shock wave

Since it is ideal gas, $h = \frac{P}{\rho} + e = C_pT = \frac{\gamma}{\gamma-1}RT$ is also available, and then Eq. 3.5 will be:

$$\frac{T_2}{T_1} = \frac{1 + \frac{\gamma-1}{2}M_s^2}{1 + \frac{\gamma-1}{2}M_2^2} \tag{3.9}$$

Combining Eq. (3.6), (3.8) and (3.9) yields,

$$M_2^2 = (1 + \frac{\gamma-1}{2}M_s^2)/(\gamma M_s^2\frac{\gamma-1}{2}) \tag{3.10}$$

Substituting Eq. (3.10) into Eq. (3.8), we obtain,

$$\frac{P_2}{P_1} = 1 + \frac{2\gamma}{\gamma+1}(M_s^2 - 1) \tag{3.11}$$

The pressure ratio across the shock wave in Eq. (3.11) is called the shock strength, and it shows that the faster a shock wave propagates, the more pressure increases behind the shock wave.

3.4.3 Pressure Ratio of P_5 to P_1

The pressure transducer installed on the end wall of the main chamber, PT2, is able to measure pressure P_1 before the initial shock wave reaches the end wall and pressure P_5 after the shock is reflected by the end wall. In order to evaluate the measured pressure ratio of P_5 to P_1, a theoretical model regarding the pressure ratio is required. When the initial shock wave reaches a flat end wall of the main chamber, the shock wave is reflected, and the gas behind the shock remains rest, but all properties of the gas are changed to the state of zone 5 in Figure 3.9. Now, the reflected shock wave propagates at the speed of u'_R in the stationary coordinate, but in the coordinate moving with the shock, the gas velocities in front of and behind the shock are u_R, and u_2, respectively as shown in Figure 3.11.

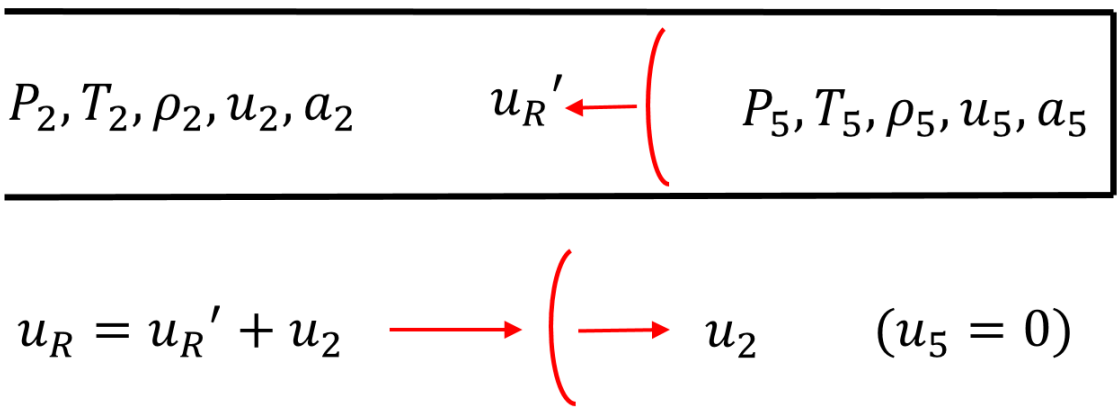

Fig. 3.11. Properties of two zones across the reflected shock wave

Mach number of the gas in front of the reflected shock wave can be defined as $M_R = u_R/a_2$. Finding the pressure ratio across the reflected shock wave begins with the velocity condition that the gas velocity behind the reflected shock wave, u_5 is identical to u_2 in the moving coordinate.

$$u_2 = u_5 \tag{3.12}$$

This can be expressed as,

$$\frac{u_2}{a_1} = \frac{u_5}{a_2} \cdot \frac{a_2}{a_1} \tag{3.13}$$

The left term u_2/a_1 is a function of γ in zone 1 and P_2/P_1 [68].

$$\frac{u_2}{a_1} = \{\frac{P_2}{P_1} - 1\}/\{\gamma\sqrt{\frac{\gamma-1}{2\gamma} \cdot (\frac{\gamma+1}{\gamma-1} \cdot \frac{P_2}{P_1} + 1)}\} \tag{3.14}$$

u_5/a_2 in the right term also can be expressed in a same manner.

$$\frac{u_5}{a_2} = \{\frac{P_5}{P_2} - 1\}/\{\gamma\sqrt{\frac{\gamma-1}{2\gamma} \cdot (\frac{\gamma+1}{\gamma-1} \cdot \frac{P_5}{P_2} + 1)}\} \tag{3.15}$$

The sound speed ratio a_2/a_1 is also a function of γ in zone 1 and P_2/P_1 [68].

$$\frac{a_2}{a_1} = \sqrt{\{\frac{P_2}{P_1}(\frac{\gamma+1}{\gamma-1} + \frac{P_2}{P_1})\}/\{1 + \frac{\gamma+1}{\gamma-1} + \frac{P_2}{P_1}\}} \tag{3.16}$$

Substituting Eq. (3.14), (3.15), and (3.16) into (3.13),

$$\frac{\frac{P_2}{P_1} - 1}{\gamma\sqrt{\frac{\gamma-1}{2\gamma} \cdot (\frac{\gamma+1}{\gamma-1} \cdot \frac{P_2}{P_1} + 1)}} = \frac{\frac{P_5}{P_2} - 1}{\gamma\sqrt{\frac{\gamma-1}{2\gamma} \cdot (\frac{\gamma+1}{\gamma-1} \cdot \frac{P_5}{P_2} + 1)}} \cdot \sqrt{\frac{\frac{P_2}{P_1}(\frac{\gamma+1}{\gamma-1} + \frac{P_2}{P_1})}{1 + \frac{\gamma+1}{\gamma-1} + \frac{P_2}{P_1}}} \tag{3.17}$$

Simplifying Eq. (3.17), we obtain Eq. (3.18) [68].

$$\frac{P_5}{P_1} = 1 + \frac{4\gamma}{\gamma+1}(M_s^2 - 1) \cdot \frac{1 + (\frac{1}{2} + \frac{\gamma-1}{\gamma+1}) \cdot (M_s^2 - 1)}{1 + (\frac{\gamma-1}{\gamma+1}) \cdot (M_s^2 - 1)} \tag{3.18}$$

Another way to find P_5/P_1 is using Eq. (3.11), which is available to figure out any pressure ratio across a normal shock wave. P_2 and P_5 are the pressures in front

of and behind the reflected shock wave, and the gas velocity in front of the reflected shock wave is M_R, which can be expressed as a function of M_s and γ of zone 1 [69].

$$\frac{P_5}{P_2} = 1 + \frac{2\gamma}{\gamma+1}(M_R^2 - 1) \tag{3.19}$$

$$M_R = \sqrt{\frac{2\gamma M_2^2 - (\gamma - 1)}{(\gamma - 1)M_s^2 + 2}} \tag{3.20}$$

Therefore, P_5/P_1 can be obtained in a simpler way,

$$\frac{P_5}{P_1} = \frac{P_5}{P_2} \cdot \frac{P_2}{P_1} = \{1 + \frac{2\gamma}{\gamma+1}(M_R^2 - 1)\} \cdot \{1 + \frac{2\gamma}{\gamma+1}(M_s^2 - 1)\} \tag{3.21}$$

Eq. (3.18) and (3.21) show identical results for same input variables.

3.4.4 Attenuation of Pressure Ratio of Reflected Shock Wave

The reflected pressure P_5 data is collected from the pressure record of PT2. Figure 3.12 shows an example of PT2 record. When the initial shock wave is reflected on the end wall, the pressure record displays a sudden pressure rise, and increases as a step shape due to shock waves travelling back and forth in the main chamber until the ignition, where the second big rise in the left graph occurs. The right graph in Figure 3.12 shows a zoomed version of the beginning of the PT2 record. The amplitude of P_5 which represents a gauge value of the reflected pressure, from the PT2 record is defined as a mean value of the first pressure step. The measured pressure ratio of P_5/P_1 will be the absolute pressure P_5 over room pressure of the day when the test is conducted.

In order to obtain the pressure ratio from Eq. (3.18), the specific heat ratio of zone 1 and Mach number of the initial shock should be obtained first. Ambient temperature and pressure are applied in the calculation. The specific heat ratio and gas constant of the mixture are calculated using mole numbers of hydrogen, methane, and air in the main chamber at ambient temperature, which are obtained by Eq. (2.16), (2.4), and (2.10), respectively. The Mach number of the initial shock is calculated using

the speed of sound, $a = \sqrt{\gamma_{mix} R_{mix} T}$, with the measured initial shock speed. Lastly, the pressure ratio P_5/P_1, a function of the specific heat ratio and the Mach number of the initial shock wave, can be determined by this calculation order. Figure 3.13 contains the comparison results of the measured and the calculated pressure ratios of P_5/P_1.

The black square dots represent the measured pressure ratios with respect to the Mach number of the initial shock wave, and the red line is the result of Eq. (3.18) for the given Mach number range. Both pressure ratios increase with the increase of the Mach number, but the measured pressure ratio is lower than the ratio from calculation. Further, the discrepancy between two ratios increases with the increase of the Mach number.

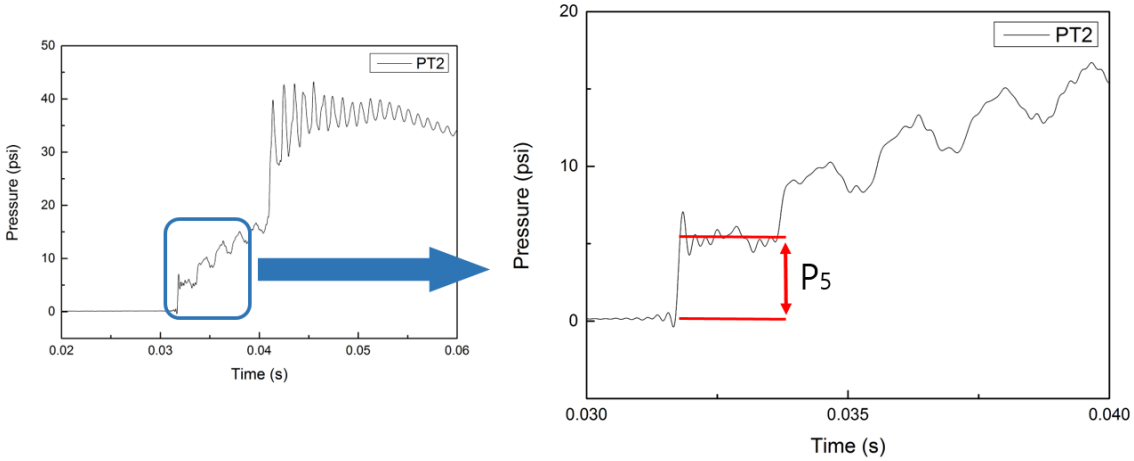

Fig. 3.12. Definition of the amplitude of the reflected shock wave obtained from PT2 pressure record, Original PT2 record (Left) and a zoomed version in the blue square (Right)

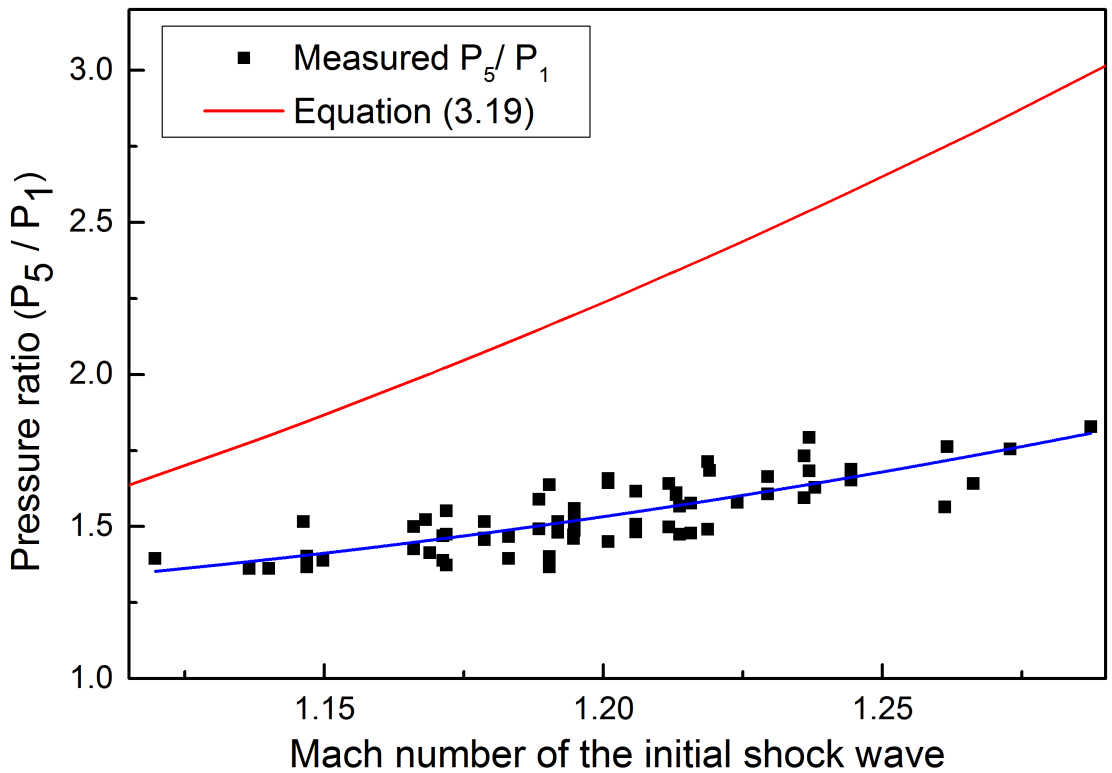

Fig. 3.13. Comparing the measured pressure ratio (black dots) and the calculated pressure ratio (red line)

There are two probable explanations that can be made on this result. The first one is the effect of rarefaction waves catching up the initial shock wave. In the ideal shock tube, the initial shock wave is sustained at a constant strength by a constant mass flow rate behind it, until the reflected waves occur. However, with the present experiment, the driver section is not a long tube, and the pressure it in immediately begins falling, thus reducing the mass flow rate into the driven section. This causes rarefaction waves to be propagated toward the initial shock. Expansion waves cannot be overlapped since pressure and temperature are decreased behind an expansion wave so the speed of the later expansion wave is slower than that of the former one. Nevertheless, the first expansion wave is able to catch up the initial shock wave due to the increased pressure and density behind the initial shock. In this case, the shock wave, an accumulation of compression waves, meets the expansion wave and they cancel each other out, decreasing the pressure gap across the initial shock wave and the shock strength. Sundaramurthy [70] varied the length of the driver section, which corresponds to the pre-chamber in the current study, to control the strength of the shock front. As shown in Figure 3.14, the first expansion fan can catch up the shock front quickly with the shorter driver section, C_1, than C_2 due to the shorter travel distance. The number of expansion waves catching up the shock front increases with the decrease of the length of the driver section, so the shock strength is the lowest at the shortest driver section. The author experimentally verified this fact that among four different length ratios of the driven section to the driver section, 5.65, 8.51, 17.21, and 101.97, the longest length ratio, 101.97, showed the lowest shock strength, and the shortest length ratio, 5.65, showed the highest shock strength. In the current study, the length ratio of the main chamber to the pre-chamber is 6.46, so it is assumed that some of expansion waves may catch up the initial shock wave before reflected on the end wall of the main chamber, and as a result, the strength of the initial shock wave becomes lower compared to the given shock Mach number and specific heat ratio, and the pressure ratio between P_5 and P_1 is also measured lower than the ideal pressure ratio.

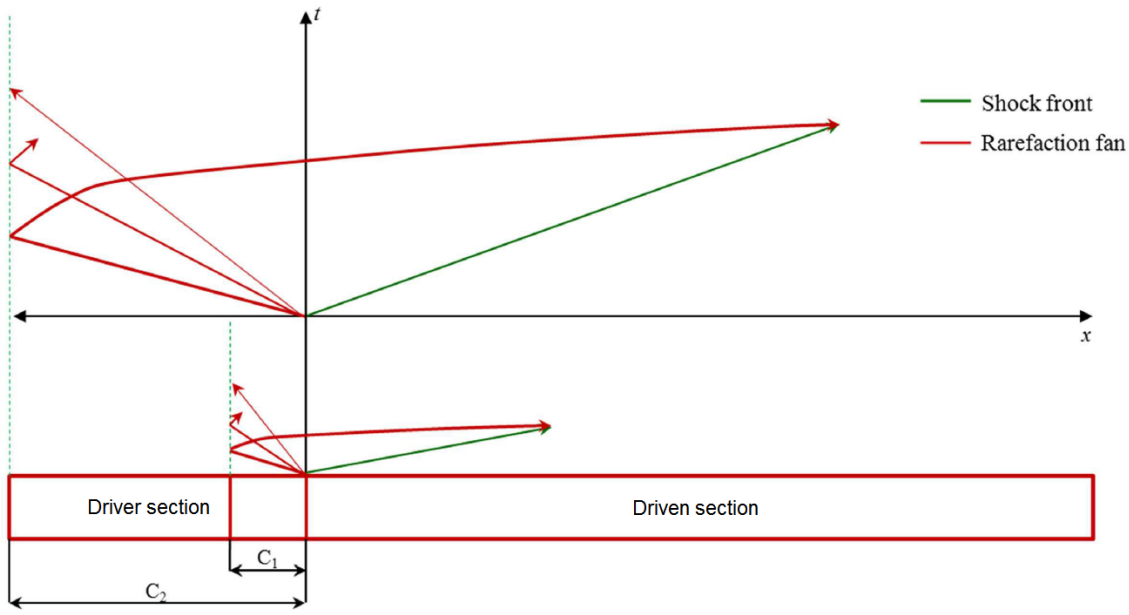

Fig. 3.14. x-t Diagram for the expansion fan and the initial shock wave behaviors after the diaphragm rupture, and a comparison between two driver length C_1, and C_2 [70]

The second reason of the attenuation of the measured pressure ratio is the effect of the wall boundary layer. According to Mirels [71], a flow with velocities u_2 in the region 2 of Figure 3.9 generates a thin boundary layer on the wall surface behind the initial shock wave. This boundary layer induces expansion waves in the region 2 due to a vertical velocity component in the layer, and the expansion waves overtake the shock front, attenuating its strength. Also, Mirels considered dissipation and heat transfer as other reasons of the shock attenuation. Dissipation and heat transfer from the wall to the boundary layer tend to increase the vertical velocity, contributing to the generation of expansion waves. Mirels compared the results of the theoretical model based on the above assumptions with the shock tube experiment results [72], and especially it showed good agreement at low Mach number of the shock wave. The experiment results show that the pressure ratio across the shock wave decreases with the increase of the distance from the diaphragm due to the attenuation of the shock strength, and with the increase of the shock Mach number at the same distance from the diaphragm. This trend also agrees with the result in Figure 3.13.

As the increase of the shock strength results in the increase of pressure and temperature of a gas mixture behind the shock wave, mitigation of the attenuation effects on the shock strength may contribute to the reduction of the ignition delay time. Considering that the advantages of the shock wave are utilized in channels of the actual wave rotor drum, further investigations on the attenuation of the shock strength in a constant-volume chamber are required.

3.5 Ignition Delay Time Measurement

Finding factors leading to rapid ignition is crucial for the wave rotor combustor due to its intrinsic operational requirements. Some of variables which may affect the ignition delay time of the current combustion setup will be discussed. In the current study, the definition of the ignition delay time is from when the diaphragm ruptures, emerging of hot-radical jet, to when the ignition of the air/fuel mixture in the main

chamber occurs as illustrated in Figure 3.15. A black line and a red line in the figure indicate pressure records of the pre-chamber and PT2, respectively. While pressure in the pre-chamber is increasing, the diaphragm ruptures at a certain pressure, and this rupture moment can be estimated via the method mentioned in Section 3.3. The pressure record of PT2 has two sudden pressure rise, the first one is due to the arrival of the initial shock wave at the end wall and the later one is due to ignition in the main chamber.

Perera [17] and Chinnathambi [44] had the same definition of the ignition delay time, but the measurement method was different to the current way. Unlike the ignition moment that can be detected using both the high speed camera and the pressure record, the rupture moment cannot be directly measured unless the high speed camera stays focus on the diaphragm. So, they individually obtained the diaphragm rupture time and the ignition moment. They first repeated several diaphragm rupture tests at each pre-chamber combustion condition while the high speed camera was recording images of the diaphragm alone, and then, average diaphragm rupture times of each condition were calculated from the obtained high speed camera data. The ignition moment of the main chamber was measured separately in another run using a different high speed camera setup, and then applied the average rupture times to the calculation of the ignition delay time. In the old method, because of the uncertainties of the equivalence ratio of the pre-chamber and the depth of the diaphragm indentation, errors of the averaged rupture time is too high especially for the short ignition delay time cases. In the Perera′s result, the standard deviation of the averaged rupture time is 0.2 ms, which is 50% of the shortest ignition delay time, 0.4 ms, of the ethylene combustion in the main chamber. In the Chinnatahmbi′s result, the standard deviation of the averaged rupture time is 0.3 ms, which is also 50% of the shortest ignition delay time, 0.6 ms, of the ethylene combustion in the main chamber. Therefore, the old method, which measures the diaphragm rupture moment and the ignition moment separately and applies the average rupture time to the calculation of the ignition delay time may include considerable measurement errors especially for

the short ignition delay time cases. In the current study, it has been confirmed that the diaphragm rupture moment can be estimated using the data of the initial shock speed within error of 0.5% to the measured rupture moment using the high-speed camera, and therefore more precise data of the ignition delay time can be suggested. Above all, both the diaphragm rupture moment and the ignition moment are acquired in the same combustion test, eliminating undesirable errors of the previous researches.

Ignition delay time can be expressed as follows.

$$\tau_{ig} = \tau_{PT1\,peak} - \tau_{rupture} \tag{3.22}$$

τ_{ig} is the ignition delay time, $\tau_{PT1\,peak}$ is the ignition moment in the main chamber, and $\tau_{rupture}$ is the diaphragm rupture moment. The time origin of both the ignition moment and the rupture time is when the spark plug is first triggered by the ignition switch. When the ignition takes place in the main chamber, rapid chemical reactions increase temperature and pressure locally, and the pressure change is delivered to the pressure transducer as a form of pressure waves after some time delay. The ignition moment is defined as the peak time of the first differential of the second pressure rise of PT1 pressure profile as shown in Figure 3.16. Since the ignition point varies with each combustion test case, the travelling time of the pressure waves from the ignition point to the pressure transducer PT2 also changes, so this remains as the measurement error. To assess the measurement error of the ignition moment, the ignition moment is measured by the high-speed camera as time-resolved flame luminosity images as Figure 3.17. Due to a fast shutter speed, the gamma value should be maximized to recognize the ignition moment. These ignition moments obtained by the flame luminosity images and the pressure record are compared. Figure 3.18 shows the comparison result of the ignition moments from the high-speed camera and the pressure records. Generally, the ignition moments measured by PT1 are a bit slower than those measured by the camera due to the delay time of the pressure wave movement, and the mean error is 0.018%, so this method to measure the ignition moment using the pressure profile from PT1 is credible.

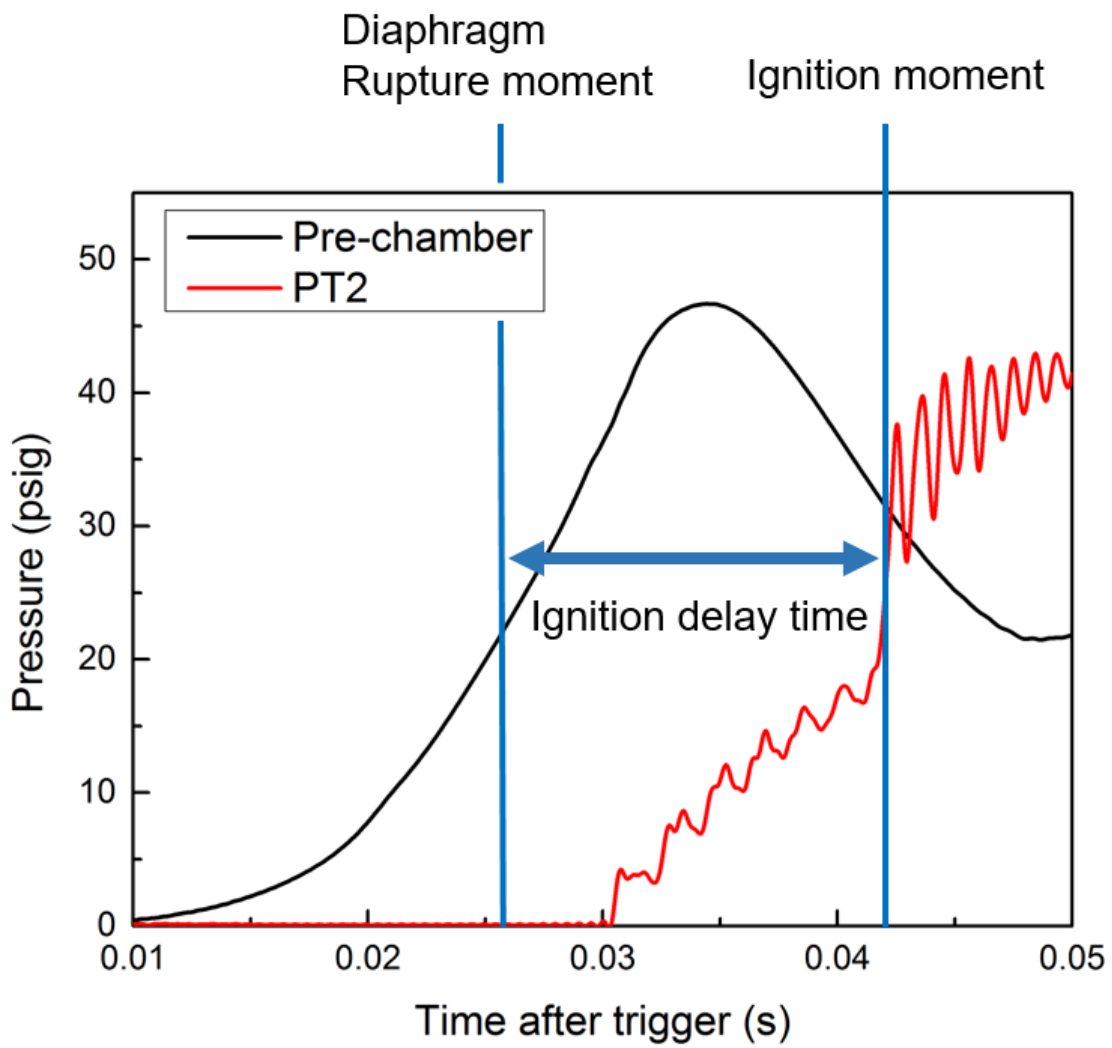

Fig. 3.15. Definition of the ignition delay time

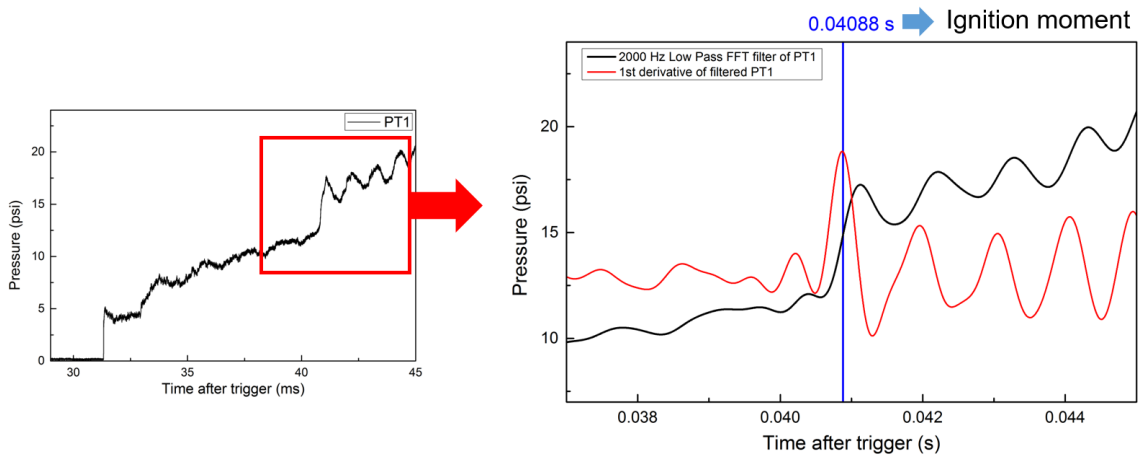

Fig. 3.16. Definition of the ignition moment obtained from PT1 pressure record. Original PT1 pressure record (Left) and a zoomed version in the red square (Right). The blue vertical line indicates the ignition moment in the left figure (Main chamber condition: Φ=0.8, H_2=50%, indentation #=2, case #=2)

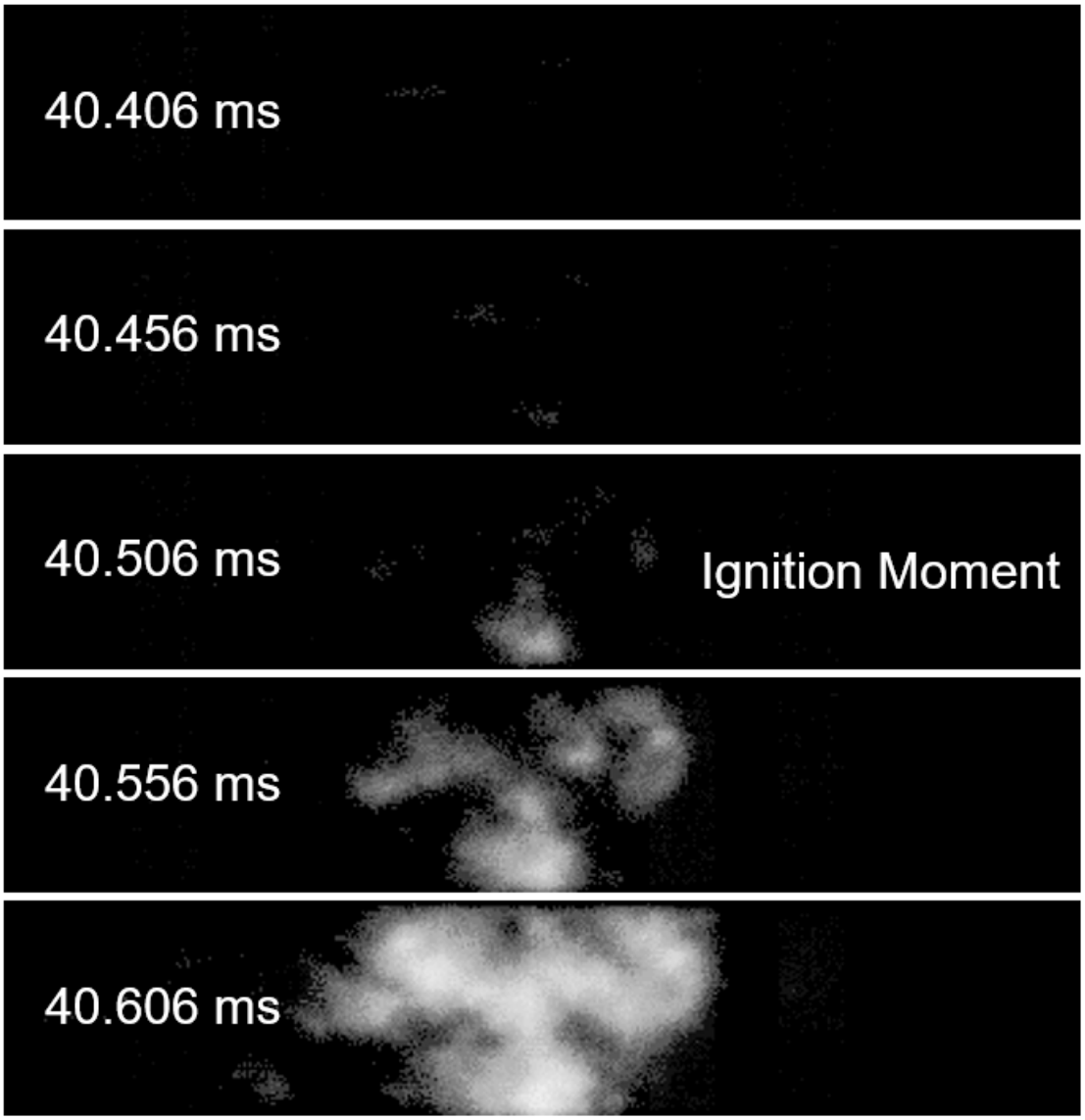

Fig. 3.17. Time-resolved flame luminosity images obtained by the high-speed camera for the validation of the ignition moment (Main chamber condition: Φ=0.8, H_2=50%, indentation #=2, case #=2)

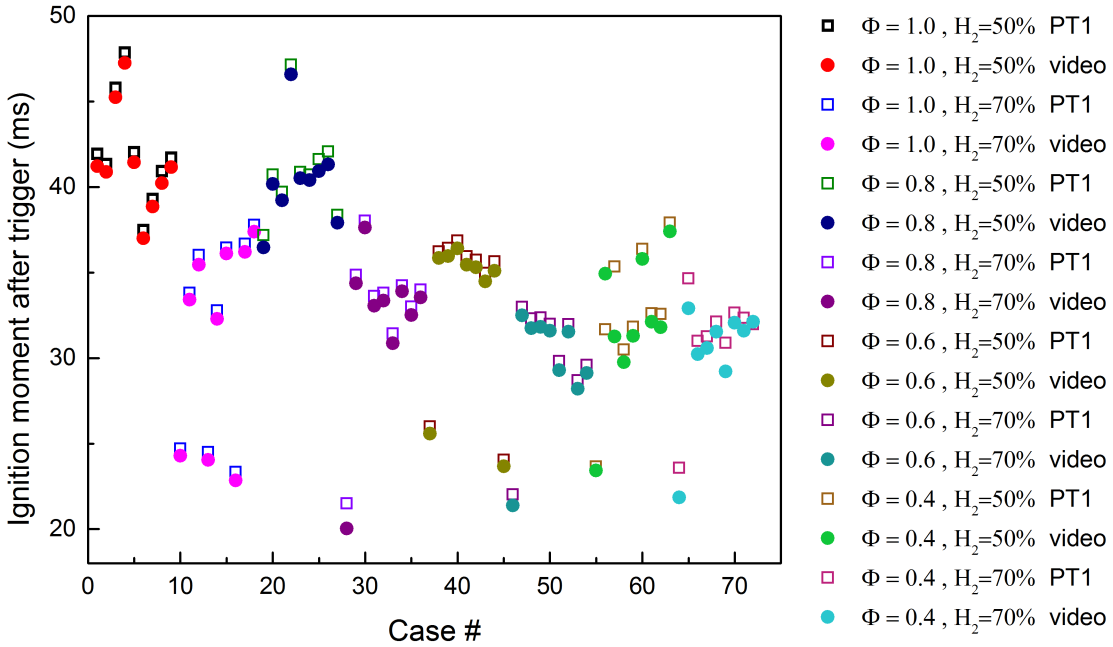

Fig. 3.18. Comparing the ignition moments obtained by PT1 pressure records and the high-speed camera

3.5.1 Effect of Diaphragm Rupture Pressure on Ignition Delay Time

The results of the ignition delay time with respect to the experimental variables, equivalence ratios from 0.4 to 1.0, hydrogen contents in the fuel mixture 50% and 70%, and various rupture pressures are shown in Figure 3.19. For the investigations of the ignition delay time through the shock tube experiments, the ignition temperature and pressure in the driver section can be readily tracked. However, for the current setup, it is challenging because the ignition is occurred by hot jet from the pre-chamber, and pressure and temperature of the air/fuel mixture are changed by several traversing shock waves before ignited. Therefore, the diaphragm rupture pressure has been selected as a variable which has a strong influence on the ignition delay time. The rupture pressure is normalized by the initial pressure in the main chamber, which is ambient pressure.

Ignition delay time decreases with the increase of the rupture pressure, and there are two reasons for this trend. First, the higher rupture pressure, the more the mass flow rate of the hot radical jet injected through the nozzle. Ignition gets promoted when the air/fuel mixture is exposed to more hot reactive radicals. Nazmuzzaman [45] conducted the 3-D numerical simulation research to investigate the ignition delay time with respect to two hydrogen contents of the methane and hydrogen mixture, 50% and 70%, and 3 different pre-chamber rupture pressures. Figure 3.20 shows the 3-D numerical simulation result using a detailed mechanism with 21 species and 84 elementary reactions (DRM19) at the same boundary condition and pre-chamber combustion condition [45]. At 0.8 ms, the length of the penetration jet increases with the increase of the pre-chamber pressure, and it seems that ignitions are occurred at 1 ms, 1.4 ms, and 2.2 ms for the pre-chamber pressure 6 bar, 4 bar, and 2 bar cases, respectively. For the hydrogen content 70%, the ignition delay time decreases with the increase of the pre-chamber pressure, which is similar to the current result, but for the hydrogen content 50%, ignition was observed at the case of pre-chamber pressure 2 bar alone, and the other cases did not show ignition within 3 ms after the

diaphragm rupture due to the simulation time limit. Obtaining the fastest ignition at the lowest rupture pressure is opposite to the current result that the ignition delay time decreases with the increase of the rupture pressure for the hydrogen content 50% as well. The author explained this phenomenon with turbulent mixing effects. The higher the rupture pressure, the more the mixing occurs by the jet turbulence, so the physical ignition delay time reduces. For the high reactive fuel mixture, which is the hydrogen content 70% case, the ignition delay time obviously decreases with the increase of the mixing effect. On the contrary, for the less reactive fuel mixture (hydrogen content 50% case), hot mass from the jet is rapidly mixed with cold mass of fuel mixture in the main chamber if the mixing effect is too strong. Therefore, the flame kernel dissipates, and the ignition becomes difficult to achieve. Unlike the simulation result, the turbulent effect of the jet is not considerably dominant in the main chamber considering that the ignition delay time still decreases with the increase of the rupture pressure, so the mixing effect helps reduce the ignition delay time. In addition, as the pre-chamber combustion condition is the constant-volume combustion, higher pressure leads to the product gas of higher temperature, so it is assumed that temperature of hot jet increases with the increase of the rupture pressure. If a system for measuring temperature of hot-jet is prepared, better analysis on the effect of the rupture pressure can be available.

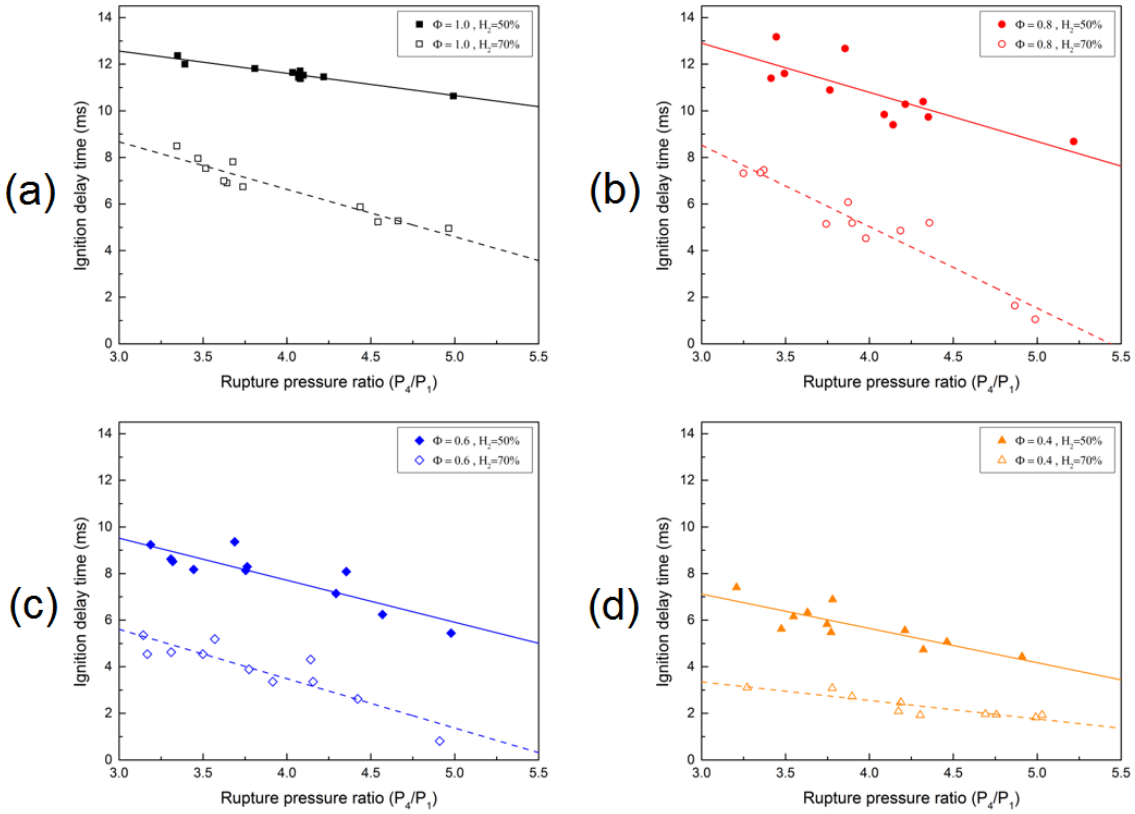

Fig. 3.19. Ignition delay time variation with respect to the rupture pressure change (Black: Φ=1.0, Red: Φ=0.8, Blue: Φ=0.6, Yellow: Φ=0.4, Solid line: H_2=50%, Dotted line: H_2=70%)

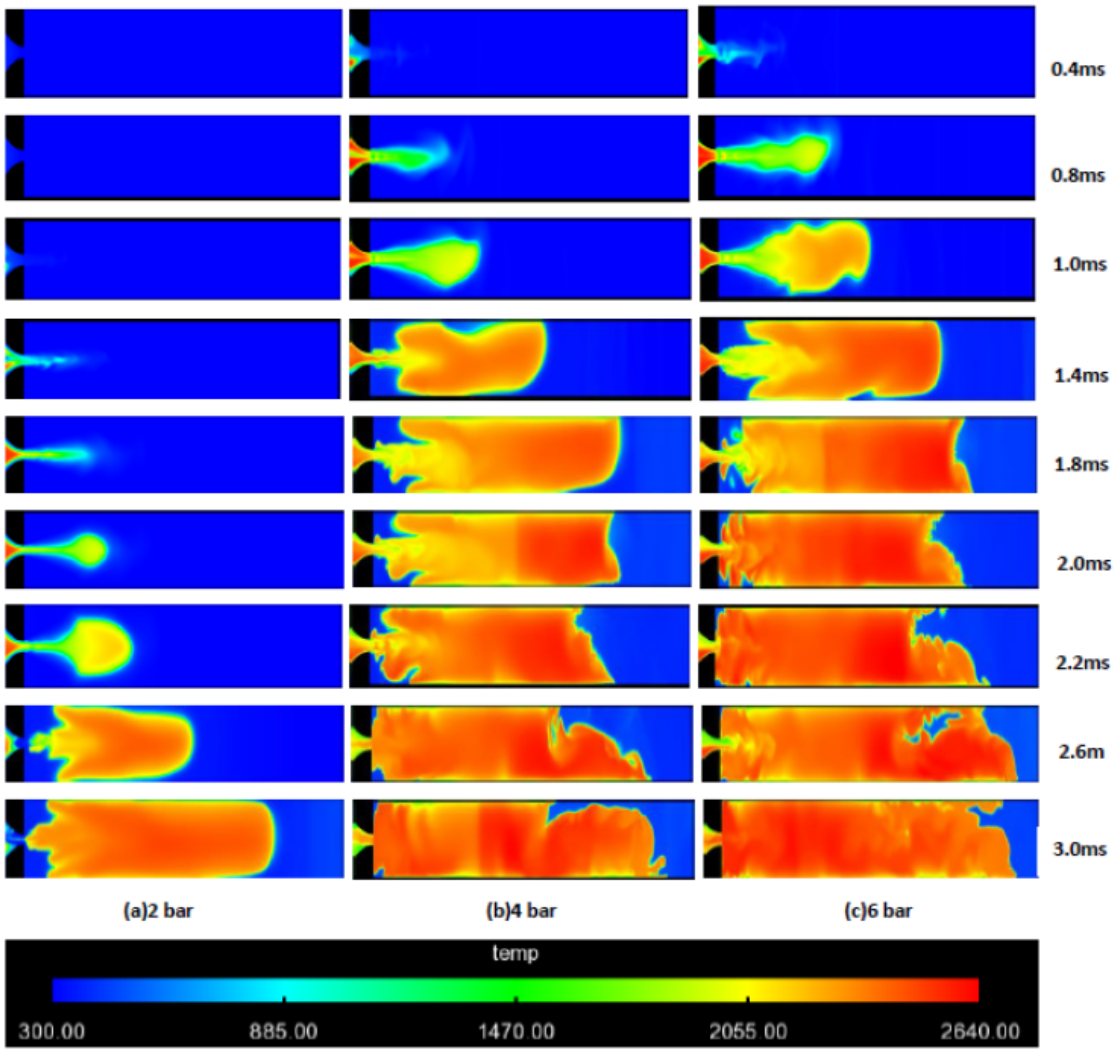

Fig. 3.20. Time-resolved temperature distribution in CVC chamber for hydrogen-methane-air mixture Φ=1.0, and H_2=70% with respect to the pre-chamber rupture pressure variation (a)2 bar, (b)4 bar and (c)6 bar [45]

It can also be inferred from Fig 3.19 that the strength of the traversing shock wave increases with the increase of the rupture pressure, increasing temperature and pressure of the air/fuel mixture in the main chamber. Figure 3.21 shows that the initial shock Mach number increases with the increase of the rupture pressure for the experiment cases of the current study, and it can be also confirmed from Figure 3.5 and Eq. (3.1). Eq. (3.11) describes that the shock strength increases with the shock Mach number, and therefore the higher the rupture pressure, the higher the shock strength. As the shock strength indicates the pressure ratio across the shock, higher shock strength implies higher pressure behind the shock, and temperature behind the shock T_2 also increases with the increase of Ms with respect to the shock front properties P_1, T_1, and specific heat ratio γ as shown in Eq. (3.23) [73].

$$\frac{T_2}{T_1} = \frac{\{2\gamma M_s^2 - (\gamma - 1)\} \cdot \{(\gamma - 1)M_s^2 + 2\}}{(\gamma + 1)^2 M_s^2} \tag{3.23}$$

Shock waves travelling in the main chamber are reflected on the end wall, or transmitted by other waves, increasing temperature and pressure of the air/fuel mixture. It can be expected that temperature and pressure of the mixture exposed to the shock waves will increases more when the rupture pressure increases. NASA report [73] expressed the ignition delay time as follows.

$$\tau_{ig} \propto \frac{1}{A} exp(\frac{E}{RT}[O]^{-a}[Fuel]^{-b}P^{-c}T^{-d}) \tag{3.24}$$

A is the Arrhenius constant, E is the global activation energy, R is the universal gas constant, [O] is the oxygen concentration, and a, b, c and d are real positive numbers. Since the correlation indicates that the inverse of pressure and temperature is proportional to the ignition delay time, the increase of pressure and temperature reduces the ignition delay time. This fact is verified by many other researches performed the shock tube experiments using hydrogen-methane mixtures, but it is reported that the increase or decrease range of the ignition delay time varies with the hydrogen content in the mixture [35, 74–77].

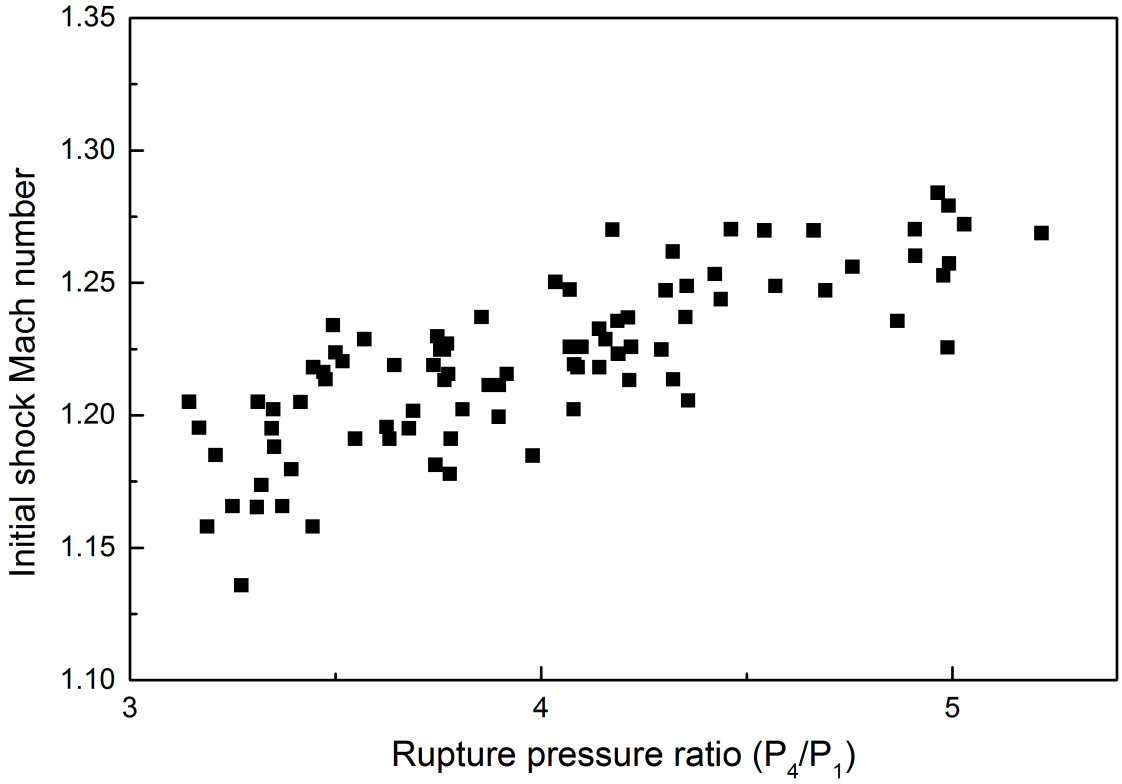

Fig. 3.21. Mach number variation of the initial shock wave with respect to the rupture pressure change for all test cases

3.5.2 Effect of Hydrogen Content in Fuel Mixture on Ignition Delay Time

Two different hydrogen contents for the hydrogen-methane mixture has been tested, 50% and 70%. In Figure 3.19, the hydrogen content 70% shows noticeably faster ignition delay times compared to the hydrogen content 50%. This observation is also verified in [45]. In general, hydrogen is much more reactive than methane, so the increase of the hydrogen content in the mixture decreases the ignition delay time with respect to the same equivalence ratio and ignition energy. Cheng and Oppenhiem [78] investigated ignition characteristics of hydrogen-methane mixtures and proposed an empirical correlation with the ignition delay time of hydrogen and methane, $\tau_{ig} = \tau_{CH_4}^{(1-\chi_{H_2})}\tau_{H_2}^{(\chi_{H_2})}$, indicating that the ignition delay time is a function of the hydrogen content in the mixture. Zhang [35] and Petersen [79] conducted shock tube experiments to investigate the ignition delay time of the hydrogen-methane mixture with various hydrogen volumetric contents. Zhang classified the ignition characteristics of the hydrogen-methane mixture into three ignition regimes based on hydrogen contents. For the hydrogen volume content in the fuel mixture less than 40%, it is methane chemistry dominating ignition (MCDI), and the addition of hydrogen does not change dominant kinetic of the methane oxidation. In this regime, ignition kinetic depends on oxygen concentration in fuel mixtures, so the ignition delay time increases with the increase in equivalence ratio. For the hydrogen volume content higher than 80%, it is hydrogen chemistry dominating ignition (HCDI), and the ignition characteristics of the mixture behave analogously to 100% pure hydrogen ignition. The existence of methane acts like an ignition inhibitor in this regime [75]. The hydrogen volume content around 60% is called combined chemistry methane and hydrogen dominating ignition (CCMHDI), and the addition of hydrogen highly decreases the ignition delay time in this regime. According to Tang [75], the typical reaction occurring ignition is the chain-branching reaction, $H + O_2 \leftrightarrow OH + O$, and the most effective reaction inhibiting ignition is H radical consumption reaction $CH_4 + H \leftrightarrow CH_3 + H_2O$. As the hydrogen content increases, the amount of the H

radical increases, and on the other hand, the consumption of the H radical is reduced due to the decrease of the methane content, and therefore, the ignition delay time decreases. Gersen [74] reported that the ignition delay time significantly decreases with the increase of the hydrogen content from the hydrogen volume content more than 50%. Two hydrogen contents in the current study correspond to the CCMHDI regime, so it is assumed that the ignition delay times of two hydrogen content cases show obvious differences with respect to the equivalence ratios tested.

3.5.3 Effect of Equivalence Ratio on Ignition Delay Time

Four equivalence ratios, 0.4, 0.6, 0.8, and 1.0, are tested in the current study. Figure 3.22 is a rearranged version of Figure 3.19 to elucidate the effect of the equivalence ratio on the ignition delay time variation. For both hydrogen content cases, the ignition delay time decreases with the decrease of the equivalence ratio. It seems that oxygen concentration plays an important role in the chemical kinetics on ignition of hydrogen contents from 50% to 70%. Another noticeable trend in Figure 3.22 is that the ignition delay time at equivalence ratio 0.8 is more sensitive to the rupture pressure change for both hydrogen contents compared to the other equivalence ratios.

Interestingly, Zhang [35] conducted the ignition delay time investigation for equivalence ratios, 0.5, 1, and 2 at the fixed ignition pressure 1.8 MPa and hydrogen content 60%, and the result shows that ignition delay times have no difference between two equivalence ratios 0.5 and 1, as shown in Figure 3.23 (a), which is opposite to the current result. Gersen [74] also reported a similar result that two ignition delay times of equivalence ratios of 1 and 0.5 at the fixed ignition temperature 995±4 K and hydrogen content 50% shows no difference as well as shown in Figure 3.23 (b). As briefly introduced in Section 1.3.3, Zhang explained this phenomenon using sensitivity analysis that both ignition promotion and inhibition reactions are promoted together with the increase of equivalence ratio, making the ignition delay time insensitive to the equivalence ratio variation. However, the author did not suggest a

clear explanation on R1, $H + O_2 \leftrightarrow O + OH$, which still has the biggest promotion effect on ignition. Nazmuzzaman [45] investigated the chemical ignition delay time of the hydrogen-methane mixture for equivalence ratios from 0.6 to 1.0, and reported that equivalence ratio has minimal effect on the ignition delay time. In the current study, the ignition temperature and pressure are ambiguous, so it is impossible to make a direct comparison with previous researches. If it is assumed that the same rupture pressure causes the same thermochemistry profile of hot-radical jet and the same ignition temperature and pressure of the air/fuel mixture in the main chamber each time, it can be concluded that the radicals in hot-jet play a vital role in the ignition mechanism because the hot-jet ignition is a big difference with the previous researches regarding the ignition delay time. In order to deeply understand the effect of radicals in hot-jet, the quantitative analysis on the variation of radicals with respect to the rupture pressure change as well as the tracking of the temperature and pressure changes of combustion in the main chamber.

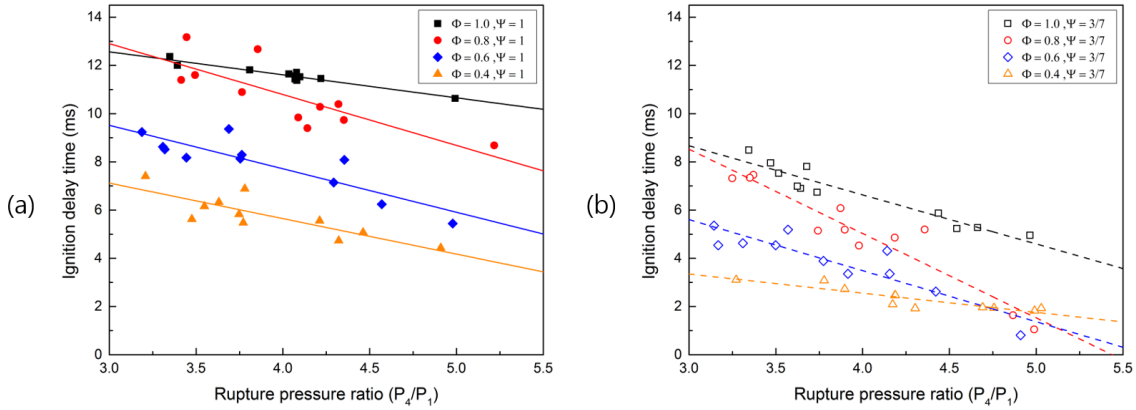

Fig. 3.22. Re-arranged version of the ignition delay time variation with respect to the rupture pressure change (Black : Φ=1.0, Red: Φ=0.8, Blue: Φ=0.6, Yellow: Φ=0.4, Solid line: H_2=50%, Dotted line: H_2=70%)

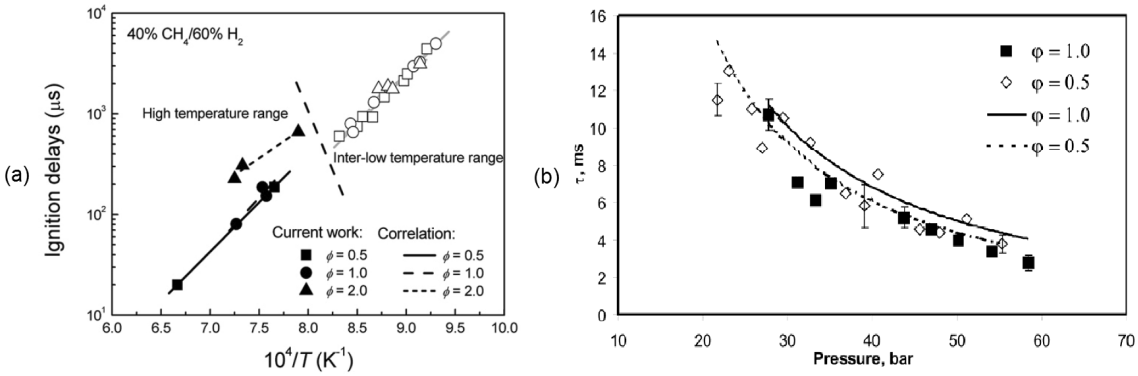

Fig. 3.23. Effects of equivalence ratio on ignition delay of hydrogen and methane dominating mixture for hydrogen content 60% (a) [35], and 50% (b) [74]

4. COMBUSTION CHARACTERISTICS AND SHOCK-WAVE INTERACTION

4.1 Maximum Pressure in Main Chamber after Ignition

For the same amount of fuel, combustion at higher temperature and pressure is more efficient in terms of useful energy production. Constant-volume combustion which can achieve both high temperature and pressure results in a thermodynamic cycle with higher efficiency than constant-pressure combustion. This is the ultimate goal of wave-rotor combustors. In an adiabatic constant-volume combustor, the final pressure with complete combustion does not depend on the details of the ignition or combustion process. The goal of the present work is to ensure rapid ignition and complete combustion. The pressure history in the combustor gives an indication of the ignition process and the initial rate of combustion. An investigation has been performed to find the maximum pressure produced in the main chamber by constant-volume combustion of hydrogen-methane-air mixtures with the equivalence ratio variation from 0.4 to 1.0 and the two fuel blends with hydrogen volume fractions of 50% and 70%. The averaged pressure values are presented in Figure 4.1, and the maximum pressure of combustion is defined by the highest pressure value of PT2 since the PT2 is flush mounted in the main chamber. The error bar on the graph indicates the standard deviation of each mean value. The 70% hydrogen blend show higher maximum pressures than the 50% blend, even though the theoretical adiabatic maximum pressure is higher for the 50% blend, as shown below. This is a clear indication that the maximum pressure is strongly related to the dynamics of ignition and heat loss. At equivalence ratio 0.8, the highest maximum pressure is observed for both fuel blends. The lowest maximum pressure is measured at equivalence ratio 0.4, with relatively small difference between the two blends compared to other equivalence ratio conditions.

In order to explain this trend, the flame temperature and pressure of the adiabatic constant-volume combustion, and the reaction rate of hydrogen-methane-air mixtures regarding respective equivalence ratios and hydrogen contents should be considered. Figure 4.2 shows flame temperature and pressure of the adiabatic constant-volume combustion obtained by CEA NASA code [80]. The adiabatic flame temperature and pressure reach its peak at equivalence ratio 1.1, indicating that the equivalence ratio 1.1 is the most energetic condition for the hydrogen-methane-air mixture. Dirrenberger [81] examined the variation of the laminar flame velocity with respect to the changes of the equivalence ratio and the hydrogen content of the hydrogen-methane-air mixture as shown in Figure 4.3 using a flat flame adiabatic burner, and the laminar flame velocity, which represents the reaction rate, is also the fastest at equivalence ratio 1.1 for the entire hydrogen contents. The flame velocity significantly declines as the equivalence ratio decreases, and therefore, the equivalence ratio 0.4, is an adverse condition for rapid combustion.

It is noted that the maximum recorded pressure in Figure 4.1 shows the peak value at equivalence ratio 0.8, which differs with the adiabatic pressure and the laminar flame velocity trends. The peak pressure in the CVC chamber is expected to be determined by the balance between pressure rise by combustion and pressure loss by heat loss. It appears that the rate of combustion is influenced by other factors than laminar flame velocity. Although the main chamber pressure overrides the pre-chamber pressure when ignition occurs, the remaining radicals can have an influence on combustion for a short time. As the ignition delay time decreases with a decrease of the equivalence ratio in Figure 3.22, which conflicts with previous results, the radicals engage in the combustion reaction of the main chamber, so the most energetic condition is shifted from equivalence ratio 1.1 to 0.8.

It is also noted that the maximum pressure values between two hydrogen contents at the same equivalence ratio display a significant gap except for the equivalence ratio 0.4, which is a contrast to the adiabatic constant-volume combustion pressure result. Unlike the adiabatic combustion, heat from combustion is transferred through the

chamber wall. The 70% hydrogen blend cases have a higher reaction rate, so the pressure can be built up more within a certain time period than the 50% hydrogen blend cases while losing heat. Considering that the laminar flame velocity has a relatively small difference with respect to the hydrogen content variation at a low equivalence ratio, the reason of that the maximum pressure gap between two hydrogen contents at equivalence ratio 0.4 is small can be explained by the low reaction rate. In other words, the reaction rate cannot be increased a lot at a low equivalence ratio with an increase of the hydrogen content. Karimi [82] conducted the 2-D simulation research on the effect of jet chemical activity. Three different compositions of jet were tested; products of rich combustion (equivalence ratio 1.1) of ethylene and air, pure nitrogen, and pure argon. The jet of combustion products displays a faster radical increase of CH_3 and higher molar concentrations of CO, H, and OH radicals than other two jets, and therefore, it shows the fastest fuel consumption rate. In conclusion, the radicals from the hot-jet play a vital role on both the ignition delay time and the combustion process at the beginning, so it is necessary to measure the amount of the radical injection in order to quantitatively analyze the effect of the radicals on the ignition and the combustion.

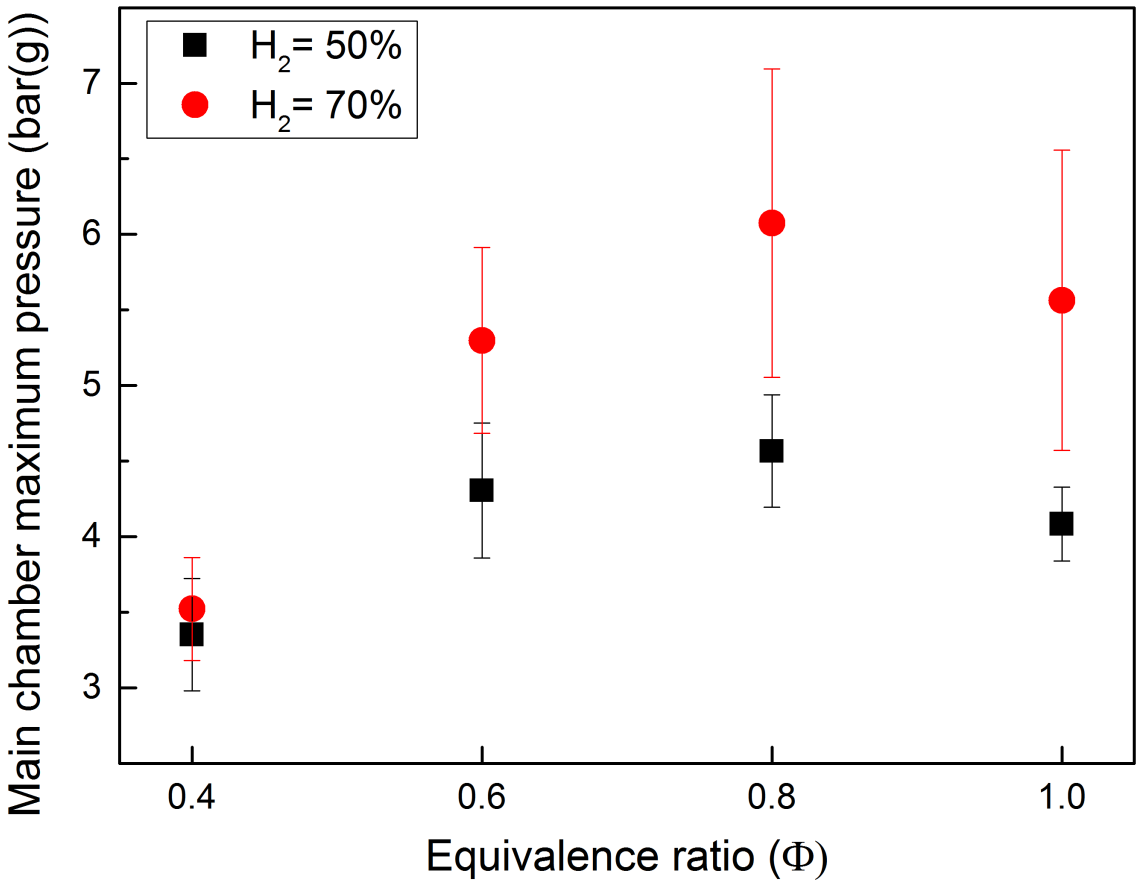

Fig. 4.1. Maximum pressure of hydrogen-methane-air mixture combustion pressure in the main chamber for all test cases

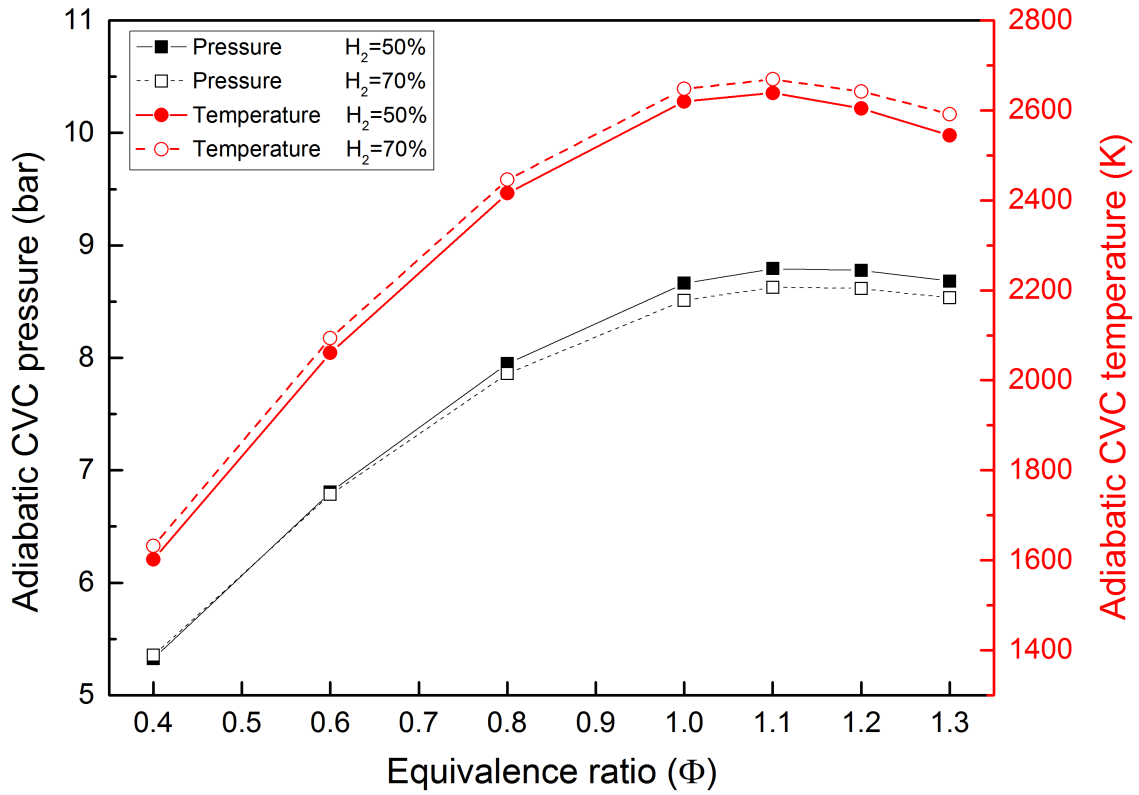

Fig. 4.2. Adiabatic constant-volume combustion pressure and temperature for the experiment conditions obtained using the CEA NASA code

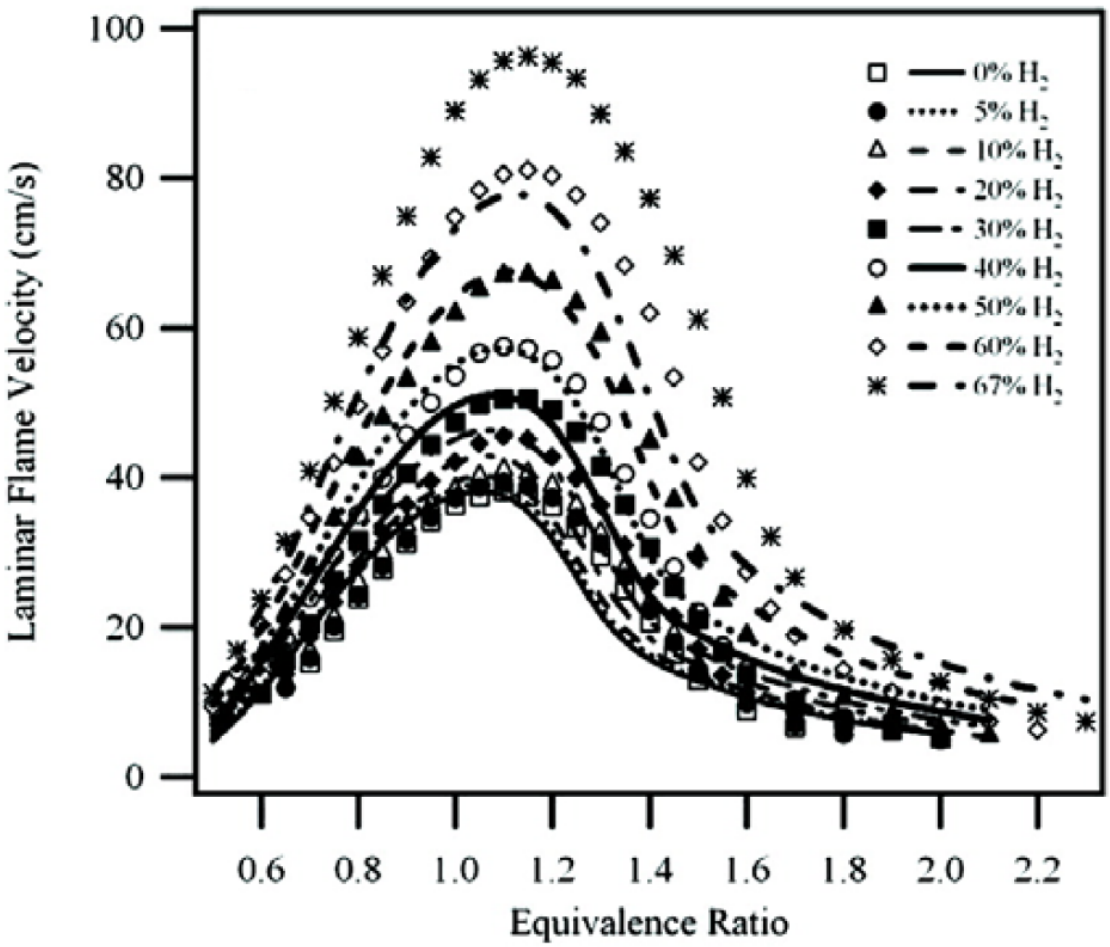

Fig. 4.3. Laminar burning velocities for a hydrogen-methane-air mixture as a function of equivalence ratio and hydrogen content. Symbols, experiments; lines, modeling [81]

4.2 Flame Motion and Interaction due to Pressure Waves

High-speed Schlieren images of each test case display that the flame front has an apparent back-and-forth motion, due to gas motion caused by the traveling shock and expansion waves. Shock-flame interactions have a different character depending on whether the shock arrives from the hot (fast sound speed) or cold (slow sound speed) side of the flame. There are called slow-fast and fast-slow interactions [83–85]. Each test case has a distinct difference in shock-flame interactions and pressure profiles.

4.2.1 Flame Front Motion by Pressure Waves

After ignition occurs, the flame propagates in the main chamber, consuming the unburned air/fuel mixture. Because of shock and expansion waves generated by the initial jet and by the ignition event, this flame is subject to bulk motion set up by waves travelling in the main chamber.

4.2.2 Shock-Flame Interaction

The interactions of shock and flame are generally categorized into two classes: slow-fast (s/f) and fast-slow(f/s) interactions. The terms, slow and fast refer to the sound speed in the gas where the shock is travelling. In the slow-fast interaction, the incident shock wave travels from the low sound speed medium, the cold unburned gas, to the high sound speed medium, the hot combusted product gas. When the incident shock wave meets the flame front, it is separated as transmitted and reflected waves. In the slow-fast interaction, the transmitted wave is a shock wave, and the reflected wave is an expansion fan. On the contrary, in the fast-slow interaction, the incident shock travels from the hot product gas to the cold reactant gas, and both the transmitted wave and reflected wave are both shocks. These explanations are well depicted in Figure 4.4.

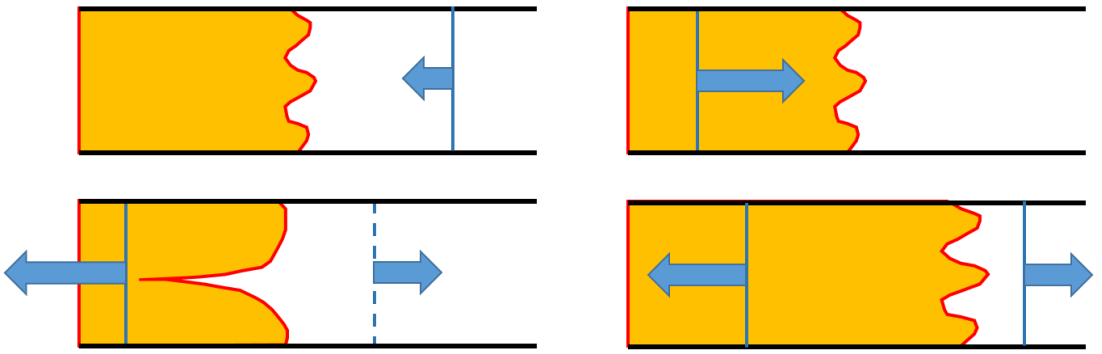

(a) Slow-Fast shock flame interaction (b) Fast-Slow shock flame interaction

Fig. 4.4. Illustration of slow-fast and fast-slow interactions

Two shock-flame interactions have different effects on the heat release rate, the entropy reduction, and the pressure increase. When a shock wave passes through a flame front, it leads to the gas compression and the flame stretch concurrently. For the fast-slow interaction, the effect of the flame stretch overrides that of the gas compression, the heat release rate increases more than the slow-fast interaction [86]. Compared to the isobaric combustion process, a single shock-flame interaction causes the entropy reduction and the pressure increase. These are also more effective in the fast-slow interaction [87].

The fundamentals of flame deformation induced by the shock-flame interaction are well known. The Richtmyer-Meshkov instability (RMI) is mainly involved with the flame surface deformation under the shock-flame interaction environment [88]. Like the Rayleigh-Taylor instability (RTI), the fundamental mechanism of Richtmyer-Meshkov instability is baroclinic vorticity generation caused by the misalignment of the local pressure gradients and the local density gradients across the interface [88]. Unlike RTI, the pressure gradient is transient and due to traveling waves. Richtmyer suggests an equation for the growth rate of perturbation amplitude ε as [88]:

$$\frac{d\varepsilon(t)}{dt} = \dot{\varepsilon} = k \cdot \Delta u \cdot At \cdot \varepsilon_0 \tag{4.1}$$

Where, ε is the length of the interface perturbation, k=$2\pi/\lambda$ is the wave number of the perturbation, λ is the channel width, At = $(\rho_2\text{-}\rho_1)/(\rho_2+\rho_1)$ is the post-shcok Atwood number, Δu is the interface velocity change due to shock refraction, and ε_0 is the initial perturbation amplitude. Figure 4.5 illustrates the evolution of the Richtmyer-Meshkov instability at a single-mode interface perturbation [89].

The flame stretch or deformation can extend the flame surface by the shock-flame interaction, increasing the consuming rate of reactants in the chamber [45]. In continuous-flow constant-pressure combustors the positive feedback of such interactions leads to undesirable oscillations. However, it is desirable and exploited in the wave rotor combustor since it helps achieve the rapid combustion. The shock-flame interaction can influence the combustion characteristics of other types of combus-

tors. For example, a pulse detonation engine, which is a typical system using the shock-flame interaction for rapid combustion, exploits a deflagration-to-detonation transition(DDT) process. A deflagration initiated by a weak energy source such as a small spark can accelerate due to turbulence and shock interations, with the reaction zone of the flame merging into a supersonic detonation front [90].

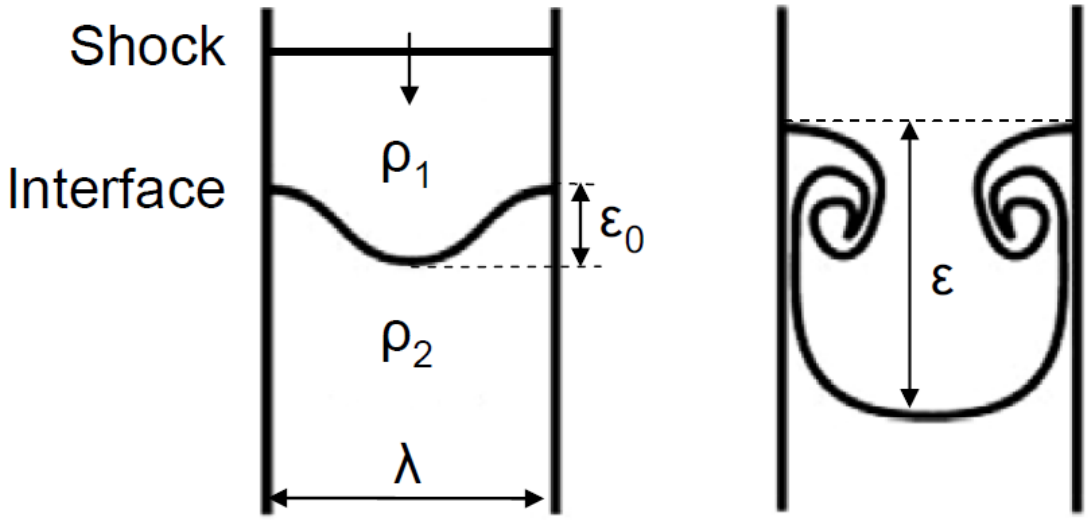

Fig. 4.5. Evolution of RMI at a single-mode interface perturbation [89]

4.2.3 Observations of Flame Behavior and Shock-Wave Interactions

The propagation of the flame front is investigated using a high-speed Schlieren technique. Figure 4.6 shows that time-resolved Schlieren images of two cases, (a) Φ=1.0 and H_2=50%, and (b) Φ=0.6 and H_2=70%. The time period of oscillation images is selected when the maximum pressure by combustion is observed. The flame front is moved and modified due to the shock-flame interaction in both cases, but behaviors of each case are considerably different. Since images of both cases display one period of the gas oscillation, each cases contains a fast-slow interaction and a slow-fast interaction. For the case (a), the weak flame stretch and flame surface compression effects by the shock-flame interaction are observed, and many vortices formed by the baroclinic effect are behind the flame surface. The period of the flame movement is measured as 1 ms approximately. On the other hand, the case (b) displays the strong flame stretch and flame surface compression effects. The first image of (b) shows a tulip shape flame by the slow-fast interaction, and the flame front is rapidly stretched after 21.62 ms due to the fast-slow interaction. At 22.15 ms, the flame front gets shrunk again like the image of 21.36 ms due to the slow-fast interaction.

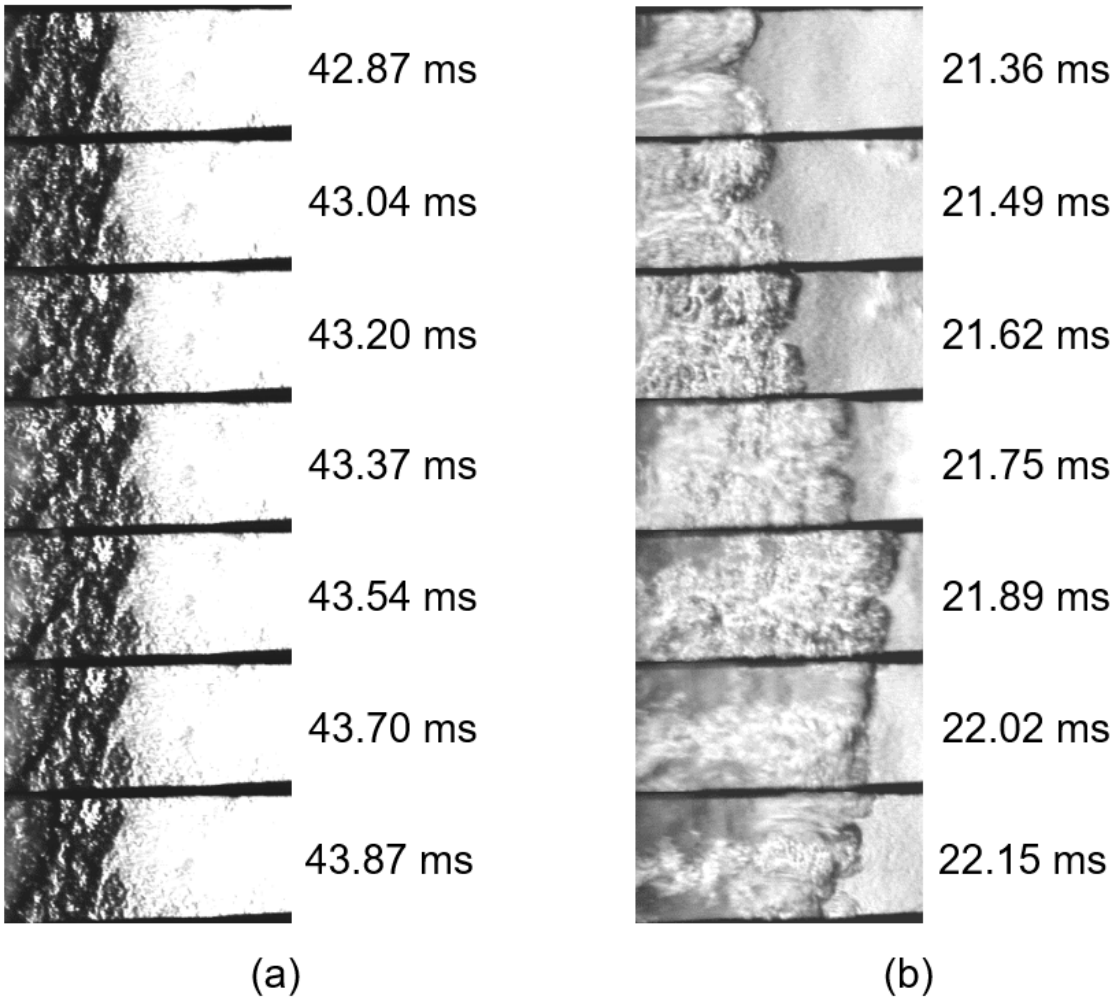

Fig. 4.6. Time-resolved Schlieren images of (a) Φ=1.0 and H_2=50%, and (b) Φ=0.6 and H_2=70%. The numbers beside each image indicate the time after trigger

Pressure records of the cases (a) and (b) in Figure 4.7 also exhibit the differences corresponding to the flame movements. Red vertical lines in Figure 4.7 indicate the time period of each image series in Figure 4.6. Both pressure-time graphs have the same time scale. The ignition in case (b) occurs much earlier as expected due to the greater role of fast hydrogen kinetics. The more energetic ignition event also results in larger pressure amplitude than the case (a). Despite the lower total fuel energy in the chamber at the lower equivalence ratio of case (b), the fast energy release helps overcome heat losses. In Figure 4.7 (a), after 28.57 ms, when the initial shock wave arrives at the end wall, the pressure increases oscillating with a certain frequency due to the shock waves bouncing back and forth, and then quickly rises due to ignition at 38.27 ms. After the ignition occurs, the pressure gradually decreases oscillating with a higher frequency compared to the frequency before ignition. For the case (b) in Figure 4.7, the initial shock arrives at the end wall at 18.41 ms, and the ignition occurs at 20.34 ms before the shock wave comes back to the end wall. The pressure increase by ignition is significantly larger than the case (a), and the amplitude and the frequency of the pressure oscillation after ignition are also larger and higher. The combustion behavior in the main chamber can be characterized as slow flame propagation like the case (a) and fast flame propagation like the case (b) based on the pressure oscillation frequency 1000 Hz and the combustion time 20 ms. Table 4.1 shows the classified combustion characteristics for all test conditions.

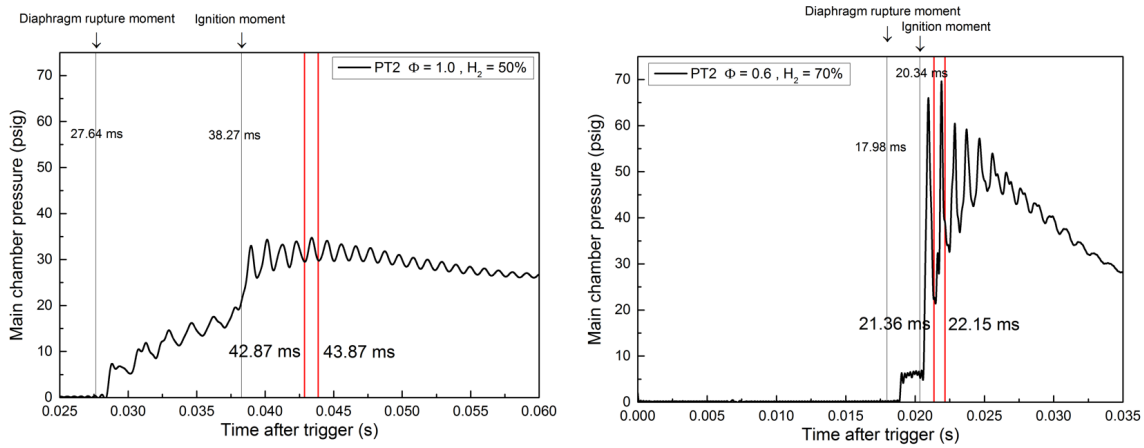

Fig. 4.7. Pressure records in the main chamber obtained by PT2 for the test conditions of (a) Φ=1.0 and H_2=50%, and (b) Φ=0.6 and H_2=70%

Table 4.1
Classification of combustion characteristics for all test conditions

Fast flame propagation				Slow flame propagation			
Φ	H_2 (%)	τ_{comb} (ms)	Frequency (Hz)	Φ	H_2 (%)	τ_{comb} (ms)	Frequency (Hz)
1	70	2.78	1050	1	50	33.74	976
0.8	70	3.63	1135	0.6	50	27.10	953
0.8	50	7.95	1069	0.4	70	47.71	867
0.6	70	9.39	1008	0.4	50	40.02	908

The fast flame propagation results in energetic flame front deformations by the shock-flame interaction, and the higher amplitude and frequency of the pressure oscillation. Considering that four test conditions of the fast flame propagation have faster laminar flame velocities than other conditions of slow flame propagation, one interpretation can be suggested that a feedback mechanism between the flame and the pressure waves can lead to the flame acceleration, achieving the fast flame propagation [89, 91]. When the shock waves pass through the flame front, the interaction not only expands the combustion products, but also generates other pressure waves. These waves coalesce and form a single one-dimensional wave within a very short distance after the interaction, increasing the strength of the shock wave [92]. The reinforced shock compresses and accelerates the unburned gas ahead of the flame, thus temperature, pressure and vorticity of the unburned gas are increased, and this increases the reaction rate of the flame. Consequently, the expansion rate of the gas products is enhanced more, generating a stronger shock wave. This feedback loop is illustrated in Figure 4.8.

For a higher reaction rate of the reactants, this feedback mechanism explains the fast flame propagation. However, it seems that the feedback mechanism has a minor influence on a lower reaction rate of the reactants. Although the traveling shock wave is enhanced by the shock-flame interaction, the expansion rate of the product gas is not increased further due to the low reaction rate of the reactant gas, maintaining the flame propagation speed. In order to exploit the feedback effect to accelerate the flame propagation speed, the reactant gas mixture should satisfy a certain reaction rate condition. Since the reaction rate of the reactants varies with the mixture conditions and the mixing conditions, it is recommended that future investigation to find the minimum criteria yielding the feedback effect should be conducted in controlling not only the equivalence ratio and fuel ratio but also the shock strength.

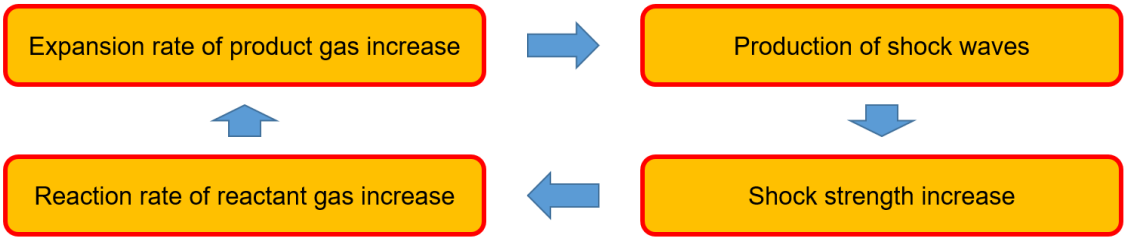

Fig. 4.8. Feedback mechanism enhancing the flame acceleration

4.2.4 Flame Front Oscillation by Shock-Flame Interactions

A methodology was introduced in Section 2.7 to define the flame front axial location and quantify the the flame front movement along the chamber axis over time. This methodology is applied for all Schlieren test cases and the flame position movement is compared with the corresponding pressure record. Among them, results of cases Φ=1.0 and H_2=50% for (a) and (c), and Φ=0.6 and H_2=70% for (b) and (d) are presented in Figure 4.9. In order to compare both cases intuitively, the flame front movement-pressure-time graph of two cases are presented as the zoomed-out version (a) and (b), and the zoomed-in version (c) and (d). The scales of flame movement, pressure, and time in each version are identical. The distance of the end wall from the nozzle, which is 40.77 cm, is the top line of the graph. The flame front movement expressed as a red line displays a similar trend with the pressure result, a black line.

Both cases show that a periodic flame front movement is in phase with a pressure oscillation. In Figure 4.9 (a), the condition of Φ=1.0 and H_2=50% shows that the amplitude of the flame oscillation is about 1cm at the beginning of combustion. It is observed that the flame front cannot propagate more to the end wall at 48 ms after trigger, and even retreats at 52 ms. The flame front moves forward after the shock strength dissipates at 55 ms. This lagged flame movement results from the low reaction rate of reactants in that the flame front cannot overcome the compression effect of the shock wave due to slow consumption rate of the unburned gas. On the contrary, the condition of Φ=1.0 and H_2=50% in Figure 4.9 (b) shows the flame oscillation amplitude of approximately 3cm at the beginning of combustion, 3 times larger than the condition of Φ=1.0 and H_2=50%. The flame front reaches the end wall within three periods as shown in Figure 4.9 (d) The feedback effect appears well in this case that the product gas is expanded by the traveling shock wave, increasing the heat release rate. With the shock wave enhancement by the pressure wave generation from the flame surface, the traveling speed of the shock increases due to the increase of pressure and temperature. This leads to the increase of frequencies of the pressure and the flame oscillations, resulting in the fast flame propagation.

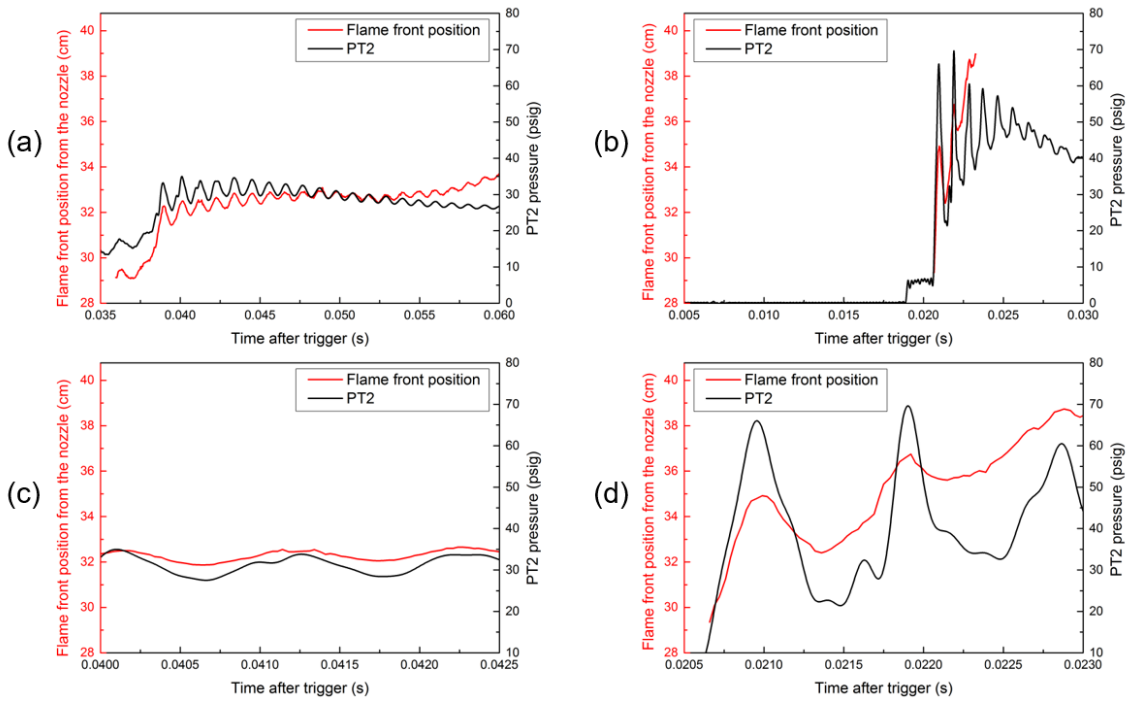

Fig. 4.9. Comparison of flame front movement and pressure oscillation. (a) Φ=1.0 and H_2=50% and (b) Φ=0.6 and H_2=70% are the zoomed-out version, and (c) Φ=1.0 and H_2=50% and (d) Φ=0.6 and H_2=70% are the zoomed-in version

4.2.5 Comparison of Gas Motion and Pressure Oscillation Frequencies

Pressure oscillation frequencies before and after ignition, and the gas oscillation frequency (as measured by the flame location) are compared in Figure 4.10. All frequencies are obtained by the fast Fourier transform (FFT) from the pressure and the flame movement records. The black point is the averaged pressure frequency before ignition, the red point is the averaged pressure frequency after ignition, and the green point is the flame oscillation frequency. The pressure frequency after ignition is slightly higher than the gas oscillation frequency, reflecting the faster travel of waves in higher temperature gas. The flame front movement is driven by the traveling shock wave and tracks the post-ignition pressure frequency within the margin of error. The fast flame propagation conditions, which have pressure oscillation frequencies higher than 1000 Hz, exhibit the flame acceleration. Oscillation frequencies of the pressure and the flame front are highly related to the reaction rate of the air/fuel mixture because the equivalence ratio 0.8, which has the highest reaction rate, shows the highest oscillation frequencies of the pressure and the flame front in the hydrogen contents of both 50% and 70%, and the hydrogen content 70% shows higher frequencies than the 50%. The pressure frequency before ignition displays no notable change with respect to the variations of the equivalence ratio and the hydrogen content, but it changes significantly after ignition. Therefore, this can be an evidence of that the shock wave is affected by the flame, supporting the feedback mechanism between the flame and the shock wave.

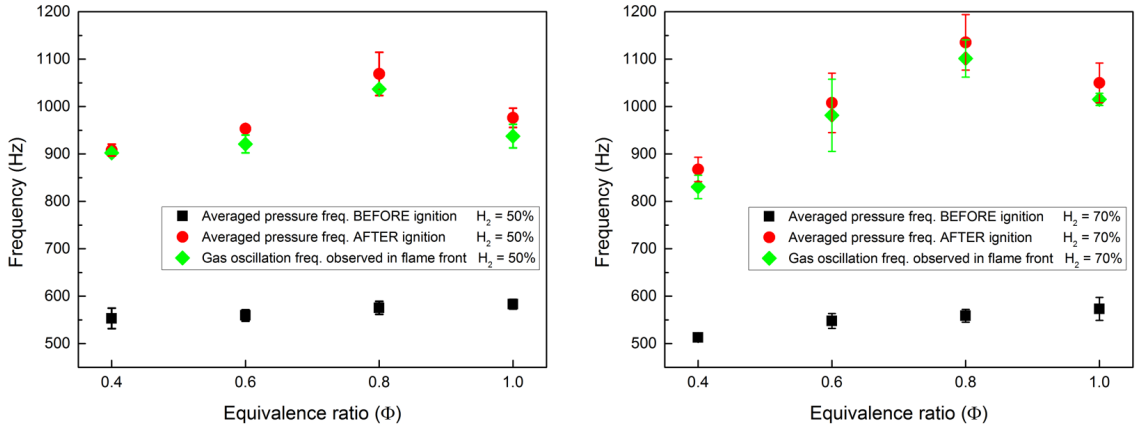

Fig. 4.10. Comparison of gas oscillation frequencies of the pressure before and after ignition, and the flame front. Left : H_2=50%, Right : H_2=70%

4.3 Combustion Time Measurement

Combustion time is defined as a time interval from the ignition moment to the time when the flame front arrives at the end wall of the main chamber, so the combustion time represents a time to burn up the air/fuel mixture in the chamber. Figure 4.11 shows the combustion time variation regarding the equivalence ratio and the hydrogen content. The black point is the hydrogen content 50%, and the red point is the 70%. The combustion behavior is classified as fast and slow flame propagation based on the combustion time 20 ms. For the fast flame propagation, the combustion time shorter than 20 ms, the flame is accelerated by the interaction, reaching the end wall within a very short time. The shortest combustion time, 2.565 ms, is observed at Φ=1.0 and H_2=70%. For the slow flame propagation, the combustion time longer than 20 ms, the flame cannot be accelerated, so the flame front oscillates and propagates with a slow speed. The longest combustion time, 48.757 ms, is observed at Φ=1.0 and H_2=70%. If the reaction rate of the reactants is high enough, the feedback mechanism between the flame and the shock wave is activated, and the flame propagation is accelerated, reducing the combustion time. In Figure 4.11, it is expected that the condition for the feedback activation is located between 50% and 70% of the hydrogen contents at equivalence ratio 1.0 and 0.8. As the feedback mechanism is influenced by the reactivity of the reactants and the mixing effect of the shock wave, Properties of the shock wave such as a pressure ratio across the shock and the shock Mach number should be obtained to analyze the mixing effect on the feedback mechanism. If the gas mixture with a low reaction rate is supplied into the wave rotor channel, the mixture may not be completely consumed until exhausted, causing an adverse effect on the system efficiency. Therefore, it is imperative to find the activation condition of the feedback mechanism for achieving the fast flame propagation.

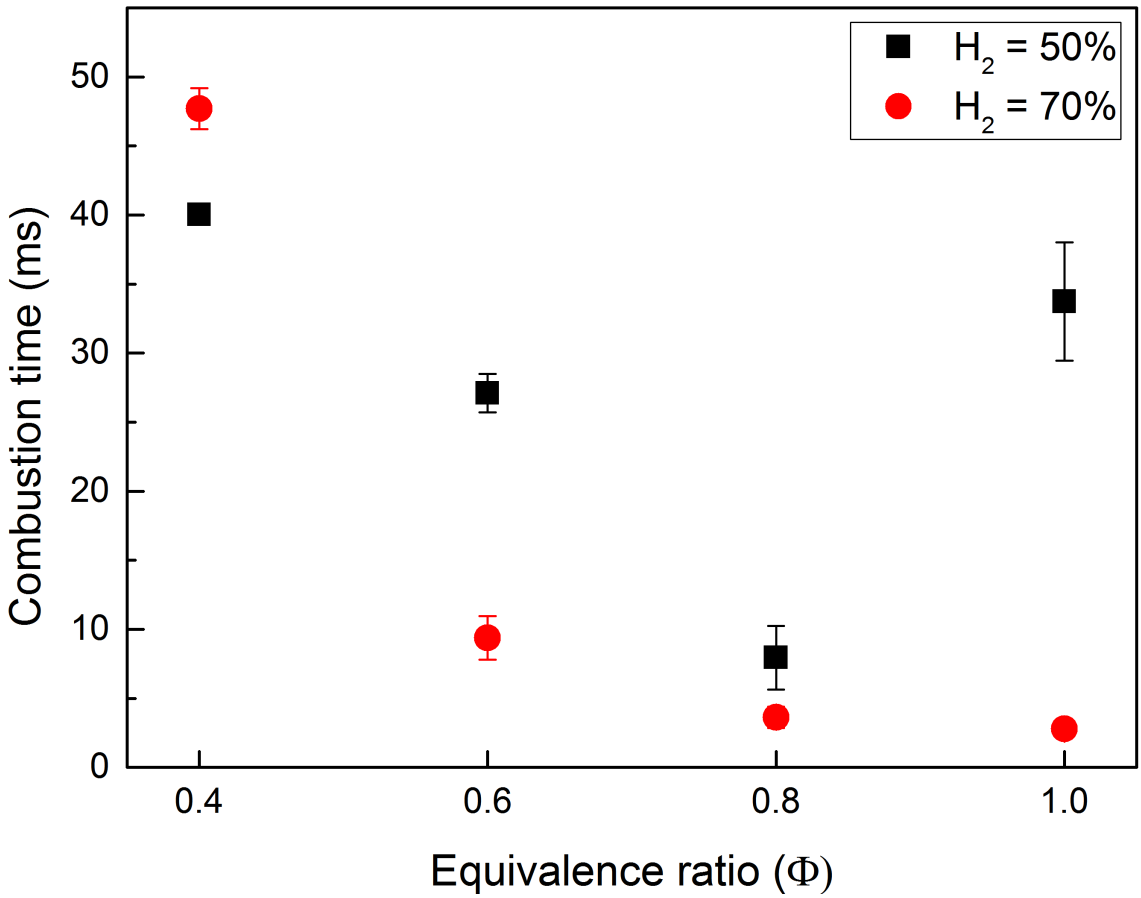

Fig. 4.11. Combustion time variation with respect to the equivalence ratio and the hydrogen content

5. CONCLUSION AND RECOMMENDATIONS

This chapter contains the concluded comments for the current experimental study and recommendations for future work.

5.1 Conclusions

An experimental study was conducted to investigate the ignition delay time and the combustion characteristics of transient hot-jet ignition in a constant-volume combustion (CVC) chamber. A transient jet or puff or hot reactive gas was produced by spark ignition of a hydrogen-methane-air mixture in a pre-chamber, and injected into the CVC or main chamber to ignite another hydrogen-methane-air mixture in the main chamber. The mixture in the pre-chamber was fixed at an equivalence ratio 1.1 and a hydrogen content 50% by volume in the hydrogen and methane blend. Various equivalence ratios from 0.4 to 1.0 and hydrogen contents 50% and 70% by volume in the hydrogen and methane blend were adopted for the main CVC chamber mixture. In order to investigate the diaphragm rupture pressure effect on the ignition delay time, the indentation depth of a diaphragm varied. A Schlieren photography system was prepared to visualize shock waves and flame front movements, and an image processing code was created to analyze Schlieren images. Initial shock speeds were measured by using a high sampling rate of pressure transducers. This enabled a new validated methodology to find the ignition delay time by extrapolating the shock travel backward in time to the moment of the initial jet initiation by diaphragm rupture. High-speed flame luminosity images were obtained to validate the ignition delay time.

With the use of the slightly rich combustion mixture in the pre-chamber, ignition delay time in the CVC chamber reduces (a) with increase of the hydrogen content,

(b) with a decrease of the equivalence ratio, and (c) with increase of the diaphragm rupture pressure. As the hydrogen content increases, the ignition-promoting reactions are increased but the ignition-inhibiting reactions are decreased, and consequently the ignition delay time decreases. In previous reported experimental researches [35,74], it appeared that the equivalence ratio of the mixture with the same hydrogen-methane fuel blend tested in the current study had no effect on the ignition delay time. The major difference between the current and the previous experiments is the hot-jet ignition, so it is assumed that radicals in the hot-jet play a vital role in the decrease of the ignition delay time as the equivalence ratio decreases. The increase of the diaphragm rupture pressure increases temperature of the hot-jet and the amount of reactive radical in the hot-jet, leading to the increase of energy and effectiveness of the jet. Also, the initial shock strength increases with the increase of the diaphragm rupture pressure, increasing the temperature and pressure of the gas mixture and the mixing rates in the main chamber. All contribute to the reduction of the ignition delay time.

The highest maximum pressure in the main chamber was observed at equivalence ratio 0.8. It seems possible that the reaction rate of this gas mixture is the highest among the tested equivalence ratios, and therefore pressure builds up most rapidly at equivalence ratio 0.8. It has been investigated in previous studies for the laminar burning velocity [81] that the highest reaction rate appears at equivalence ratio 1.1 for combustion of the hydrogen-methane-air mixture, but the reactive radicals in the hot jet are involved in the combustion reactions, shifting the condition of the highest reaction rate from equivalence ratio 1.1 to 0.8. The shock-flame interaction exhibits two trends throughout the tested conditions, fast and slow flame propagations. In the fast flame propagation, flame front acceleration and large amplitudes of the flame front and pressure oscillations were observed, and frequencies of the pressure oscillation were high. In contrast, the slow flame propagation reveals low frequencies of the pressure oscillation, and the acceleration of the flame front by pressure waves was not observed. Amplitudes of the flame front motion and pressure oscillation were

also small. The flame front acceleration is caused by a feedback effect between the flame and shock waves, and it is assumed that a certain level of the reaction rate of the gas mixture is required in order to activate the feedback effect. If the feedback is not activated like the slow flame propagation cases, the flame front only shows oscillations by the pressure waves without stretched, and propagates slowly, causing a slow combustion time.

It was observed that the strength of the reflected was weaker than expected from the initial shock speed. It is argued that expansion fans generated in the pre-chamber are able to catch up the initial shock wave due to the short length of the pre-chamber, attenuating the strength of the initial shock wave, so the strength of the reflected shock wave also diminishes. This has not undermined confidence in the methodology of determining ignition delay times.

5.2 Recommendations

1) The present work focused on a stationary jet nozzle and pre-chamber, although the test rig was designed for a nozzle that traverses the CVC chamber through rotation of the pre-chamber. In order to experimentally simulate the ignition process in an actual wave rotor channel, an investigation of jet mixing affected by relative motion between the torch jet and the CVC is required. For this, the design and construction of both the pre-chamber and the main chamber should be improved to minimize a leakage from the gap between the two chambers. A previous CVC experiment conducted by Chinnathambi [44] included traversing motion with some leakage present. The issue of the gap between two chambers is not solved in the current study, so the effect of the relative motion was not able to be investigated. It is difficult to absolutely seal the contact surfaces, one is rotating and another is stationary, but the leakage should be minimized by redesign of the rig and alignment of the surfaces.

2) As the ignition delay time is measured using the initial shock speed, more accurate measurement of the initial shock speed is desired to reduce uncertainty in the

ignition delay time estimation. The PT1 was installed on a pressure probe to prevent heat damage from a flame in the chamber, but it caused amplitude and phase modulations of the pressure signal, incurring errors on the ignition delay time. Two pressure transducers flush mounted on the main chamber are required to measure the initial shock speed more precisely. An existing pressure transducer is flush mounted at the end of the main chamber, where the flame temperature is relatively low. The initial shock speed can be measured more precisely using another flush-mounted pressure transducer at a safe location on the chamber, with the use of a heat resistant grease to protect the sensor.

3) Temperature of the jet reactants and products should be measured accurately. The ignition delay time is strongly related to temperature of the reactants. Therefore, the temperature of the gas mixture in the main chamber is required to complete a correlation of the ignition delay time. The hot gas emerging from the pre-chamber into the CVC chamber will have experienced heat loss and may also be affected by incomplete combustion in the pre-chamber. However, since the combustion process is transient and has a very short time scale, the temperature cannot be measured using typical temperature measurement ways. A Rayleigh scattering measurement technique has been used to measure dynamic gas temperature at high sampling rates (10 kHz) [93,94], so it can be suggested as the best method for the current combustion condition.

4) A quantitative assessment of the pre-chamber combustion process and discharge process. At given pre-chamber combustion condition, the amount of hot-jet mass injection, pressure and profile of the jet, and the boundary effect should be measured to determine properties of the hot jet. Minimizing uncertainties from the amount of the gas supply and the depth of the diaphragm indentation is also required for an accurate assessment.

5) A quantitative model of transient jet ignition considering mixing and chemical kinetic processes. A complete ignition delay time correlation should be based on a detailed model.

6) Quantitative criteria to determine whether the flame propagation behavior is fast or slow should be established. If the combustion time is too long in an actual wave rotor channel, the gas mixture in the channel may be discharged with incomplete burning, causing an adverse influence on the system efficiency. Therefore, it is necessary to figure out a combustion condition promoting not only rapid ignition but also fast flame propagation. As the feedback between the flame and shock waves is highly related to the fast flame propagation condition, it should be investigated that the feedback is activated in which conditions. In order to figure out the feedback activation condition, the conditions between the hydrogen contents 50% to 70% at equivalence ratios 0.6 and 1.0 need to be investigated since those conditions showed large differences in the combustion time result. Also, as the reaction rate of the gas mixture, and the mixing effect by the shock-flame interaction have a vital role in the feedback mechanism, the criteria of the feedback activation condition can be established based on quantification of the reaction rate of the gas mixture and the vorticity production rate by the interaction.

LIST OF REFERENCES

LIST OF REFERENCES

[1] P. Akbari, R. Nalim, and N. Mueller, "A review of wave rotor technology and its applications," *Journal of Engineering for Gas Turbines and Power*, vol. 128, no. 4, pp. 717–735, 2006.

[2] M. Hirceaga, F. Iancu, and N. Muller, "Wave rotors technology and applications," in *The 11th International Conference on Vibration Engineering, Romania*, 2005.

[3] R. Knauff, "Converting pressures of liberated gas energy into mechanical work," *British Patent*, vol. 2818, 1906.

[4] H. Burghard 1913. British Patent 19,421.

[5] A. F. Lebre 1928. British Patent 290,669.

[6] H. Burghard 1929. German Patent 485,386.

[7] A. Meyer, "Recent developments in gas turbines," *Journal of Mechanical Engineering*, vol. 69, no. 4, pp. 273–277, 1947.

[8] M. Berchtold and F. Gardiner, "The comprex: A new concept of diesel supercharging," in *ASME 1958 Gas Turbine Power Conference and Exhibit*, pp. V001T01A016–V001T01A016, American Society of Mechanical Engineers, 1958.

[9] P. Akbari, R. Nalim, and N. Mueller, "A review of wave rotor technology and its applications," *Journal of Engineering for Gas Turbines and Power*, vol. 128, no. 4, pp. 717–735, 2006.

[10] G. B. Andre and C. Jendrassik, "Jet reaction propulsion units utilizing a pressure exchanger," 1956. US Patent 2,757,509.

[11] R. Pearson, "A pressure exchange engine for burning pyroil as the end user in a cheap power from biomass system," in *Turbines à gaz. Congrès international des machines à combustion. 15*, pp. 931–966, 1983.

[12] A. Mathur, "A brief review of the ge wave engine program (1958-1963)," in *Proceedings ONR/NAVAIR Wave Rotor Research and Technology Workshop*, pp. 171–193, 1985.

[13] R. Moritz, "Rolls-royce study of wave rotors (1965–1970)," in *Proceedings ONR/NAVAIR Wave Rotor Research and Technology Workshop*, pp. 116–124, 1985.

[14] G. E. Welch *et al.*, "Overview of wave-rotor technology for gas turbine engine topping cycles," in *Novel Aero Propulsion Systems International Symposium, The Institution of Mechanical Engineers*, pp. 2–17, 2000.

[15] P. Akbari and R. Nalim, "Review of recent developments in wave rotor combustion technology," *Journal of Propulsion and Power*, vol. 25, no. 4, pp. 833–844, 2009.

[16] W. H. Heiser and D. T. Pratt, "Thermodynamic cycle analysis of pulse detonation engines," *Journal of Propulsion and Power*, vol. 18, no. 1, pp. 68–76, 2002.

[17] U. L. I. U. Perera, *Experimental investigation into combustion torch jet ignition of methane-air, ethylene-air, and propane-air Mixtures.* MS thesis, Purdue University, 2010.

[18] T. M. Elharis, S. D. Wijeyakulasuriya, and M. R. Nalim, "Wave rotor combustor aerothermodynamic design and model validation based on initial testing," in *46th AIAA/ASME/SAE/ASEE Joint Propulsion Conference & Exhibit, AIAA 2010-7041*, 2010.

[19] M. R. Nalim, "Longitudinally stratified combustion in wave rotors," *Journal of Propulsion and Power*, vol. 16, no. 6, pp. 1060–1068, 2000.

[20] D. Lieberman, K. Parkin, and J. Shepherd, "Detonation initiation by a hot turbulent jet for use in pulse detonation engines," in *38th Joint Propulsion Conference, Indianapolis, IN, July*, pp. 7–10, 2002.

[21] P. Higelin, C. Robinet, C. Mounaim-Rouselle, O. Pajot, and B. Moreau, "A new combustion concept for internal combustion engines," in *Proceedings of the 15th Internal Combustion Engine Symposium (International)*, vol. 9935761, 1999.

[22] T. Ma, H. Zhao, J. Li, and N. Ladommatos, "Experimental investigation of controlled auto-ignition (cai) combustion in a 4-stroke multi-cylinder gasoline engine and drive cycle simulations," in *A new generation of engine combustion processes for the future*, pp. 115–124, 2001.

[23] M. Elhsnawi and A. Teodorczyk, "Experimental study of hot inert gas jet ignition of hydrogen-oxygen mixture," in *First International Conference on Hydrogen Safety, Pisa, Italy*, pp. 8–10, 2005.

[24] R. Sadanandan, D. Markus, R. Schießl, U. Maas, J. Olofsson, H. Seyfried, M. Richter, and M. Aldén, "Detailed investigation of ignition by hot gas jets," *Proceedings of the Combustion Institute*, vol. 31, no. 1, pp. 719–726, 2007.

[25] I. Iglesias, M. Vera, A. L. Sánchez, and A. Liñan, "Numerical analyses of deflagration initiation by a hot jet," *Combustion Theory and Modelling*, vol. 16, no. 6, pp. 994–1010, 2012.

[26] M. Bilgin, *Stationary and rotating hot jet ignition and flame propagation in a premixed cell.* PhD thesis, University of Washington, 1998.

[27] P. Lakshminarayanan and Y. V. Aghav, "Ignition delay in a diesel engine," in *Modelling Diesel Combustion*, pp. 59–78, Springer, 2010.

[28] K. Zhang, C. Banyon, C. Togbé, P. Dagaut, J. Bugler, and H. J. Curran, "An experimental and kinetic modeling study of n-hexane oxidation," *Combustion and Flame*, vol. 162, no. 11, pp. 4194–4207, 2015.

[29] D. Davidson and R. Hanson, "Interpreting shock tube ignition data," *International Journal of Chemical Kinetics*, vol. 36, no. 9, pp. 510–523, 2004.

[30] J. Wang, Z. Huang, Y. Fang, B. Liu, K. Zeng, H. Miao, and D. Jiang, "Combustion behaviors of a direct-injection engine operating on various fractions of natural gas–hydrogen blends," *International Journal of Hydrogen Energy*, vol. 32, no. 15, pp. 3555–3564, 2007.

[31] S. Rousseau, B. Lemoult, and M. Tazerout, "Combustion characterization of natural gas in a lean burn spark-ignition engine," *Proceedings of the Institution of Mechanical Engineers, Part D: Journal of Automobile Engineering*, vol. 213, no. 5, pp. 481–489, 1999.

[32] L. Ben, N. Raud-Ducros, R. Truquet, and G. Charnay, "Influence of air/fuel ratio on cyclic variation and exhaust emission in natural gas si engine," tech. rep., SAE Technical Paper, 1999.

[33] K. Nanthagopal, R. Subbarao, T. Elango, P. Baskar, and K. Annamalai, "Hydrogen enriched compressed natural gas- a futuristic fuel for internal combustion engines," *Thermal Science*, vol. 15, no. 4, pp. 1145–1154, 2011.

[34] S. B. Shrestha and G. Karim, "Hydrogen as an additive to methane for spark ignition engine applications," *International Journal of Hydrogen Energy*, vol. 24, no. 6, pp. 577–586, 1999.

[35] Y. Zhang, X. Jiang, L. Wei, J. Zhang, C. Tang, and Z. Huang, "Experimental and modeling study on auto-ignition characteristics of methane/hydrogen blends under engine relevant pressure," *international journal of hydrogen energy*, vol. 37, no. 24, pp. 19168–19176, 2012.

[36] H. Taylor and J. Waldram, "Improvements in the schlieren method," *Journal of Scientific Instruments*, vol. 10, no. 12, p. 378, 1933.

[37] H. Richard and M. Raffel, "Principle and applications of the background oriented schlieren method," *Measurement Science and Technology*, vol. 12, no. 9, p. 1576, 2001.

[38] F. Parsinejad, J. C. Keck, and H. Metghalchi, "On the location of flame edge in shadowgraph pictures of spherical flames: a theoretical and experimental study," *Experiments in Fluids*, vol. 43, no. 6, pp. 887–894, 2007.

[39] E. Hecht and A. Zajac, *Optics, chapter 9.* Addison Wesley, New York, 2002.

[40] A. Schuster, *An introduction to the theory of optics.* Edward Arnold, London, 1904.

[41] G. S. Settles, *Schlieren and shadowgraph techniques: visualizing phenomena in transparent media.* Springer Science & Business Media, 2012.

[42] P. K. Panigrahi and K. Muralidhar, *"Laser schlieren and shadowgraph", Schlieren and shadowgraph methods in heat and mass transfer.* Springer, 2012.

[43] J. A. Volpe and G. S. Settles, "Laser-induced gas breakdown as a light source for schlieren and shadowgraph particle image velocimetry," *Optical Engineering*, vol. 45, no. 8, pp. 080509–080509, 2006.

[44] P. Chinnathambi, *Experimental investigation on traversing hot jet ignition of lean hydrocarbon-air mixtures in a constant volume combustor*. MS thesis, Purdue University, 2014.

[45] M. N. Khan, *Three-dimensional transient numerical study of hot-jet ignition of methane-hydrogen blends in a constant-volume combustor*. MS thesis, Purdue University, 2015.

[46] K. Murphy, *Experimental Investigation of Traversing Hot-Jet Ignition of Ethylene, and Propane-Air Mixtures in a Constant-Volume Combustor*. MS thesis, Purdue University, Unpublished, Estimated deposit year: 2016.

[47] R. C. Flagan and J. H. Seinfeld, *Fundamentals of air pollution engineering*. Courier Corporation, 2013.

[48] "http://www.wunderground.com," Weather Underground: Weather Forecast & Reports. Last date accessed: Jan/6/2016.

[49] S. Carter, A. Ned, J. Chivers, and A. Bemis, *Selecting Piezoresistive vs. Piezoelectric Pressure Transducers*. Application Note: AN-102, Industry/Kulite General Overview, 2015.

[50] *Electrical Transducer Nomenclature and Terminology*. Instrument Society of America, ISA37.11975 (R1982), 1982.

[51] W. Gopel, J. Hesse, and J. N. Zemel, *Sensors Applications, Sensors in Intelligent Buildings, Vol. 2*. Wiley, 1998.

[52] *Introduction to Piezoelectric Pressure Sensors*. Technical report, PCB Piezotronics, 2003.

[53] G. Li and E. J. Gutmark, "Effects of installation on dynamic pressure measurements," in *44th AIAA Aerospace Sciences Meeting and Exhibit*, p. 1387, 2006.

[54] D. L. Straub, D. H. Ferguson, R. Rohrssen, and E. Perez, *Design considerations for remote high-speed pressure measurements of dynamic combustion phenomena*. National Energy Technology Laboratory, US Department of Energy, 2007.

[55] R. Rohrssen, *Acoustic Characteristics of a Dynamic Pressure Sensing Apparatus with Applications to Gas Turbine Combustors*. PhD thesis, West Virginia University, 2007.

[56] D. R. Englund and W. B. Richards, "The infinite line pressure probe," *Thirty-ninth International Instrumentation Symposium*, 1984.

[57] J. Oh, M. Kim, and Y. Yoon, "The tuning methodology of a ge 7fa+ e dln-2.6 gas turbine combustor," *Applied Thermal Engineering*, vol. 36, pp. 14–20, 2012.

[58] S. D. Gallimore, *A study of plasma ignition enhancement for aeroramp injectors in supersonic combustion applications*. PhD thesis, Virginia Polytechnic Institute and State University, 2001.

[59] P. A. Boettcher, *Thermal ignition*. PhD thesis, California Institute of Technology, 2012.

[60] A. Sangeetha and S. Rajesh Kannan, "Detecting fire and flame images using an auto adaptive edgedetection algorithm," in *International Journal of Recent Development in Engineering and Technology*, vol. Volume 2, Special Issue 3, 2014.

[61] R. T. E. Hermanns, J. Kortendijk, R. Bastiaans, and L. De Goey, *Laminar burning velocities of methane-hydrogen-air mixtures*. Universal Press, 2007.

[62] E. Hu, Z. Huang, J. He, C. Jin, and J. Zheng, "Experimental and numerical study on laminar burning characteristics of premixed methane–hydrogen–air flames," *international journal of hydrogen energy*, vol. 34, no. 11, pp. 4876–4888, 2009.

[63] T. Boushaki, Y. Dhué, L. Selle, B. Ferret, and T. Poinsot, "Effects of hydrogen and steam addition on laminar burning velocity of methane–air premixed flame: experimental and numerical analysis," *international journal of hydrogen energy*, vol. 37, no. 11, pp. 9412–9422, 2012.

[64] H. W. Liepmann and A. Roshko, *Elements of gasdynamics*. Courier Corporation, 1957.

[65] B. Schmidt, "Galcit 6-inch shock tube," *Technical report, California Institute of Technology*, 2013.

[66] I. I. Glass and J. G. Hall, "Handbook of supersonic aerodynamics. section 18. shock tubes," tech. rep., DTIC Document, 1959.

[67] B. Bobbitt, S. Sahaner, and B. Schmidt, "The combustion driven shock tube," *Technical report, California Institute of Technology*, 2012.

[68] I. Glass, "Shock tubes, part 1: Theory and performance of simple shock tubes," *UTIA Review No. 12*, 1958.

[69] H. Mark, *The interaction of a reflected shock wave with the boundary layer in a shock tube*. National Advisory Committee for Aeronautics, 1958.

[70] A. Sundaramurthy and N. Chandra, "A parametric approach to shape field-relevant blast wave profiles in compressed-gas-driven shock tube," *Frontiers in neurology*, vol. 5, 2014.

[71] H. Mirels, "Attenuation in a shock tube due to unsteady-boundary-layer action," *NASA National advisory committee for aeronautics report 1333*, 1957.

[72] R. L. Trimpi and N. B. Cohen, "A theory for predicting the flow of real gases in shock tubes with experimental verification," *NASA Technical note 3375*, 1955.

[73] A. R. Staff, "Equations, tables, and charts for compressible flow," *NACA Report*, vol. 1135, 1953.

[74] W. en Natuurwetenschappen, F. Zwarts, and S. Gersen, *Experimental study of the combustion properties of methane/hydrogen mixtures*. PhD thesis, University of Groningen, 2007.

[75] C. Tang, Y. Zhang, and Z. Huang, "Progress in combustion investigations of hydrogen enriched hydrocarbons," *Renewable and Sustainable Energy Reviews*, vol. 30, pp. 195–216, 2014.

[76] B. Adhikary and S. K. Aggarwal, "Ignition of methane-hydrogen mixtures at high pressures," in *48th AIAA Aerospace Sciences Meeting Including the New Horizons Forum and Aerospace Exposition*, p. 1357, 2010.

[77] Y. Zhang, Z. Huang, L. Wei, J. Zhang, and C. K. Law, "Experimental and modeling study on ignition delays of lean mixtures of methane, hydrogen, oxygen, and argon at elevated pressures," *Combustion and Flame*, vol. 159, no. 3, pp. 918–931, 2012.

[78] R. Cheng and A. Oppenheim, "Autoignition in methane-hydrogen mixtures," *Combustion and Flame*, vol. 58, no. 2, pp. 125–139, 1984.

[79] E. L. Petersen, J. M. Hall, S. D. Smith, J. de Vries, A. R. Amadio, and M. W. Crofton, "Ignition of lean methane-based fuel blends at gas turbine pressures," *Journal of Engineering for Gas Turbines and Power*, vol. 129, no. 4, pp. 937–944, 2007.

[80] "https://www.grc.nasa.gov/www/ceaweb/," Chemical Equilibrium with Applications Code. Last date accessed: Mar/21/2016.

[81] P. Dirrenberger, H. Le Gall, R. Bounaceur, O. Herbinet, P.-A. Glaude, A. Konnov, and F. Battin-Leclerc, "Measurements of laminar flame velocity for components of natural gas," *Energy & fuels*, vol. 25, no. 9, pp. 3875–3884, 2011.

[82] A. Karimi, *Numerical study of hot jet ignition of hydrocarbon-air mixtures in a constant-volume combustor*. MS thesis, Purdue University, 2014.

[83] R. Samtaney and N. J. Zabusky, "On shock polar analysis and analytical expressions for vorticity deposition in shock-accelerated density-stratified interfaces," *Physics of Fluids A: Fluid Dynamics (1989-1993)*, vol. 5, no. 6, pp. 1285–1287, 1993.

[84] V. Kilchyk, R. Nalim, and C. Merkle, "Baroclinic vortex sheet production by shocks and expansion waves," *Shock Waves*, vol. 20, no. 5, pp. 367–380, 2010.

[85] V. Kilchyk, R. Nalim, and C. Merkle, "Laminar premixed flame fuel consumption rate modulation by shocks and expansion waves," *Combustion and Flame*, vol. 158, no. 6, pp. 1140–1148, 2011.

[86] V. Kilchyk, *Pressure-wave amplification of flame area in wave rotor channels*. PhD thesis, Purdue University, 2009.

[87] E. Lutoschkin, M. Rose, and S. Staudacher, "Pressure-gain combustion using shock–flame interaction," *Journal of Propulsion and Power*, vol. 29, no. 5, pp. 1181–1193, 2013.

[88] M. Brouillette, "The richtmyer-meshkov instability," *Annual Review of Fluid Mechanics*, vol. 34, no. 1, pp. 445–468, 2002.

[89] D. E. Lutoschkin, *Pressure-gain combustion for gas turbines based on shock-flame interaction*. PhD thesis, University of Stuttgart, 2014.

[90] E. Schultz, E. Wintenberger, and J. Shepherd, "Investigation of deflagration to detonation transition for application to pulse detonation engine ignition systems," in *Proceedings of the 16th JANNAF Propulsion Symposium*, pp. 175–202, Citeseer, 1999.

[91] P. H. Azoury, *Engineering applications of unsteady fluid flow.* Wiley, 1992.

[92] T. Scarinci, J. Lee, G. Thomas, R. Bambrey, and D. Edwards, "Amplification of a pressure wave by its passage through a flame front," *Dynamics of heterogeneous combustion and reacting systems*, pp. 3–24, 1993.

[93] R. G. Seasholtz, "2d velocity and temperature measurements in high speed flows based on spectrally resolved rayleigh scattering," in *New Trends in Instrumentation for Hypersonic Research*, pp. 399–408, Springer, 1993.

[94] A. F. Mielke and K. A. Elam, "Molecular rayleigh scattering diagnostic for measurement of high frequency temperature fluctuations," in *Optics & Photonics 2005*, International Society for Optics and Photonics, 2005.

APPENDICES

Appendix A MATLAB Code to Measure the Flame Front Position by Time

```
clear all
clc
filename=input('Only enter a file name to bring the file list: ','s');
if(isempty(strfind(filename,'.'))~=1);
   error('Do not enter the file extension');
end;
fid=fopen([filename,'.dat'],'r');
if(fid==-1);
   error(['Failed to read.',filename,' is a wrong input. Please
   re-check the file name']);
end;
[IN1]=fscanf(fid,'%g %g %g',3);
total=IN1(1);  %total file number
starttime=IN1(2); %image recording start time
interval=IN1(3); %time interval between images

xposition=zeros(total, 112);
foravg=zeros(total, 112);

for IR=1:total;
     [filen]=fscanf(fid,'%s',1);
   if(isempty(strfind(filen,'.'))~=1);
      error(['Please make sure that the file name should begin
      with alphabet. the wrong file name is:',int2str(IR)])
```

```
   end;
    filbmp=sprintf('%s.bmp',filen);
    fig=imread(filbmp);

    I=rgb2gray(fig);
    BW=imgaussfilt(I,10);
    BW = edge(BW,'canny');
    BW = imdilate(BW,strel('square',3));
    BW = imfill(BW,'holes');
    BW = imerode(BW,strel('square',3));
    BW = bwareaopen(BW, 200);
    BW = bwperim(BW,8);
    finalfig=255*uint8(BW);

    i=rgb2gray(fianlfig);
    isize=size(i);

    for ii=1:isize(1);
     for iii=1:isize(2);
        if i(ii, iii)==255;
            xposition(IR, ii)=iii;
            foravg(IR, ii)=1;
        end
     end
    end
end

xposition=xposition';
foravg=foravg';
```

```
positioninfo=sum(xposition)./sum(foravg);
positioninfo=positioninfo';

for iiii=1:total;
    final(iiii,1)=starttime+(iiii-1)*interval;
end

final(:,2)=positioninfo*0.035775+28.767;
result_file_name = sprintf('result.txt');
data_save=fopen(result_file_name,'wt');

[Rowsize,Columsize]=size(final);
for k = 1 : 1 : Rowsize;
    for kk = 1 : 1 : Columsize;
        fprintf(data_save, '%10.5f\t', final(k,kk));
    end
    fprintf(data_save,'\n');
end
fclose(data_save);
```

Appendix B Flame Front Position Versus Pressure History from Schlieren Test Cases

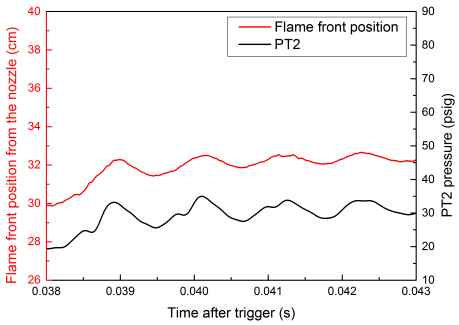

(a) H_2 content=50%, #=1

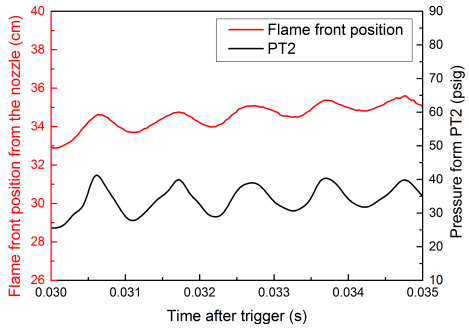

(b) H_2 content=50%, #=2

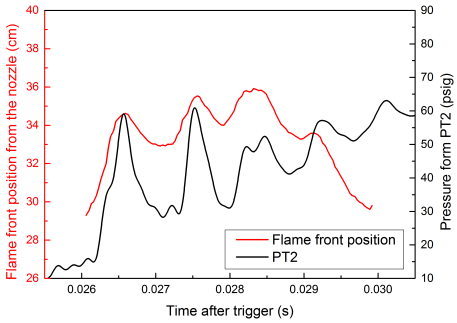

(c) H_2 content=70%, #=1

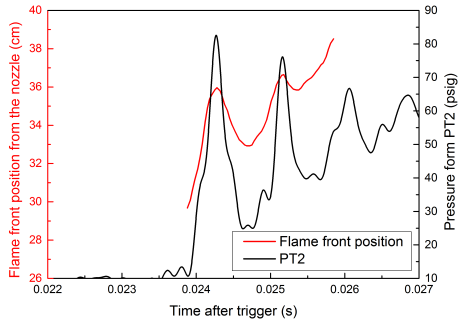

(d) H_2 content=70%, #=2

Fig. B.1. Φ=1.0, Time scale=5 ms, Pressure range=10∼90 psig, Flame front movement range=26∼40 cm

The flame front of Figure B.1 (c) is measured as if retreated at the end because another flame bubble is generated in front of the original flame front, and pushes back the original flame front like Figure B.2. The MATLAB code only can track the original flame front movement, so it is measured like drawing back.

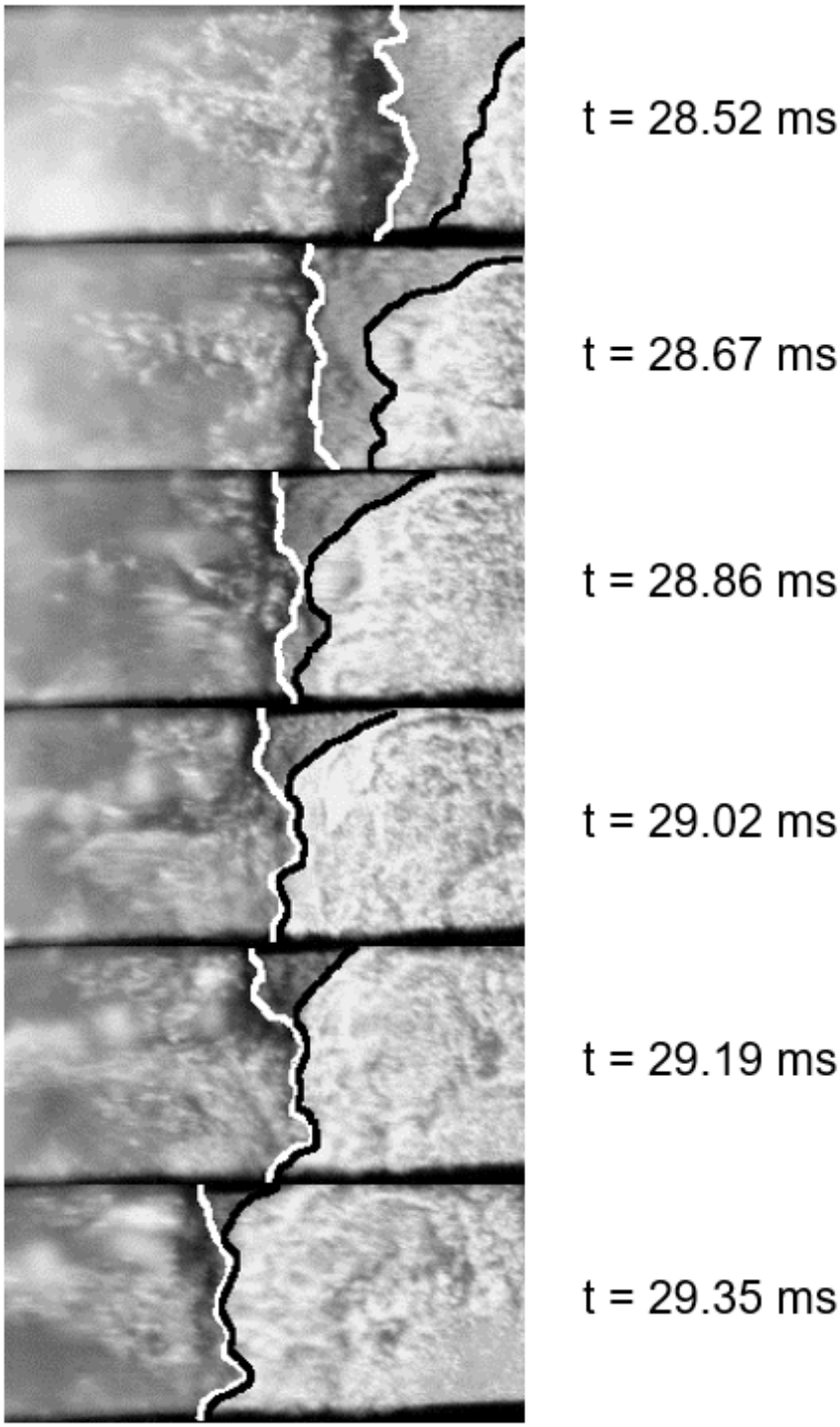

Fig. B.2. The original flame front (white line) is pushed out by the new flame bubble (black line) generated in front of the original flame

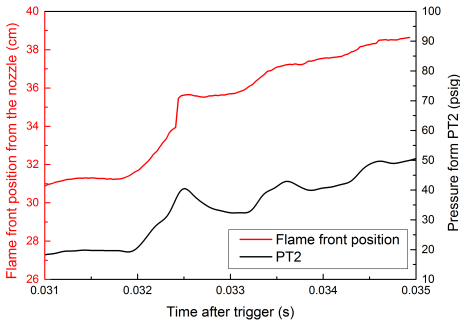

(a) H_2 content=50%, #=1

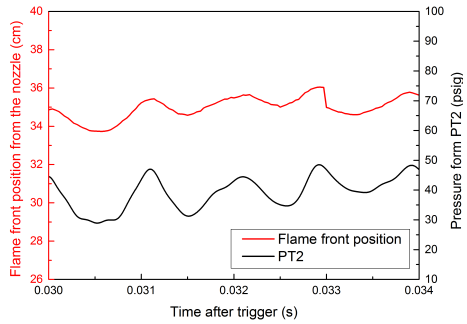

(b) H_2 content=50%, #=2

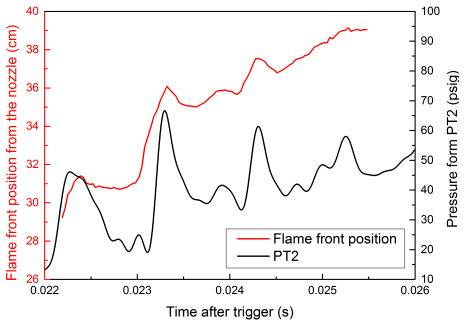

(c) H_2 content=70%, #=1

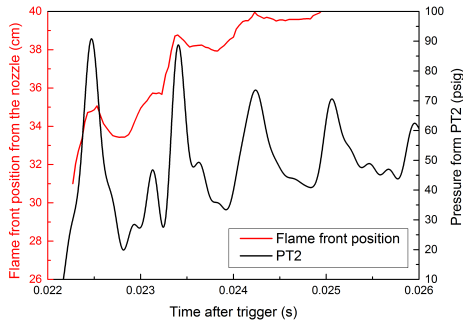

(d) H_2 content=70%, #=2

Fig. B.3. Φ=0.8, Time scale=4 ms, Pressure range=10$\sim$100 psig, Flame front movement range=26$\sim$40 cm

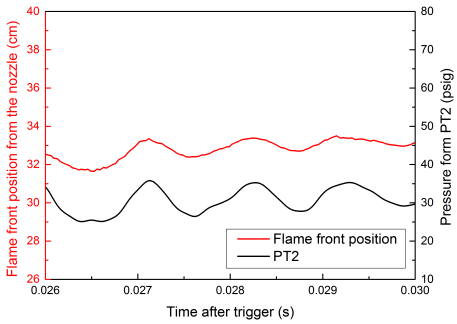

(a) H_2 content=50%, #=1

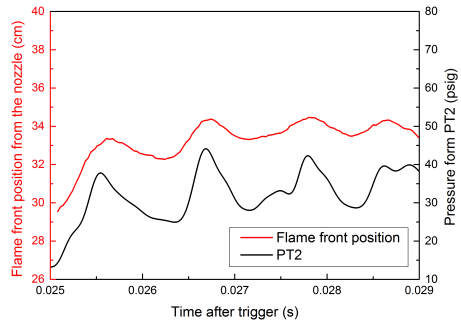

(b) H_2 content=50%, #=2

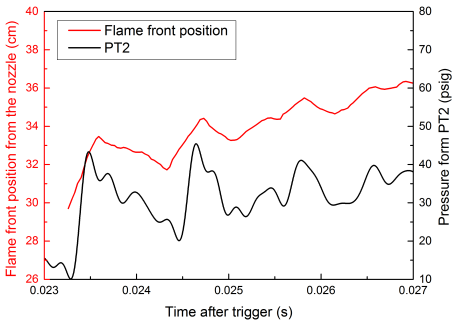

(c) H_2 content=70%, #=1

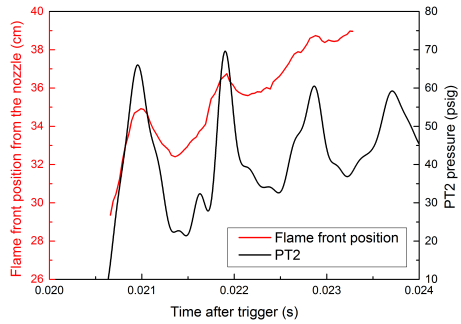

(d) H_2 content=70%, #=2

Fig. B.4. Φ=0.6, Time scale=4 ms, Pressure range=10∼80 psig, Flame front movement range=26∼40 cm

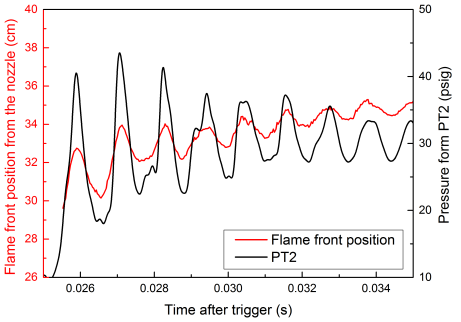

(a) H_2 content=50%, #=1

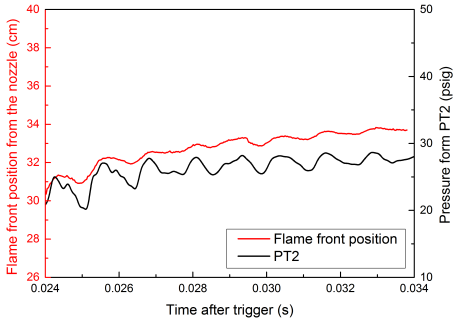

(b) H_2 content=50%, #=2

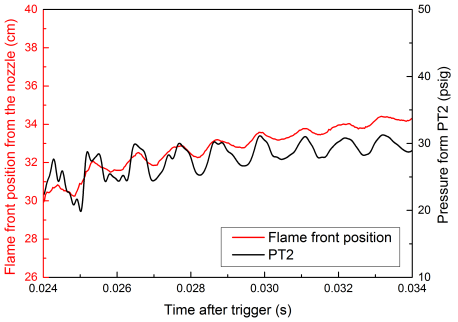

(c) H_2 content=70%, #=1

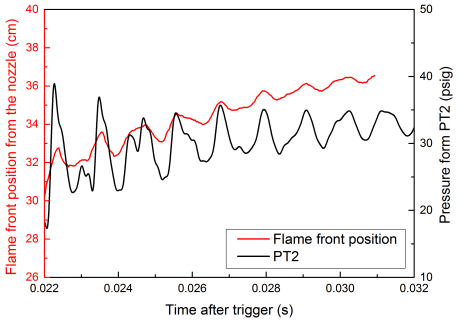

(d) H_2 content=70%, #=2

Fig. B.5. Φ=0.4, Time scale=10 ms, Pressure range=10∼50 psig, Flame front movement range=26∼40 cm